Intense Microwave Pulse Propagation Through
Gas Breakdown Plasmas in a Waveguide

By

DOUGLAS PAUL BYRNE
B.S. (University of Montana) 1977
M.S. (University of California, Davis) 1980

DISSERTATION

Submitted in partial satisfaction of the requirements for the degree of

DOCTOR OF PHILOSOPHY

in

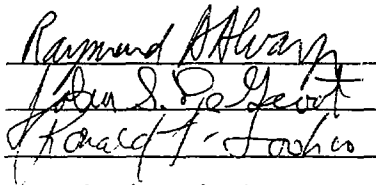Engineering-Applied Science

in the

GRADUATE DIVISION

of the

UNIVERSITY OF CALIFORNIA

DAVIS

Approved:

Committee in charge

Deposited in the University Library_____

Date   Librarian

This thesis is dedicated to my wife Robin, who's love, support, and understanding made it p⌐ssible.

TABLE OF CONTENTS

ACKNOWLEDGEMENTS

First, I want to thank my parents and family for all their love and emotional support.

I would like to thank the members of the staff at the Lawrence Livermore National Laboratory Electron Linac for all their help over the years. Special thanks go to mechanical technicians W. Patterson, S. Love, and W. Beisley, mechanical engineers/designers J. DeHart, W. Wong, and R. Lara, and coordinator A. Stoldal. Thanks also go to the electronics staff members H. Koberle, R. Booth, C. Herman, and J. Kimbrough for all their support.

The microwave engineering assistance and friendship provided by R. Johnson of EM Design, Pleasanton, CA, was invaluable.

The efforts of Dr. H Cabayan, Dr. D. Mayhall, Dr. D. Meeker, Dr. G. Sieger, Dr. J. Yee, and Dr. T. Young, who provided support and performed or assisted with many of the numerical calculations at LLNL, were greatly appreciated. I would also like to thank Dr. P. Bolton, Dr. J. Mercereau, and Dr. M. Fluss for their help and for many useful discussions, and Dr. J. Becker for the use of his data acquisition system.

I am especially thankful for all the editorial help given me by my dissertation committee: Dr. J. DeGroot, my thesis advisor, Dr. R. Soohoo, and Dr. R. Alvarez. To Dr. Alvarez, I owe a great debt; his knowledge and patience

were limitless, and he taught me many things.

LIST OF FIGURES

LIST OF TABLES

Douglas Paul Byrne
September 1986
Engineering - Applied Science

Intense Microwave Pulse Propagation Through

Gas Breakdown Plasmas in a Waveguide

Abstract

High-power microwave pulse-compression techniques are
used to generate 2.856 GHz pulses which are propagated in a
TE_{10} mode through a gas filled test section of waveguide,
where the pulses interact with self-generated gas-breakdown
plasmas. Pulse envelopes transmitted through the plasmas,
with durations varying from 2 ns to greater than 1 μs, and
peak powers of a few kW to nearly 100 MW, are measured as a
function of incident pulse power and gas pressure for air,
nitrogen, and helium. In addition, the spatial and temporal
development of the optical radiation emitted by the break-
down plasmas are measured.

For transmitted pulse durations $\geq$ 100 ns. good agree-
ment is found with both theory and existing measurements.
For transmitted pulse durations as short as 2 ns (less than
10 rf cycles), a two-dimensional model is used in which the
electrons in the plasma are treated as a fluid whose inter-
action with the microwave pulse are governed by a self-con-
sistent set of fluid equations and Maxwell's equations for
the electromagnetic field. The predictions of this model
for air are compared with the experimental results over a
pressure range of 0.8 torr to 300 torr. Good agreement is

obtained above about 1 torr pressure, demonstrating that

microwave pulse propagation above the breakdown threshold

can be accurately modeled on this time scale.

Chapter I - Introduction

The electrical breakdown of a gas due to the applica-
tion of an oscillating electric field is a process that has
been studied extensively during the last 40 years. Though a
considerable body of experimental and theoretical work
exists,[1-4] few measurements have been made on pulsed micro-
wave breakdown, particularly for pulse durations of less
than 100 ns. In most earlier work, resonant cavities were
employed to enhance the electric fields obtainable from
available microwave sources. Tetenbaum et al.,[5] used cylin-
drical cavities resonant in a $TM_{0,0}$ mode to make air break-
down measurements with pulses that had durations as short as
100 ns. However, the electric field build-up time in a ca-
vity ($\sim Q/\omega$) generally precludes making breakdown measure-
ments on much shorter time scales.

Modern high-power microwave pulse generation tech-
niques that are now available make it possible to generate
the high fields necessary to study gas breakdown on a nano-
second time scale over a wide range of pressures. Buntschuh
and Gilden[6] employed these techniques to make X-band break-
down measurements with effective pulse lengths as short as
2 ns, while more recently Didenko et al.,[7] investigated air
breakdown at S-band (2 to 4 GHz) with no pre-ionization, us-
ing effective pulse lengths of 10 to 50 ns. In all these
experiments, the data were obtained for pulse repetition

rates greater than or equal to 50 hertz.

   The purpose of the experiments done for this thesis was
to investigate the problem of S-band frequency microwave
pulse propagation above the breakdown threshold for pulse
durations as short as 2 ns. The most important result of
these investigations is that propagation on this time scale
can be accurately modeled, above about 1 torr pressure, by
treating the electrons in the breakdown plasma as a charged
fluid whose interactions with the pulse are governed by a
self-consistent set of fluid equations and Maxwell's equa-
tions for the electromagnetic field.[8] Measured envelope
waveforms of pulses transmitted through breakdown plasmas,
with durations varying from 2 ns greater than 1 μs, will be
presented as a function of incident pulse shape and power,
and gas pressure. In addition, comparisons of the data to
fluid-theory simulations will be presented for transmitted
pulse durations from 2 ns to about 100 ns. This time domain
is about an order of magnitude shorter than has been pre-
viously investigated experimentally at S-band, and is at
least an order of magnitude shorter than any single pulse,
multi-megawatt, microwave breakdown measurements.

   Because of their engineering and practical interest,
the atmospheric gases, air and nitrogen, were chosen for
study. Air is the gas which has received the most extensive
theoretical treatment, and is the one on which this thesis
will concentrate. Experimental measurements were also made
on helium, since it is one of the easiest gases to treat

theoretically.   This data will be included in Appendix C.

All breakdown and propagation measurements were done in situ in a traveling-wave section of S-band, WR284 waveguide, at pressures in the range 0.1 torr to 700 torr.   The micro-wave frequency was 2.856 GHz, and the peak pulse power varied from a few kW to about 100 MW.

A ^{60}Co γ-radiation source was placed in proximity to the waveguide and provided seed electrons, via ionization of the gas, from which a breakdown avalanche could initiate. The envelopes of microwave pulses incident on this seed-electron region, as well as those reflected from and trans-mitted through the region, were measured.   The measurements were repeated many times for a given incident pulse in order to characterize the statistics of the breakdown/pre-ioniza-tion process.

The experimental procedure and setup are discussed in Chapter III, while the experimental results and comparisons of these results with fluid-theory calculations are con-tained in chapter IV.   The results include data on the time and spatial development of the optical radiation emitted from the breakdown plasma, in addition to the data on pulse transport.   Chapter II provides a brief description of the electrical properties of breakdown in waveguides.   It in-cludes some background on early theories of gas breakdown, and finishes with a discussion of the theoretical framework of the fluid model.   Finally, Appendix A contains all the experimental details not found in the main body of the the-

sis, and Appendix B discusses the estimation of the source-generated seed-electron density used as input to the fluid-model calculations.

Chapter II - Background and Theory

2.1 Gas Breakdown in Microwave Fields

When a gas is subjected to a microwave electric field, charged particles in the volume are accelerated. If the charged particles suffer collisions during the microwave field period, energy can be transferred from the field to the particles. The energy transfer to the electrons will be much greater than to the ions because of the mass difference; indeed, for most purposes the motion of the ions can be ignored.

The energy gain rate will depend on the type of gas, since on the average, electrons undergoing elastic collisions will gain energy from the field, while inelastic collisions inducing atomic or molecular excitations will result in energy loss to radiation when the excitations decay. If the volume and field intensity are large enough, the electrons oscillate in the volume and some will gain enough energy to collisionally ionize the gas atoms or molecules, producing more free electrons. At the same time, electrons can diffuse to the walls containing the gas, recombine with positive ions, or attach to neutral atoms or molecules. The electron production and loss rates depend on the type of gas, microwave field strength and frequency, pressure, and container geometry. For continuously oscillating fields, there exists some field amplitude for which electron pro-

duction rates exceed loss rates. At this amplitude, break-
down is initiated and a microwave discharge will develop.
This threshold field is a function of the ionization poten-
tial of the gas, the gas's electron collision properties,
the container geometry, and the field frequency.

For pulsed microwave fields, the pulse length is an
additional complicating parameter. In this case, the break-
down field for plane waves is reached when the plasma fre-
quency of the breakdown discharge exceeds the applied micro-
wave field frequency during the pulse. When this occurs,
the plasma expels and/or absorbs the fields and the gas's
microwave transmission properties are greatly altered. In
waveguide breakdown experiments, we say that breakdown has
occurred if the discharge plasma "noticeably" affects the
propagation of the pulse. As will be shown, these effects
may occur, in some cases, at discharge plasma frequencies
lower than the microwave field frequency. Generally,
though, these effects require plasma frequencies higher than
the microwave frequency because the discharges have less
than a wavelength spatial extent.

If no charged particles are present during the applica-
tion of the field, no breakdown will occur. In continuous
wave (cw) breakdown experiments, this is not necessarily a
problem, because cosmic rays provide occasional electrons.
On the other hand, electron production by cosmic rays does
not occur at a high enough rate for consistent pulsed break-
down measurements; other provisions must be made. In the

experiments done for this thesis, ^{60}Co sources provided con-
tinuous ionization of the gases used for breakdown studies
with short duration pulses.

2.2 Electrical Properties of a Breakdown Discharge in a
Waveguide

Microwave energy radiated from a directional antenna
can be focused so that most of the energy passes through an
area roughly equal to the square of the radiation wave-
length. Provided enough power is available, breakdown mea-
surements made using this technique can be completely inde-
pendent of wall effects. For a given microwave source
strength, however, the electric fields attainable in a dif-
fraction-limited beam are much lower than those attainable
in a waveguide matched to the output of the source, and
breakdown measurements in waveguide are possible over a
broader pressure and pulse duration range. Elimination of
wall effects are then accomplished by operating in a param-
eter range where electron mean free paths and oscillation
amplitudes are much less than the inner waveguide dimen-
sions.[9] In most of the experiments done for this work, the
gas pressures and field strengths were such that wall ef-
fects were essentially negligible. However, for the shor-
test, highest-field pulses studied, the calculated oscilla-
tion amplitudes at 0.8 torr were about 3 to 4 mm (~10% of
the narrow waveguide dimension); for those results it is
not possible to ignore the effects of the waveguide walls.

Pre-Ionization Sources and TE₁₀ Mode Peak Electric Field
Profile in WR284 Waveguide
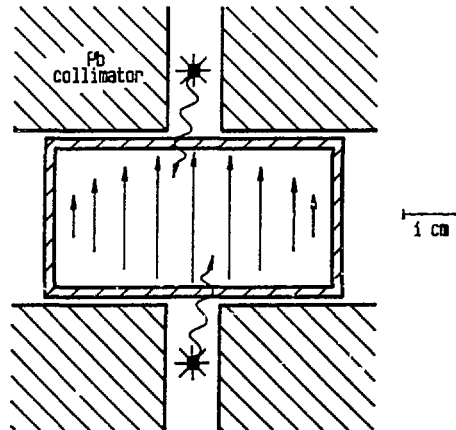
FIG. 2-1

The first step toward understanding breakdown in wave-
guides is to examine how the breakdown affects the impedance
properties of the guide. The waveguide mode used for the
measurements described here, the fundamental TE_{10} mode, is
the only mode that will propagate in WR284 waveguide be
tween the waveguide cut-off frequency (2.08 GHz) and about 4
GHz. This mode's electric field profile is shown above in
Fig. 2-1, where the pre-ionization geometry is indicated as
well. Because the electric field amplitude for this mode is
largest near the center of the waveguide, and because the
pre-ionization γ-rays are also collimated toward the wave-
guide center, one expects that breakdown would occur in the
center of the guide, along the electric field lines. That
this is the case is indicated by the time-integrated photo-

Waveguide breakdown in air and nitrogen;
time integrated photographs

200 torr air

200 torr nitrogen

25 torr air

100 torr nitrogen

5 torr air

25 torr nitrogen

0.8 torr air

1 torr nitrogen
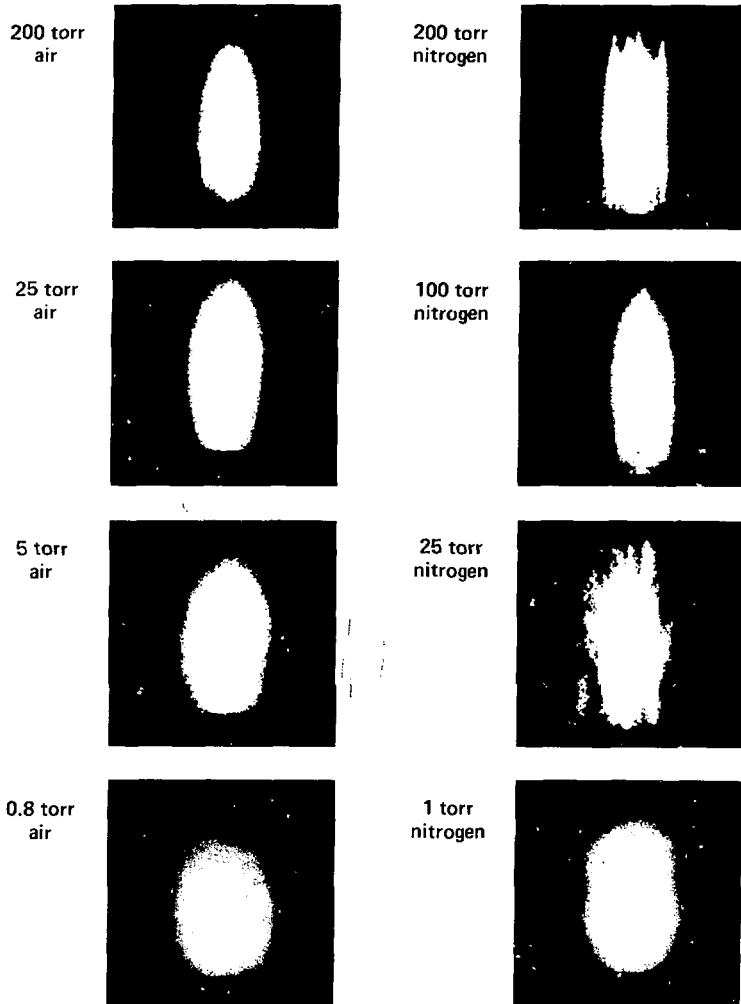
FIG. 2-2

graphs of waveguide breakdown shown in Fig. 2-2 (photographs are actual size). The camera view of the breakdown plasma is shown in Appendix A, Fig. A-5, and the photographs have been oriented for easy reference to Fig. 2-1. The photographs were taken with a streak camera operating in a framing mode with a 475-ns open shutter time.

The plasma radiation pattern and the spatial dependence of the initial electron density (due to the collimated γ-rays) suggest that the breakdown plasma is roughly cylindrical, its diameter being a function of the pressure. Initially, the breakdown may develop from a single electron or ionization track, but a cylindrical column will soon be formed. This column can become reflective, producing standing waves and subsequent breakdown columns, which would appear at spatial intervals equal to $\lambda_g/2$ (and $\lambda_g/4$) toward the microwave source. Reflection also tends to make the initially formed column elliptical, as more plasma is produced on the side of the column nearest to the microwave source. For analyzing the affect on microwave transmission, however, the initially formed cylindrical column is all we need consider. We can calculate, approximately, the impedance properties of a waveguide containing a centered, cylindrical breakdown plasma by following Schwinger, who analyzed the problem of a dielectric post in a waveguide.[10] Using variational principles, he calculated the parameters of the equivalent T circuit shown in Fig. 2-3. The parameters are

Cylindrical Dielectric Post In Rectangular Waveguide
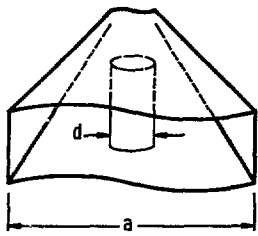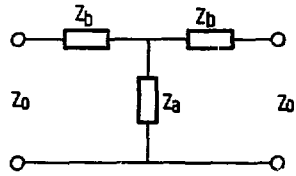
Waveguide View   **Equivalent Circuit**

FIG. 2-3

$$\frac{jZ_a}{Z_0} + \frac{jZ_b}{2Z_0} = \frac{a}{2\lambda_g}\left[\frac{J_0(\beta)}{J_0(\alpha)}\cdot\frac{1}{\beta J_0(\alpha)J_1(\beta)-\alpha J_0(\beta)J_1(\alpha)} - S_0 + \frac{\alpha^2}{4}\right],$$

$$\dots\dots\dots(2.1)$$

$$-\frac{jZ_b}{Z_0} = \left[\frac{2(\pi d)^2}{a\lambda_g}\right] \div \left[\frac{\alpha^2 J_1(\beta)}{J_1(\alpha)}\cdot\frac{1}{\alpha J_0(\alpha)J_1(\beta)-\beta J_0(\beta)J_1(\alpha)} - 2\right],$$

$$\dots\dots\dots(2.2)$$

where

$$\alpha = \pi d/\lambda \ , \quad \beta = (\pi d/\lambda)(k_r - jk_i)^{\frac{1}{2}} \ ,$$

and

$$S_0 = \ln(4a/\pi d) - 2 + 2\sum_{2}^{\infty}\left[(n^2-(2a/\lambda)^2)^{-\frac{1}{2}} - n^{-1}\right] \ .$$

In these expressions, Z_0 is the waveguide impedance (about 550Ω for TE_{10} waves of 2.856-GHz frequency in WR284 wave-

guide), λ_g is the guide wavelength, J_0 and J_1 are Bessel functions of order zero and one, respectively, and $k_r - jk_i$ is the (complex) dielectric constant of the centered post. The post diameter is d and the broad waveguide dimension is a. The equivalent circuit parameters calculated from eqns. 2.1 and 2.2 are expected to be accurate to within a few percent for d/a < 0.15, provided neither jZ_a/Z_0 or jZ_b/Z_0 is close to resonance.

The above analysis can be applied to a cylindrical breakdown plasma in a waveguide provided the plasma dielectric constant is known and the plasma is assumed to be uniformly cylindrical.

An appropriate representation of the breakdown discharge plasma is that of a collisional, unmagnetized Lorentz plasma, for which the dielectric constant is

$$k_r - jk_i = \left[1 - (n/n_c) \cdot \frac{1}{(1+(\nu/\omega)^2)} \right] - j\left[(n/n_c) \cdot \frac{(\nu/\omega)}{(1+(\nu/\omega)^2)} \right].$$

$$\ldots\ldots\ldots(2.3)$$

Here n is the plasma electron density, n_c is the critical density for propagation of 2.856-GHz microwaves, ω is the 2.856-GHz microwave frequency, and ν is the electron collision frequency for momentum transfer.

Strictly speaking, the Lorentz dielectric constant only represents plasmas for which the electron collision frequency is independent of electron energy. Though air and nitro-

gen breakdown plasmas subjected to intense microwave fields
do not have this property, MacDonald et al.,[11] have shown
that a value of $\nu = 5.3 \cdot 10^9 p$ (p in torr) allows for a rea-
sonably economical description of microwave air breakdown
data, subject to large errors only for pressures less than a
few torr. Bearing this assumption in mind, the microwave
transmission properties of an air breakdown discharge can
now be calculated from equations 2.1, 2.2, and 2.3.

From standard transmission line theory, the power ab-
sorbed, reflected, and transmitted by the breakdown column
can be calculated as a function of column diameter to wave-
guide width ratio d/a, collisionality ν/ω, and normalized
electron density n/n_c. Ignoring waveguide losses, the re-
sults are

Power reflection coefficient

$$|\rho|^2 = \left| \frac{(Z_{in}/Z_0) - 1}{(Z_{in}/Z_0) + 1} \right|^2 , \qquad (2.4)$$

where $\dfrac{Z_{in}}{Z_0} = \dfrac{(Z_a/Z_0) + (Z_b/Z_0) + [(2Z_a/Z_0)+(Z_b/Z_0)]Z_b/Z_0}{1 + (Z_a/Z_0) + (Z_b/Z_0)}$;

Power absorption coefficient

$$|\alpha|^2 = [(1 - |\rho|^2)(1 - P_0/P_{in})] , \qquad (2.5)$$

where $\dfrac{P_0}{P_{in}} = \dfrac{Z_0}{Re(Z_{in})} \cdot \left| \dfrac{(Z_a/Z_0)}{1 + (Z_a/Z_0) + (Z_b/Z_0)} \right|^2$;

Power transmission coefficient

$$|\tau|^2 = [1 - |\rho|^2 - |\alpha|^2] . \qquad (2.6)$$

These results are shown in Fig. 2-4, where each trans-
port coefficient is plotted against n/n_c for varying ν/ω and
$d/a=0.1$ in the first column, and for $d/a=0.3$ in the second
column. These d/a ratios compare favorably with the plasma
dimensions shown in Fig. 2-2. For comparison, Fig. 2-5
shows a similar plot for plane waves incident on a planar
free space-Lorentz plasma interface. Now a waveguide uni-
formly filled with plasma will actually cut off wave trans-
mission at a lower density than a free space plasma, but we
see from the figures that a plasma post in a waveguide actu-
ally cuts off transmission at a higher density than in the
free space case. As the post diameter gets larger, however,
transmission actually approaches that of free space as shown
in Fig. 2-4 for $d/a=0.3$.

Though these calculations are not self-consistent or
time dependent, in that the wave fields are assumed to have
no effect on the plasma electron density, they can be useful
for estimating breakdown plasma densities from pulse trans-
port data at a given instant in time, and for comparison to
calculated densities from self-consistent fluid model simu-
lations. In Chapter IV, some of the longer-pulse data are
compared to non-self-consistent fluid simulations, in which
the fields are not affected by the plasma. In this case,
breakdown density estimates (or data) are required in order
to predict when pulse transmission cuts off.

POWER TRANSPORT COEFFICIENTS; PLASMA POST IN WAVEGUIDE
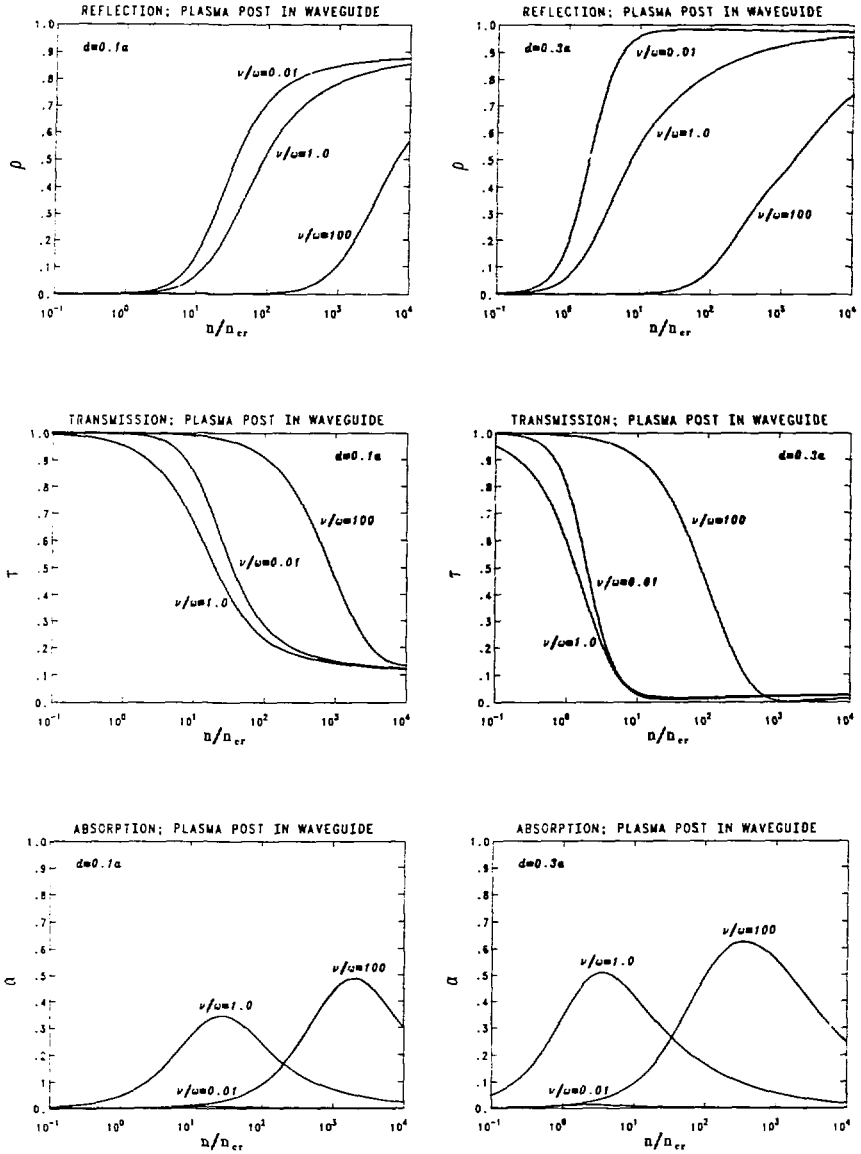
FIG. 2-4

POWER REFLECTION COEFFICIENT; PLANE WAVES
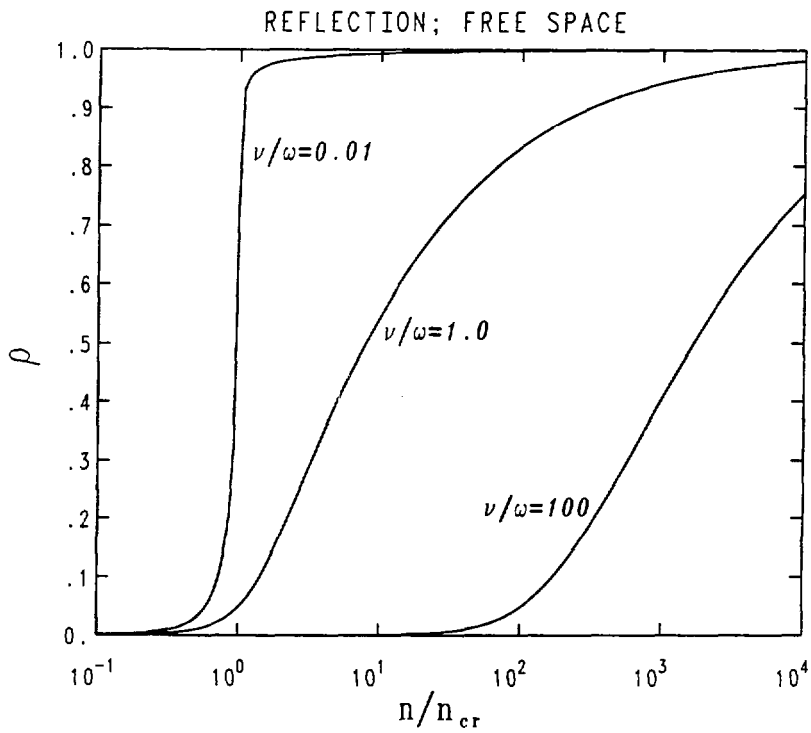
FIG. 2-5

2.3   Theory of Gas Breakdown by Microwave Fields

Since the electron density in any gas discharge deter-
mines its electrical behavior, any theoretical description
must account for its spatial and temporal variations.   Ulti-
mately, a continuity equation of the following form must be
solved,

$$\frac{\partial n(\vec{r},t)}{\partial t} = S + \nu_i n - \nu_a n - \nu_r n^2 + \nabla \cdot \nabla(Dn) \ . \tag{2.7}$$

This equation describes the time increase of free electron
density $n(\vec{r},t)$ due to external volume production at source
rate S and ionization at frequency ν_i, and decrease due to
electron attachment and recombination at rates ν_a and ν_r.
The last term represents loss due to diffusion.   Any other
gain or loss processes that may be important in a given sit-
uation must also be included.

Perhaps the simplest approach toward a solution of
equation 2.7 is the avalanche or cascade model used by Her-
lin and Brown[9,12-14] in their early work on cw breakdown in
cavity resonators.   In this model, the rate and transport
coefficients are assumed to be independent of time, and
equation 2.7 is separated into time- and space-dependent
parts, subject to boundary conditions on $n(\vec{r},t)$.   In cavity
experiments such as Herlin and Brown's, $n(\vec{r},t)$ must vanish
at the cavity walls.   If the cavity is overmoded, then dif-
fusion-eigensolutions of higher order than the fundamental
can result;   different boundary conditions on $n(\vec{r},t)$ must

then be applied. However, if the lowest-order eigensolution is assumed to dominate, if recombination is negligible, and if there is no source, $n(\vec{r},t)$ takes the exponential form,

$$n(\vec{r},t) = n_o \exp[(\nu_i - \nu_a - D/\Lambda^2)t] \cdot F(\vec{r},\Lambda) \ . \qquad (2.8)$$

In this equation, Λ is a geometry-dependent diffusion length and the rate coefficients in the exponent depend only on the electric field and the pressure. The function F depends on the diffusion mode, or combination of modes, i.e. on the field uniformity and geometry of the container. Herlin and Brown's TM_{010}-mode cylindrical cavities had $F(\vec{r},\Lambda) = \sin(z/\Lambda)$, with $\Lambda \sim L/\pi$, where z was the axial direction along which the electric field was directed, and L was the cavity length.

For the cw case, breakdown occurs when the exponent in equation 2.8 is positive, for then the electron density grows exponentially with time, or "cascades". Dividing the exponent by the pressure, the breakdown criterion can thus be written,

$$\nu_i/p = \nu_a/p + Dp/(p\Lambda)^2 \ . \qquad (2.9)$$

Microwave breakdown electric field amplitudes can be predicted phenomenologically from equation 2.9 using known dc breakdown data and the concept of "effective field".[15] The equation of motion of an electron in an electric field, subject to a velocity-dependent collisional (viscous) damping

force, is

$$m\frac{d\vec{v}}{dt} + m\nu_m\vec{v} = -e\vec{E} , \tag{2.10}$$

where ν_m is the collision frequency for momentum transfer. Provided ν_m is independent of velocity, expressions for the power transfer from the field to the electrons for the dc and alternating-field case, respectively, are

$$P = \frac{e^2 E_{dc}^2}{m\nu_m} \quad \text{and} \quad P = \frac{e^2 E_{rms}^2}{m\nu_m} \left[\frac{\nu_m^2}{\nu_m^2 + \omega^2} \right] . \tag{2.11}$$

Thus one can define

$$E_e \equiv E_{rms} \cdot \left[\frac{\nu_m^2}{\nu_m^2 + \omega^2} \right]^{1/2} , \tag{2.11b}$$

the "effective field" that would produce the same power transfer as a dc field. As was the case with the Lorentz plasma model, validity of the effective-field concept requires that ν_m be independent of electron energy. For $p\Lambda > 10$ torr·cm, however, MacDonald et al.,[11] have found that the cascade model, using the energy-independent collision frequency approximation, adequately described their air breakdown data. At low pressures and confined geometries, though, the theory breaks down. MacDonald[2] and Gould and Roberts[16] discuss predictions, using the effective-field concept, of cw breakdown-field thresholds in air, as a function of pressure, microwave frequency, and geometry.

The cascade model can also be applied to pulsed micro-
wave breakdown, where equation 2.8 becomes, for a pulse of
duration τ, constant amplitude, and negligibly short rise
time,

$$n_f \equiv n(\vec{r},\tau) = n_\circ \exp[(\nu_i - \nu_a - D/\Lambda^2)\tau] \cdot F(\vec{r},\Lambda) \quad . \quad (2.12)$$

Now the breakdown condition can be written

$$\nu_n/p = [\ln(n_f/n_0)]/p\tau + pD/(p\Lambda)^2 , \quad\quad (2.13)$$

where $\nu_n \equiv \nu_i - \nu_a$. In this case, a definition of n_f/n_0 for
breakdown must be provided. Gould and Roberts[16] made theo-
retical predictions of the breakdown field in air for a gi-
ven pulse length, using equation 2.13 and values of ν_n/p and
Dp obtained from dc measurements, as in the cw case. They
also made 2.8-GHz microwave breakdown measurements; light
emission from the gas discharge, as measured with a photo-
multiplier tube, served as their definition of breakdown. A
fit to their data indicated that n_f/n_0 was about 10^8, though
the initial electron density was not well known. Since the
initial density occurs logarithmically in equation 2.13,
predictions of breakdown field thresholds are relatively
insensitive to its value.

There are a number of questions, some already alluded
to, about the validity of the simple cascade model as mani-
fested in equation 2.13, and the effective-field concept,
particularly for time-varying fields in the few-nanosecond

pulse domain. Among these is the importance of higher oraer

diffusion modes and non-uniform fields, the validity of

treating ν_i as constant in time during the pulse envelope

(or even during the microwave-field period), and the effect

of space charge on the growth of $n(\vec{r},t)$. For this reason,

comparisons of theory and experiment for short-pulse data in

this thesis will employ more sophisticated models, namely

two variations of the plasma fluid model.

An accurate and detailed description of the properties

of an electrical gas discharge requires a knowledge of the

distribution function $F(\vec{r},\vec{v},t)$ for the electrons, defined as

the number of electrons within the spatial volume $d\vec{r}$=dxdydz

with velocities in the range from $\vec{v}$ to $\vec{v}+d\vec{v}$, at time t.

This distribution function satisfies the Boltzman equation,

$$\frac{\partial F}{\partial t} \; + \; \vec{v} \cdot \nabla_r F \; + \; \vec{a} \cdot \nabla_v F \; = \; \left[\frac{\partial F}{\partial t} \right]_c \; . \qquad (2.14)$$

Here ∇_r is the configuration-space gradient, ∇_v is the ve-

locity-space gradient, $\vec{a}$ is the external force per unit

electron mass, $(\vec{E} + \vec{v} \times \vec{B})q/m$, and $(\partial F/\partial t)_c$ is the change in F

due to collisions, including elastic, inelastic, and ion-

izing collisions. If the Boltzman equation can be solved,

the resulting distribution function provides all the infor-

mation required to calculate the electrical properties of

the discharge.

Though there is no known analytical method for solving

equation 2.14 exactly, it can in principle be solved numeri-

cally. If, on the other hand, the electrons are treated as a fluid and the physical quantities of interest are averaged over the distribution function, the problem becomes substantially less complex. This is done by first expanding the distribution function in spherical harmonics. Terms to first order are then substituted in equation 2.14, and the first three velocity moments of the resulting equation are calculated.[8] The three equations derived from this procedure are the electron fluid equations, which represent electron number balance, momentum balance, and energy balance for an electron fluid in which all electrons move with the average (fluid) velocity,[8]

Continuity

$$\frac{\partial n}{\partial t} + \nabla \cdot (n\vec{u}) = \langle v_i \rangle n \ , \tag{2.15}$$

Momentum

$$\frac{\partial (n\vec{u})}{\partial t} + \nabla \cdot (n\vec{u}\vec{u}) = \frac{nq}{m}(\vec{E} + \vec{u} \times \vec{B}) - \nabla \cdot (n\langle \vec{q}\vec{q} \rangle) - \int v_m \vec{v} f d\vec{v} \ ,$$
$$\ldots \ldots \ldots \ldots (2.16)$$

Energy

$$\frac{\partial (n\varepsilon)}{\partial t} + \nabla \cdot (n\langle \tfrac{1}{2} m v^2 \vec{v} \rangle) = nq\vec{E} \cdot \vec{u} - v_I \varepsilon n - v_w \varepsilon n \ , \tag{2.17}$$

where

n	=	free electron density, the distribution function integrated over velocity space;
$\vec{u}$	=	$\langle \vec{v} \rangle$, the velocity averaged over the distribution, by definition, the fluid velocity;
$\langle v_i \rangle$	=	ionization frequency averaged over the spherically symmetric term in the distribution function expansion;

$$\vec{q} \quad = \quad \vec{v} - \vec{u}, \text{ the non-streaming thermal velocity;}$$

$\frac{q}{m}(\vec{E} + \vec{v} \times \vec{B}) =$ the electromagnetic force per unit electron mass;

$\nu_m \quad =$ collision frequency for momentum transfer;

$n\epsilon \quad =$ averaged kinetic energy density;

$\nu_I \quad = \quad \epsilon_I \nu_i/\epsilon$, where ν_i is the ionization rate and ϵ_I is the ionization potential;

$\nu_w \quad = \quad (\Sigma \nu_e \epsilon_{ex})/\epsilon$, where ν_e is the collision frequency for excitation and ϵ_{ex} the corresponding excitation energy;

$f \quad =$ the first two terms of the distribution func-expansion in spherical harmonics.

Within a given volume equation 2.15 relates the rate-of-change of electron fluid density within that volume to fluid flow in or out of the volume and to the creation of electon fluid via ionization; thus the source term $\langle \nu_i \rangle n$.

In equation 2.16 momentum rate-of-change is related to divergence of momentum flow $n\vec{u}\vec{u}$, to internal thermal stress (the quantity $mn\langle \vec{q}\vec{q} \rangle$ is also known as the stress tensor), to external electromagnetic force, and to collisional momentum transfer.

Finally, equation 2.17 relates the rate-of-change of energy density to energy loss due to outward flux (or heat transfer), to power fed into the system by the electric field, and to energy taken up in ionizing and exciting collisions.

To describe the interaction of a microwave field with a fluid (breakdown) plasma, the fluid equations above must be combined with Maxwell's equations for the electromagnetic field, and the resulting coupled, non-linear, partial dif-

ferential equations must be solved for the boundary condi-
tions and situation of interest.

Yee and Mayhall have developed an electron-fluid compu-
ter model[8] which simulates the propagation of an electromag-
netic wave, with field strengths above the breakdown thresh-
old, in an air filled waveguide. In their model, the inte-
gral of $\nu_m \vec{v}$ over the spherical harmonic expansion of the
distribution function is approximated as

$$\int \nu_m \vec{v} f d\vec{v} \approx \langle \nu_m \rangle n \vec{u} \, , \tag{2.18}$$

and the ionization rate, momentum transfer rate, and energy
transfer rate for electrons in air are taken from both ex-
perimental results and theoretical calculations. Plots of
these rates as a function of characteristic electron energy
($u = kT_e$) are depicted in Fig. 2-6; Ref. 8 contains the
sources for them.

Simulations of some the waveguide breakdown experiments
presented here were done using the model described in Ref.
8, but expanded to two spatial dimensions.[17] Maxwell's
equations and the three "local" electron fluid equations
were solved numerically to follow the propagation of a micro-
wave pulse in a transverse-electric mode in a 2-dimensional,
air-filled waveguide. Fig. 2-7 shows the problem geometry
(the top and bottom waveguide walls had to be ignored in the
simulations because of the limit to two dimensions). The
following equations were solved self-consistently, using a

Ionization, momentum transfer, and energy loss
rates vs electron energy

(a) Ionization rate divided by
gas density
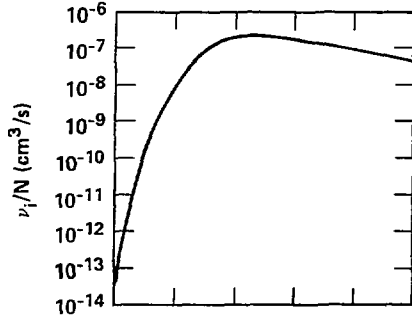
(b) Momentum transfer rate
divided by gas density
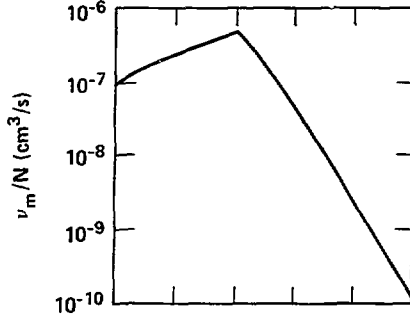
(c) Energy loss rate divided
by gas density
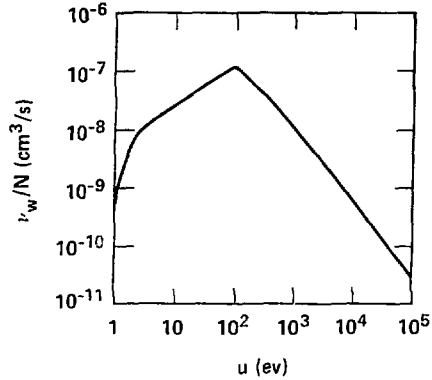
FIG. 2-6

Two-Dimensional Fluid Model Geometry
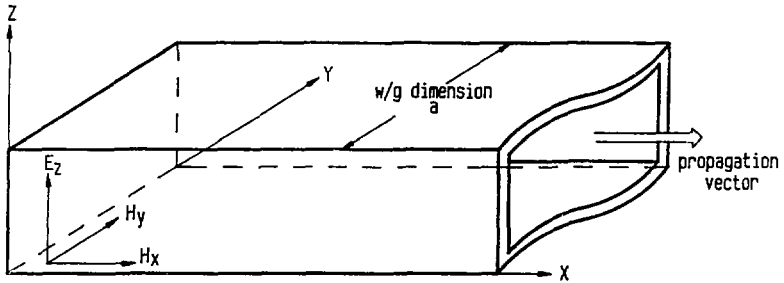
FIG. 2-7

finite-difference technique,

Maxwell's Equations

$$\nabla \times \vec{E} = -\mu_0 \frac{\partial \vec{H}}{\partial t} \quad \Rightarrow \quad \frac{\partial H}{\partial t}x = -\frac{1}{\mu_0}\frac{\partial E}{\partial t}z \quad ; \quad \frac{\partial H}{\partial t}y = \frac{1}{\mu_0}\frac{\partial E}{\partial t}z \ ;$$

$$\nabla \times \vec{H} = \vec{J} + \epsilon_0 \frac{\partial \vec{E}}{\partial t} \quad \Rightarrow \quad \frac{\partial E}{\partial t}z = \frac{1}{\epsilon_0}\left[\frac{\partial H}{\partial x}y - \frac{\partial H}{\partial y}x\right] - \frac{nev}{\epsilon_0}z \ ;$$

$$\vec{J} = nq\vec{v} = nqv_z \hat{k} \ ,$$

Local Fluid Equations

$$\frac{\partial n}{\partial t} = \nu_i(\epsilon)n \ , \tag{2.19}$$

$$\frac{m\partial(nv_z)}{\partial t} = nqE_z - mn\nu_m(\epsilon)v_z \ , \tag{2.20}$$

$$\frac{\partial(n\epsilon)}{\partial t} = -nv_z E_z - n\nu_w(\epsilon)(\epsilon-\epsilon_0) - n\epsilon_i\nu_i(\epsilon) \ . \tag{2.21}$$

Equation 2.21 has been written so that the kinetic energy ε (the rates in Fig. 2-6 are plotted vs characteristic energy $u=2\varepsilon/3$) is in eV; $\varepsilon_0=0.025$ eV is the neutral (thermal) energy, and ε_i is the average ionization potential (14 eV for air). Also, the velocities v and v_z in the above equations are fluid velocities, not the particle velocities in the Boltzman equation. These equations were derived from equations 2.15, 2.16, and 2.17 using equation 2.18 and the additional assumption, unjustified at the present time, that all convective terms could be neglected.

The results of these simulations, using the shortest incident pulses (~2 ns) measured as input, will be presented in Chapter IV, along with comparisons to actual measured transmitted pulses.

For the experiments which had times to breakdown, after the onset of the pulse, of greater than a few nanoseconds, the 2-dimensional simulations required impractical amounts of computer time. Thus for breakdown times of 10 ns to about 100 ns, the experiments were modeled using only a non-self-consistent set of fluid equations,

$$\frac{\partial n}{\partial t} = \nu_i(u)n \tag{2.22}$$

$$\frac{m\partial(nv)}{\partial t} = nqE - mn\nu_m(u)v \tag{2.23}$$

$$\frac{\partial(nu)}{\partial t} = -\frac{2}{3}nvE - n\nu_w(u)(u-u_0) - nu_i\nu_i(u) \tag{2.24}$$

These are the same as equations 2.19, 2.20, and 2.21, except

that the effects of the plasma currents on E (this is what
is meant by the term non-self-consistent) and the spatial
dependence of E, v, and n have been ignored, and the energy
is now defined as the characteristic electron energy, σr 2/3
the energy in equation 2.21. u_0 and u_i scale similarly, of
course. These equations are essentially an extension of the
cascade model described earlier to time varying fields, but
they avoid the use of the effective-field. They are some-
times called the swarm equations. Again, the equations were
solved numerically by a time-stepping technique, using mea-
sured incident-pulse power envelopes for input. Since this
model doesn't calculate the fields self-consistently, it
cannot predict transmitted-pulse waveforms. It can, how-
ever, predict pulse-breakdown thresholds if a breakdown den-
sity definition is made, say by using the results discussed
in Sec. 2.2 for pulse transport in a waveguide containing a
plasma post. A criterion for breakdown, using these re-
sults, will be given in Chapter IV, where we compare the
experiments with these calculations.

The justification for using a non-self-consistent model
is that by the time breakdown electron densities reach a
level where their currents begin to affect the fields, pulse
transmission is already very nearly cut off. For longer
pulse lengths, this model can predict breakdown thresholds
with reasonable accuracy, as will be seen in Chapter IV.

Chapter III - Experimental Methods

As noted in Chapter I, all breakdown and propagation
measurements in this study were done in waveguide. Micro-
wave pulses were introduced to a test section of waveguide
and propagated in a TE_{10} mode through the section, where
they interacted with the gas filling the waveguide. The
interaction was characterized by reflection and absorption
of parts of the pulse, as well as transmission to a load
terminating the test section. Directional couplers, micro-
wave attenuators, and fast diode detectors were used to mon-
itor the pulse both upstream and downstream from the inter-
action region, yielding incident, transmitted, and reflected
pulse envelopes for each single-pulse interaction. The
pressure of the gas inside the test section could be accu-
rately adjusted over a range of about 0.010 torr to one at-
mosphere, and gas purity was monitored with a residual-gas
analyzer/mass spectrometer. No more than 150 breakdown
measurements were made on the same volume of gas without
pumping out the test section and backfilling with fresh gas,
as it was observed that aging effects, most likely due to
chemical reactions, began to affect the data, particularly
at pressures above 100 torr. For fewer than 150 measure-
ments, no aging effects were observed. The waveguide test
section and all microwave diode detectors were regulated at
$30\pm1\,^{\circ}C$ during the experiments.

In addition to the microwave measurements, integrated
and real-time measurements of the development of the optical
radiation emitted from the breakdown plasma (integrated over
the spectral range of about 250 to 800 nm) were carried out.
Because this radiation was related to the electron density
and temperature of the plasma, its time development was re-
lated to the way in which the transmitted and reflected mi-
crowave pulses changed during breakdown, since these changes
depended on the electron density. Thus qualititive compari-
sons between the microwave and the optical measurements were
possible.

Two types of experiments were conducted: experiments
with effective microwave pulse lengths greater than or equal
to 10 ns, and experiments with pulse lengths of 2 to 3 ns
(FWHM). Since the experimental procedures for the two types
were different, they will be described separately. Experi-
mental details not included in the following descriptions
can be found in Appendix A.

3.1 Long-Pulse Experiments

The experimental arrangement for long-pulse experiments
is shown in Fig. 3-1. The low-power primary microwave
source was a highly stable oscillator which generated a con-
tinuous wave train at 2.856-GHz frequency and about one-half
watt average power. This wave train was gated by a fast PIN
diode to give pulses of 50-ns to slightly more than 1.5-μs
duration, at a typical repetition rate of one pulse every

Long-Pulse Measurements -- Experimental Layout
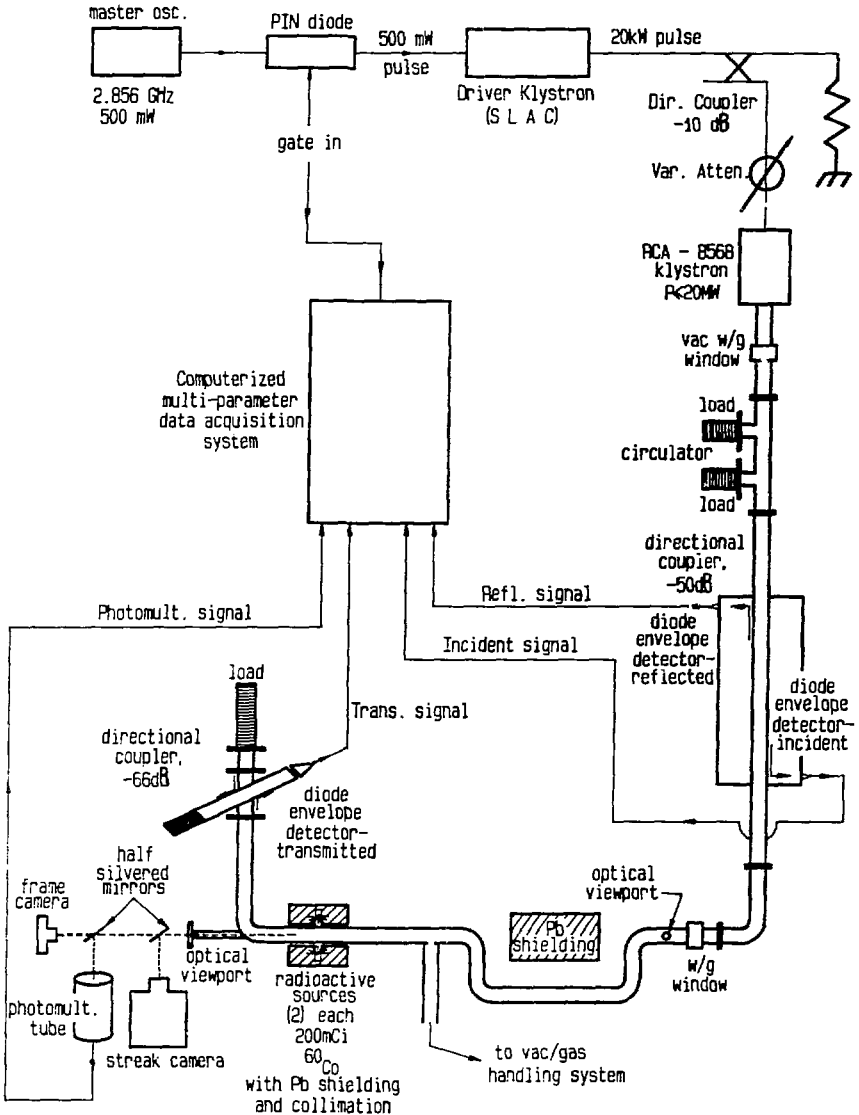
FIG. 3-1

few seconds. These pulses were amplified as high as 15 MW
peak power in two stages: first by a driver klystron and
then by an RCA 8568 klystron. The peak power of the ampli-
fied pulse could be varied from a few kW to 15 MW by attenu-
ating the output of the driver klystron and/or varying the
cathode voltage of the 8568 klystron.

After amplification by the 8568 klystron, the pulse
entered the waveguide system, the first part of which was
pressurized to 30 psig with dichlorodifluoromethane (Dupont
Freon-12) to prevent arcing. It then passed through a cir-
culator, which protected the klystron from damage due to
reflected power, and a high-directivity (37-dB directivity)
directional coupler, where the forward-traveling wave was
sampled and its envelope recorded (unless explicitly stated,
in all subsequent references to waveform detection by micro-
wave diodes, it is the envelope, not the actual rf waveform,
that is being referred to). The pulse then passed through a
waveguide pressure window and entered the test section.
From this point to the terminated end of the test section,
the waveguide contained the gas whose breakdown properties
were to be measured. Shortly after entering the test sec-
tion, the pulse reached a region where the gas contained a
small density of seed electrons, provided by ionization due
to γ-rays from two collimated ^{60}Co sources. Prior to ar-
riving at this point, the pulse was guided around lead
shielding blocks. Without this shielding, breakdown tended
to occur on the pressure window surface rather than in the

vicinity of the ^{60}Co sources. In the source region, the
pulse caused breakdown. Some energy was absorbed in
creating the discharge, some was reflected, and some was
transmitted. The reflected part of the pulse propagated
back past the upstream directional coupler, where it was
sampled and recorded, and was finally absorbed in a matched
load at the circulator. The transmitted pulse continued
down the test section, was sampled and recorded at the down-
stream directional coupler, and was finally absorbed in a
matched load terminating the waveguide test section.

As the breakdown discharge occurred, a photomultiplier
tube monitored the time development of its optical radiation
output, and a Hamamatsu C979 streak camera was used to re-
cord its temporal and one-dimensional spatial development
(two spatial dimensions were actually recorded in independ-
ent measurements). Finally, a 35-mm camera captured a time-
integrated, two-dimensional image of the discharge.

During the breakdown process, the three microwave sig-
nals and the photomultiplier signal were fed to a computer-
ized multi-parameter data acquisition system. This system
simultaneously measured and stored the peak amplitude and
time-of-arrival of all four signals, relative to a starting
trigger signal, for each breakdown event. The peak-ampli-
tude data yielded information on microwave pulse amplitude
and optical radiation output, while time-of-arrival data
yielded information on breakdown time relative to the onset

of the microwave pulse. At a fixed microwave pulse ampli-
tude and gas pressure, many breakdown measurements could be
made in a short period of time with this system, yielding
information on the statistics of the breakdown/pre-ioniza-
tion process.

Fig. 3-2 shows oscilloscope traces of detector re-
sponses for typical long-pulse breakdown experiments. Be-
cause the detector response voltages were proportional to
the square of the microwave electric field (square law), the
amplitudes of the pulses shown in these photographs are ap-
proximately proportional to waveguide power. Fig. 3-2(a) is
a negatively-rectified envelope showing the incident pulse
shape for these experiments. Fig. 3-2(b) shows the trans-
mitted pulses recorded at four different power levels and
breakdown times, with the waveguide test section at constant
pressure. At each power level, five traces were recorded;
observe the statistical variation in breakdown times, parti-
cularly for the longer, lower-power pulses. Finally, Fig.
3-2(c) shows transmitted pulses at fixed incident pulse pow-
er and varying pressures. In this figure, breakdown was
occurring on the leading edge of the 47-ns (10-90% power)
rise time pulse generated by the gated oscillator and kly-
stron. Because these transmitted pulses are not "rectangu-
lar," the analysis of this kind of data will be somewhat
different than that for pulses with breakdown times greater
than 100 ns, as will be seen in chapter IV.

Incident/transmitted detector waveforms

(a) Incident pulse
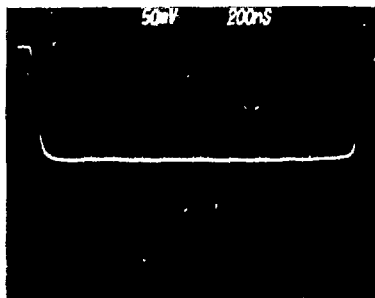
(b) Pulses transmitted after breakdown;
fixed pressure
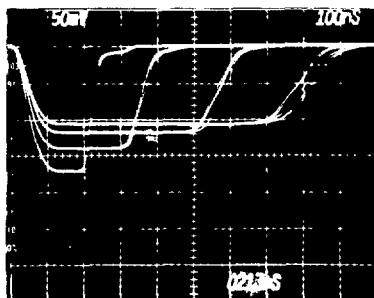
(c) Pulses transmitted after breakdown
on leading edge of incident pulse;
varying pressures
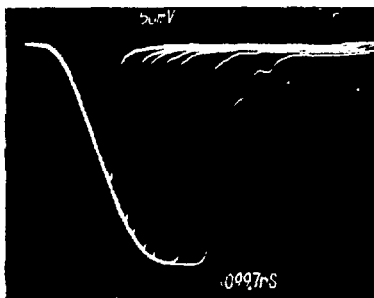
FIG. 3-2

3.2 Short-Pulse Experiments

Fig. 3-3 shows the experimental layout for the short-pulse measurements. The breakdown/propagation test section was the same in these experiments as in the long-pulse experiments, aside from a repositioning of the incident/reflected directional coupler closer to the radioactive sources. However, the microwave pulse source and the data collection system were different.

For short-pulse measurements, the source consisted of a pulse-compression cavity[18] driven by the RCA-8568 klystron. This cavity delivered 2-ns (FWHM) pulses with about 2.5-ns rise time (10-90%) and up to about 100 MW peak power to the test section (see Appendix A for pulse-compression resonator details), where breakdown took place as described in the section on long-pulse measurements.

Here, data was fed to three Tektronix 7104 oscilloscopes with 7A29 amplifiers and 7B15 time bases, where the incident, transmitted, and reflected signals were simultaneously measured and recorded with three oscilloscope cameras. Optical measurements were done exactly as described in the previous section, except that an additional photomultiplier tube, located at the pressure window viewport, was used to monitor breakdown on the waveguide window. When breakdown occurred at this window prior to occurring at the source region, the data were ignored.

The multi-parameter data acquisition system described earlier was not used in the short-pulse measurements for two

Short-Pulse Measurements - Experimental Layout
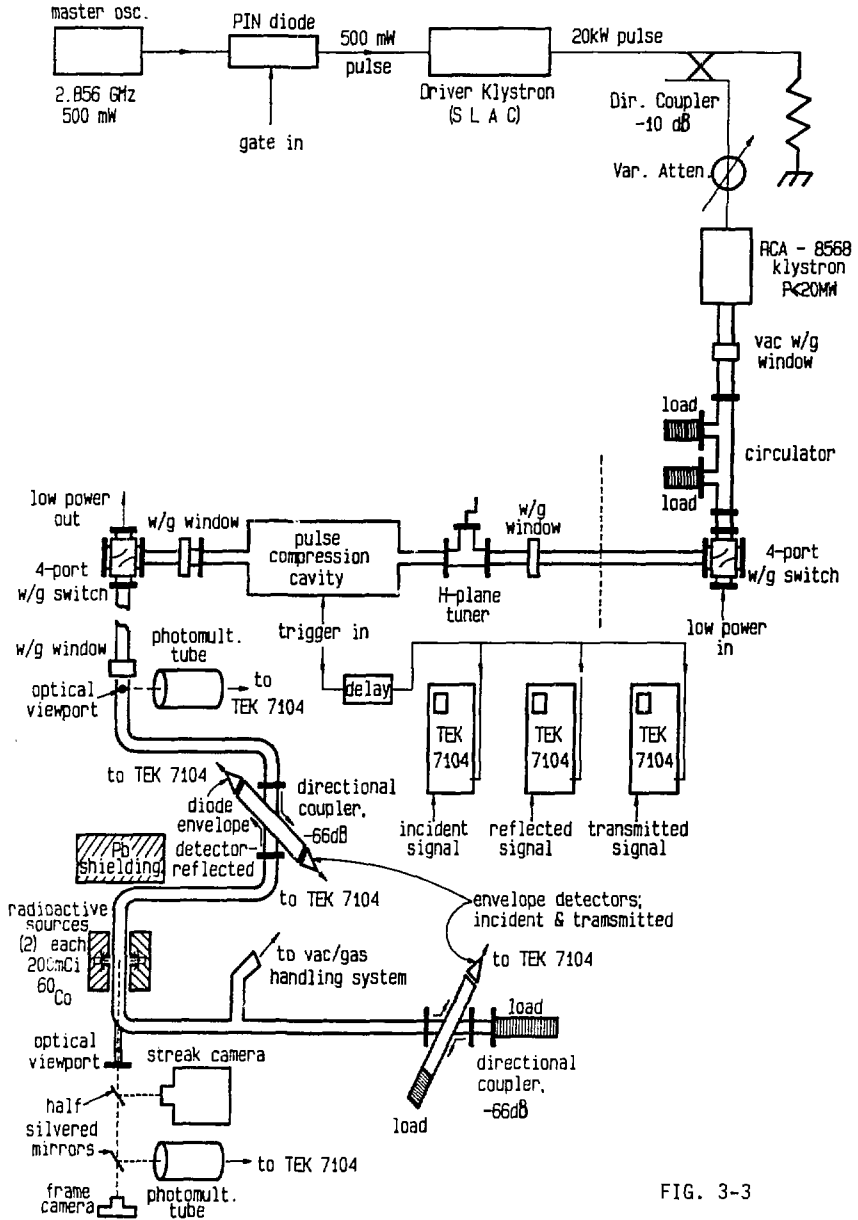
FIG. 3-3

reasons: one, statistical behavior of the breakdown wasn't observed in the pulse amplitude and pressure range studied, and two, the multi-parameter data acquisition system didn't have sufficient bandwidth to accurately measure the short-duration signals. In fact, post-acquisition signal processing was necessary to correct for bandwidth limitations present even when the fast oscilloscopes were used.

. Processing the measured waveforms corrected for two major limitations, the non-zero response time of the diode detectors and 7A29 amplifiers, and the varying frequency responses of the directional couplers used, over the bandwidth of the measured incident and transmitted pulses.

Briefly, the signal processing was carried out as follows (details can be found in Appendix A). The measured diode signal waveform, which was a convolution of the actual waveform and the diode's impulse response, was deconvolved, using standard signal processing techniques, to get an approximation to the actual waveform. The Fourier transform of the resultant waveform then yielded the frequency spectrum of the pulse. Each component in this spectrum was then corrected for the frequency-dependent coupling of the directional coupler used to sample the pulse. Finally, the inverse Fourier transform was taken to yield the pulse shape inside the waveguide. Because it was unknown, the carrier frequency spectrum had to be approximated in this procedure; this approximation is discussed in Appendix A. The other diagnostic system components, namely the cables and coaxial

attenuators, had negligibly varying frequency responses over
the pulse bandwidths, and, except for their overall atten-
uating characteristics, were ignored in the analysis.

Fig. 3-4(A) shows a typical digitized incident micro-
wave pulse obtained from an oscilloscope photograph of a
diode detector response. This was the pulse shape observed
in all the short-pulse breakdown measurements. Fig. 3-4(B)
shows the same pulse after deconvolution. In Fig. 3-4(C),
the power pulse in the waveguide derived from Fig. 3-4(A) is
shown, the derivation assuming the use of a directional
coupler with a flat, non-variant frequency response. Final-
ly, Fig. 3-4(D) shows the power envelope in the waveguide
using the deconvolved detector response shown in Fig.
3-4(B), with the frequency dependence of the directional
coupler taken into account. These results clearly show that
this type of analysis is necessary when using limited-band-
width instruments on wideband pulses: Fig 3-4(C) indicates
a peak power of 41 MW and a duration (FWHM) of 2.4 ns, while
the processed pulse in Fig. 3-4(D) shows an actual peak
power of 68 MW and a duration of 2.0 ns.

DETECTOR AND WAVEGUIDE POWER PULSE SHAPES - WITH
AND WITHOUT DECONVOLUTION
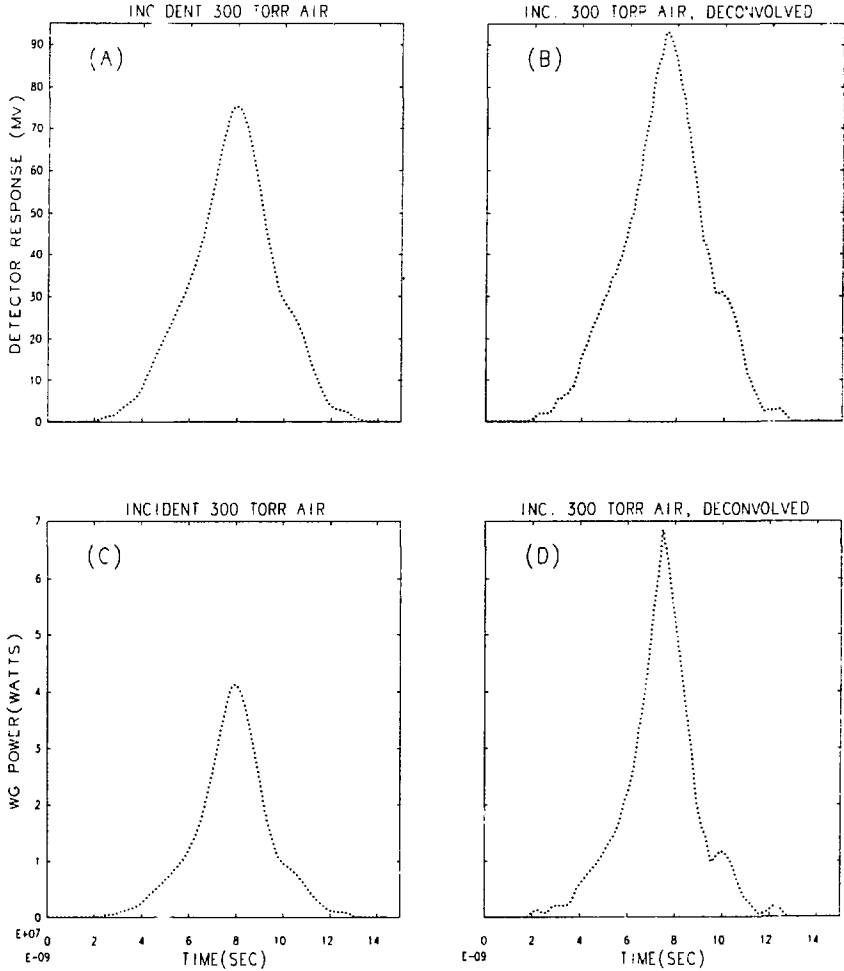
FIG. 3-4

Chapter IV - Experimental Results

This chapter is organized so that microwave breakdown
and pulse transmission data for the longest pulses investi-
gated are discussed first. The chapter then moves progres-
sively to shorter pulse results.

In Sec. 4.1, the results of breakdown measurements
using traveling wave pulses of ≥100 ns duration, which we
call long-pulse results, are presented and compared with
microwave breakdown measurements made in resonators by Tet-
enbaum, et al.,[5] and microwave breakdown "data" derived from
DC breakdown measurements[15] by Felsenthal.[19]

In Sec. 4.2, we move on to the short-pulse data, de-
fined such that breakdown occurs less than 100 ns after the
application of the microwave pulse. We first discuss the
results of measurements in which the gas broke down during
the rise time of the klystron-generated pulse, 10 to 100 ns
after the onset of the pulse. The same experimental setup
was used in these experiments as in the long-pulse experi-
ments, as described in Chapter III, but according to the
above definition, we consider the data to be short-pulse
data. These results are compared with non-self-consistent
swarm-theory calculations. Sec. 4.2 concludes with a dis-
cussion of breakdown and transmission measurements made
using pulses generated by the pulse-compression cavity. In
these measurements, breakdown occurred in less than 5 ns,

i.e., at some time during the 2-ns (FWHM) duration pulse.
The results are compared with simulations using the 2-D
fluid model.

Finally, Sec. 4.3 summarizes the experiments and dis-
cusses the conclusions that were drawn.

4.1   Long-Pulse Results

When microwave breakdown field measurements, at a given
pulse length, are made on a gas as a function of pressure,
one finds that the breakdown field has its smallest value at
pressures of several torr for S-band microwaves, typically.
The breakdown field increases as the pressure is raised or
lowered away from this minimum. At pressures below 1 torr,
free electrons rarely undergo collisions; they oscillate
out of phase with the microwave field and energy transfer
from the field to the electrons is inefficient. At high
pressures, electrons collide so often with gas atoms or mol-
ecules, and spend such a small fraction of the time gain-
ing energy from the field, that few reach high enough
energies to ionize gas atoms or molecules and initiate a
breakdown avalanche. On the other hand, at pressures of a
few torr, the electron-neutral collision frequency is rough-
ly equal to the microwave frequency, and energy couples well
from the field to any unbound electrons present. If weak
pre-ionization sources are used in breakdown experiments,
free electrons may not be available during the application
of the pulse, and the results will be statistical; for a

given field amplitude and pressure, the gas will not always
break down at the same time. The ^{60}Co sources used in the
experiments described here provided sufficient ionization
for reproducible results at pressures near the breakdown
minimum, but at high and low pressures breakdown time dis-
tributions were measured because the results were statisti-
cal.

Figs. 4-1 and 4-2 show distribution data for microwave
pulse breakdown times in air and nitrogen at high pressure,
a pressure near the breakdown minimum, and at low pressure.
These data were obtained by repeatedly making the same
breakdown-time measurement at fixed pressure and pulse am-
plitude, using incident pulses of 1.8-µs duration. The
breakdown time was defined as the difference in time between
the onset of the incident microwave signal and the appear-
ance of a reflected microwave signal. The onset time, or
zero time in the figure histograms, was the time at which
the incident pulse reached 10% of its maximum value at the
radioactive source position where breakdown took place. The
breakdown time in the histograms was the time when the re-
flected microwave signal reached 10% of its maximum value at
the source position. The incident pulse power had a 60-ns
(10-90%) rise time in these experiments; the reflected
power rise time was typically several nanoseconds, though it
varied with pressure from a minimum of a few nanoseconds at
low pressure to a maximum of 15-20 ns at high pressure.

Other authors have defined the breakdown time as the
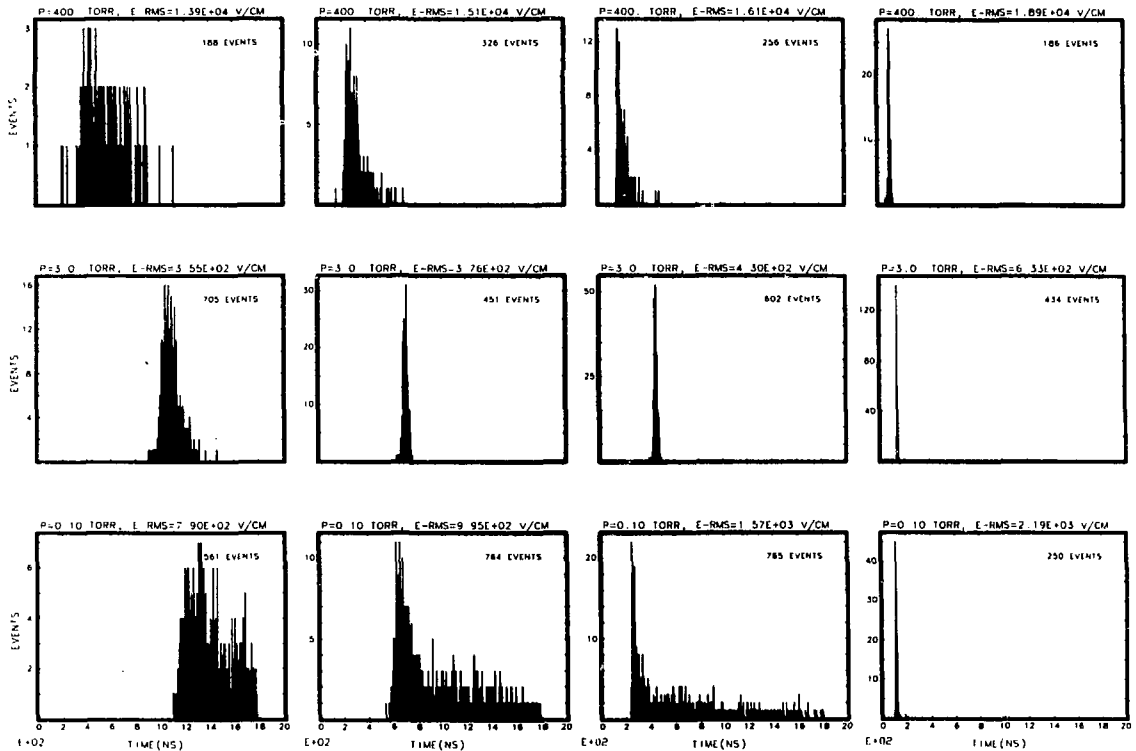
FIG. 4-1 - <u>Distributions of times-to-breakdown in air</u>. From repeated measurements at constant pulse amplitude and pressure. Incident pulse duration = 1.8 μs, total abscissa range = 2 μs. Fields are rms fields at the center of the waveguide.
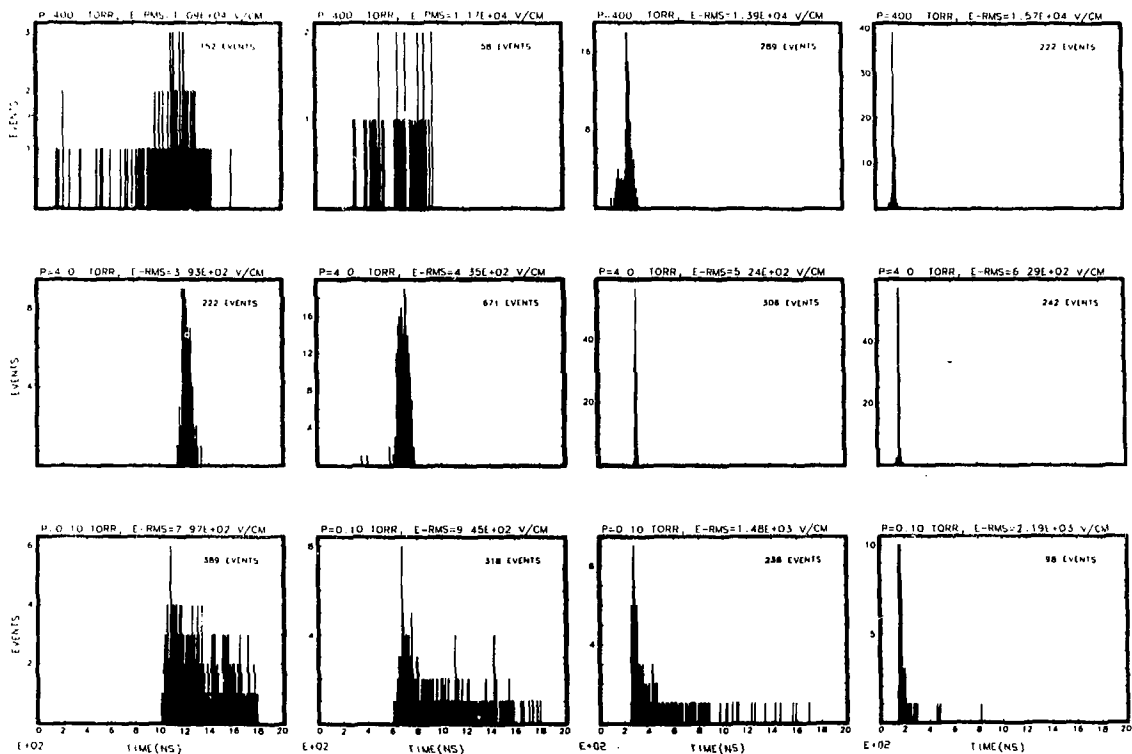
FIG. 4-2 – <u>Distributions of times-to-breakdown in nitrogen</u>. From repeated measurements at constant pulse amplitude and pressure. Incident pulse duration = 1.8 µs, total abscissa range = 2 µs. Fields are rms fields at the center of the waveguide.

time, after pulse application, at which the breakdown plasma
begins to radiate light at optical wavelengths, as measured
with a photomultiplier tube.[16] Photomultiplier tube mea-
surements done in the present experiments showed that at
fields for which breakdown occurred in less than about
100 ns, no measureable difference (within about 2-ns instru-
ment resolution) was observed in breakdown times determined
from the onset of radiated light and times determined from
reflected microwave signals. For the longer pulses, though,
the onset of optical emission from the breakdown plasma pre-
ceded microwave reflection significantly, particularly at
higher pressures. That is, optical ratiation was emitted at
electron densities well below those required to affect mi-
crowave pulse transmission. At 400 torr in air, for break-
down times of the order of 1 to 1.2 µs (measured using the
reflected microwave pulse), radiation preceded reflection by
over 200 ns. Because the photomultiplier tube used was sen-
sitive to a broad band of optical radiation and not just a
single spectral line, and because microwave pulse transport
in waveguide could be related to free-space transport (Chap-
ter II, Sec. 2.2), microwave reflection was considered a
more appropriate criterion for breakdown than optical emis-
sion.

The distributions in Figs. 4-1 and 4-2 show character-
istics one observes in the results of gas breakdown measure-
ments made with both DC and alternating fields using weak
pre-ionization sources, namely the existence of a formative

time delay and statistical time delay, prior to breakdown, as indicated in Fig. 4-3. The formative time is the time it takes for an avalanche to develop, given the presence of one or more free electrons during the initial application of the field, and is usually considered to be constant at a given field strength and pressure. Actually, it is not a constant; the formative time can be decreased by strongly increasing the pre-ionization. Statistical time delay is caused by the finite rate of free-electron generation from pre-ionization sources. In DC discharges, the statistical generation of electrons by cathode field emission or photo-emission, negative ion detachment, and cosmic rays can also contribute to the statistical time.

The histograms in Figs. 4-1 and 4-2 are very different at different pressures and field strengths. At high and low pressures, in the top and bottom rows of the figures, the spread in the time distributions is larger than at the intermediate pressures, where the microwave frequency is about equal to the collision frequency ($\omega \approx \nu$). At the lower pressures, the distributions are broad because free electrons from the pre-ionization sources were scarce (see Appendix B); one or more electrons were not always present at the time the pulse was applied. At the high pressures more electrons were present, but because of the high collision rates, few reached energies high enough to cause ionization after the application of the field; indeed, only a statistical fraction of them reached energies higher than 2 or

FORMATIVE AND STATISTICAL TIMES IN MICROWAVE BREAKDOWN
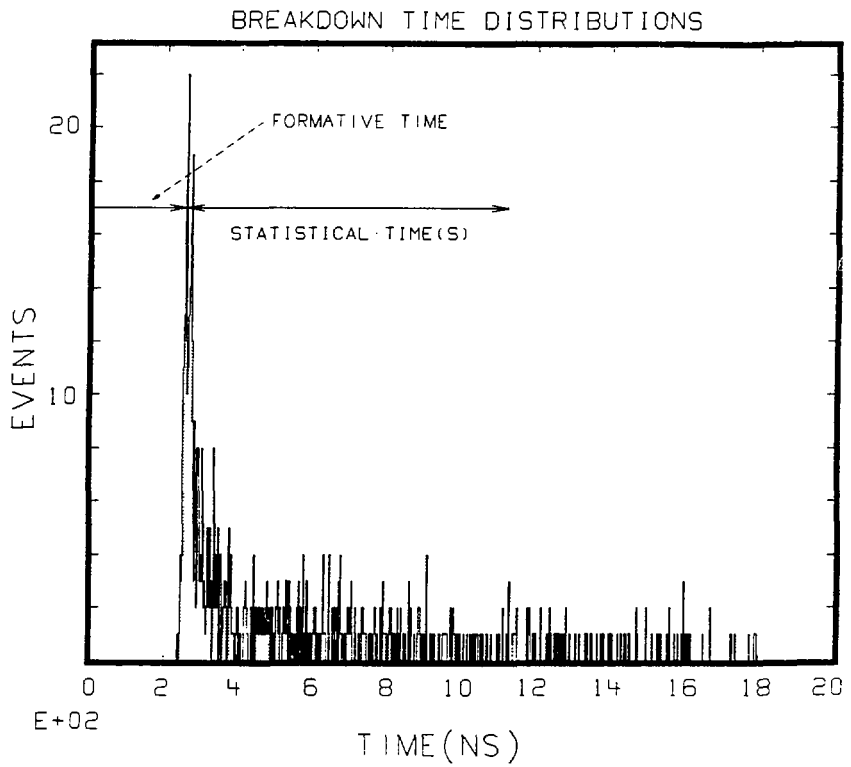
FIG. 4-3

3 eV. As the field was increased (from left to right in the figures), however, the average oscillation energy increased, and a larger fraction of the total number of available free electrons attained energies high enough to cause ionization. Thus at all pressures, the distributions are narrower at higher fields (the lowest-field distribution at 0.1 torr **appears** narrower than the one at the next highest field because the incident pulse was only 1.8-µs long). The pre-ionization sources produced electrons with an exponential time distribution, and the histograms in Figs. 4-1 and 4-2 qualitatively exhibit this character, particularly at low pressures. At high pressures the energy statistics, as dis-cussed above, were more important than the source statistics, and in air, the statistics of electron detachment from negative ions (see Appendix B) also contributed. At all pressures, the presence of a non-uniform field in the wave-guide may also have affected the statistics.

In most of the earlier work on long-pulse air break-down, strong enough pre-ionization sources (e.g., uv radia-tion from a spark-gap) were used that breakdown always oc-curred at the same time for a given field strength; the measurements were purposefully made under conditions that eliminated statistical effects. In order to compare the present long-pulse results to those of earlier investiga-tors, particularly those of Tetenbaum et al.,[5] the effects of statistics had to be removed. In Fig. 4-4, the measured breakdown time thresholds are plotted vs rms electric field

Long-Pulse Fields vs Breakdown Times in Air and Nitrogen
Dashed lines are smooth curves drawn through the
threshold data points for air. Note scale factors
at *bottom* left in the plots.
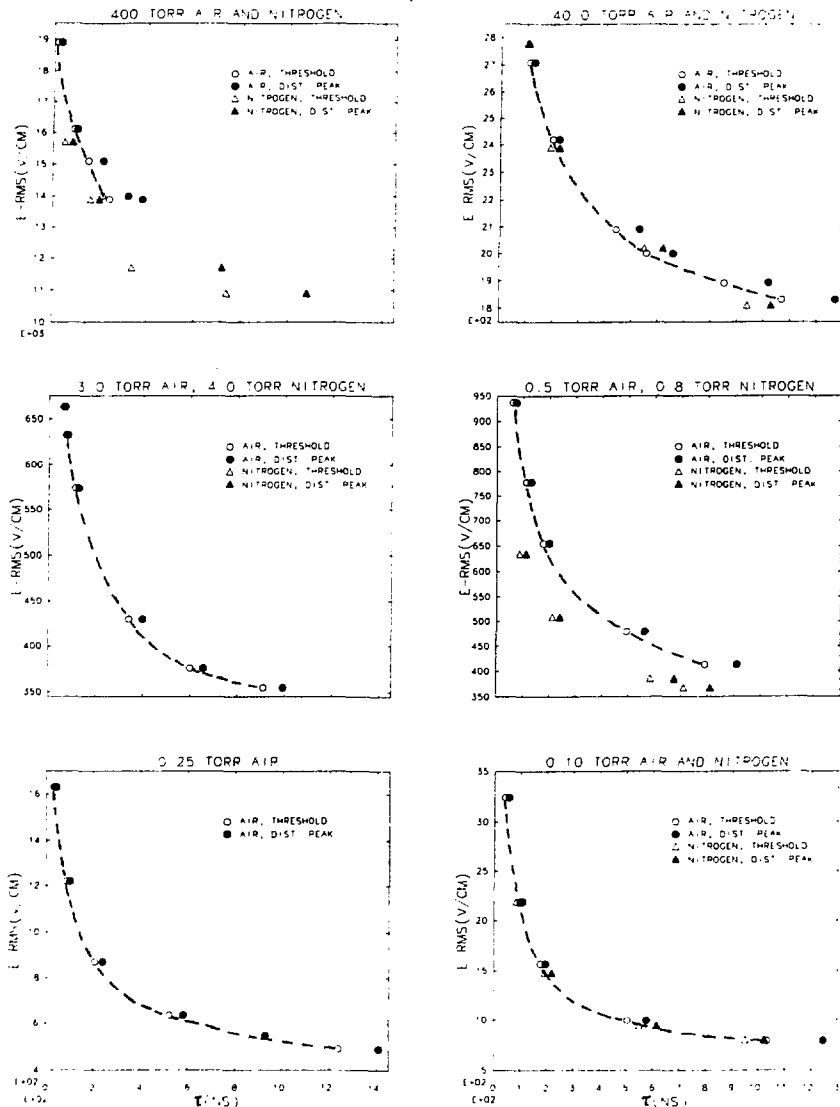
FIG. 4-4

for air and nitrogen at several pressures. The threshold
times are defined as essentially the earliest breakdown
times in the distribution envelopes. That is, for a given
field, 99% of the pulses broke down at or after this thresh-
old time. For comparison, the peaks in the distributions,
or the most probable breakdown times **in this experiment,** are
also plotted. According to convention, the time axis is
labeled τ in the plots. To compare these results to those
reported in Ref. 5, the threshold times have been renorma-
lized to a zero time at which the incident pulse has reached
a power level 90% of its maximum value, i.e. the times are
60 ns shorter than those in Figs. 4-1 and 4-2.

If smooth curves are drawn through the threshold data
for air or nitrogen (this was done for the air data in Fig.
4-4), one can see that the breakdown field for any pulse
length between about 50 ns and 1200 ns can be interpolated.
At that field a pulse of that duration and no longer can be
transmitted without breakdown if free electrons are present.

The above procedure was followed for 100-, 200-, and
600-ns pulses in air and nitrogen; Fig. 4-5(A) shows the
results for air and Fig. 4-5(B) the results for nitrogen,
while Fig. 4-5(C) shows an overlay of the two. In Fig.
4-5(D), the results for air are compared with the 3-GHz mi-
crowave breakdown data of Tetenbaum et al.[5], and the 100-ns,
3-GHz predictions of Felsenthal,[19] who used the effective-
field formalism to convert video pulse breakdown data[15] to
microwave breakdown "data". Tetenbaum et al., used the same

Breakdown Fields vs Pressure for 100-, 200-, and 600-ns Pulses
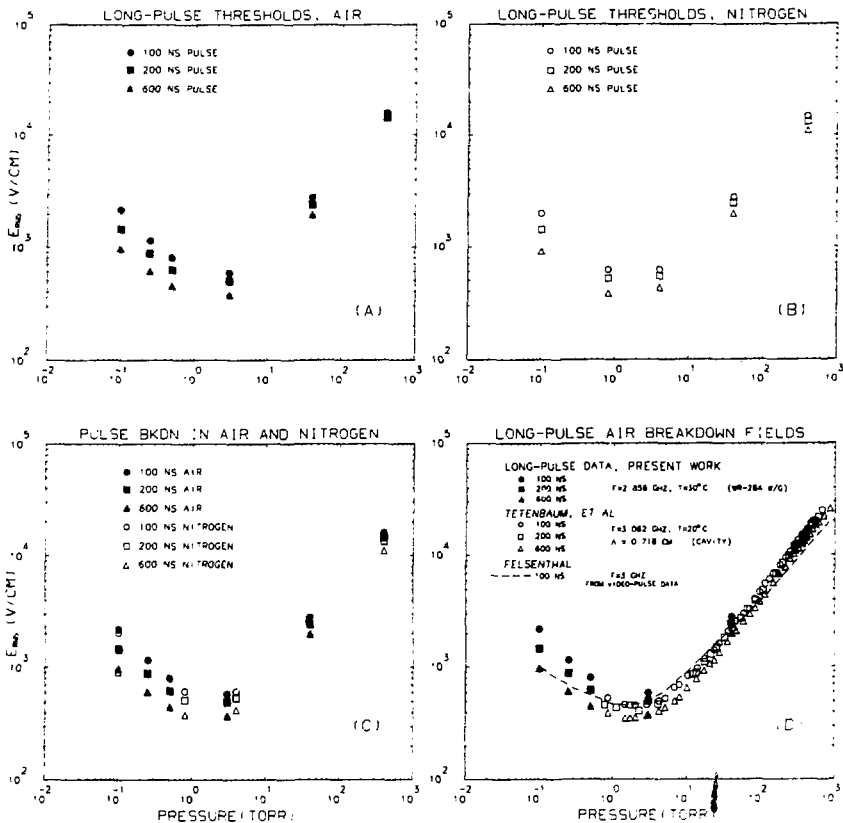
FIG. 4-5

zero-time value for their pulses as was used here, namely
the time when the pulse reached 95% of its maximum field
(90% of its maximum power). Felsenthal and Proud's DC pulse
rise time was < 1 ns.[15]

The agreement with the 600 ns data of Tetenbaum et al.
is excellent, and is within the combined experimental uncer-
tainty, in the present experiments, of 6% (see Appendix A).
For 200-ns pulses, the agreement is within 10% above 10
torr, but their data is 15% lower at 3 torr, near the break-
down mimimum. The two data sets are clearly different for
100 ns pulses: at 40 torr their data is 20% lower and at 3
torr it is 25% lower. Felsenthal's "data" is also much low-
er at low pressure, more than a factor of two at 0.1 torr.

The probable reason that poor agreement with the Tet-
enbaum data was found at the shorter pulse lengths can be
understood by referring to Fig. 4-6. In the figure, the
E-field envelope rise time of the klystron-generated pulses
used in the present work are compared with the shortest E-
field rise times one could obtain in critically coupled cav-
ities with unloaded Q values of 840 and 1110. These were
the unloaded Q values of the TM_{010}-mode resonators used by
Tetenbaum et al., in their breakdown measurements. Since
they used the same zero-time value for their pulses as does
the present work (the time the E-field reached 95% of its
maximum amplitude), one sees that if one compares the cavity
and klystron pulse rise times in Fig. 4-6, and assumes that
the breakdown-time measurements were the same in both exper-

Pulse Rise Time Comparisons; Cavities Used By
Tetenbaum et al.[5] and RCA 8568 Klystron

NORMALIZED E-FIELD TIME DEPENDENCE

LONG-PULSE S-BAND MEASUREMENTS

P_{MAX} = 15 KW
P_{MAX} = 580 KW

F=2.856 GHZ
KLYSTRON PULSES IN WR-284 W/G; MEASURED

TETENBAUM, ET AL. Q_0 = 840; Λ = 0.391
Q_0 = 1110; Λ = 0.718
F=3.062 GHZ, CRITICALLY COUPLED CAVITIES
CALCULATED PULSE SHAPES

E(T)/E-MAX
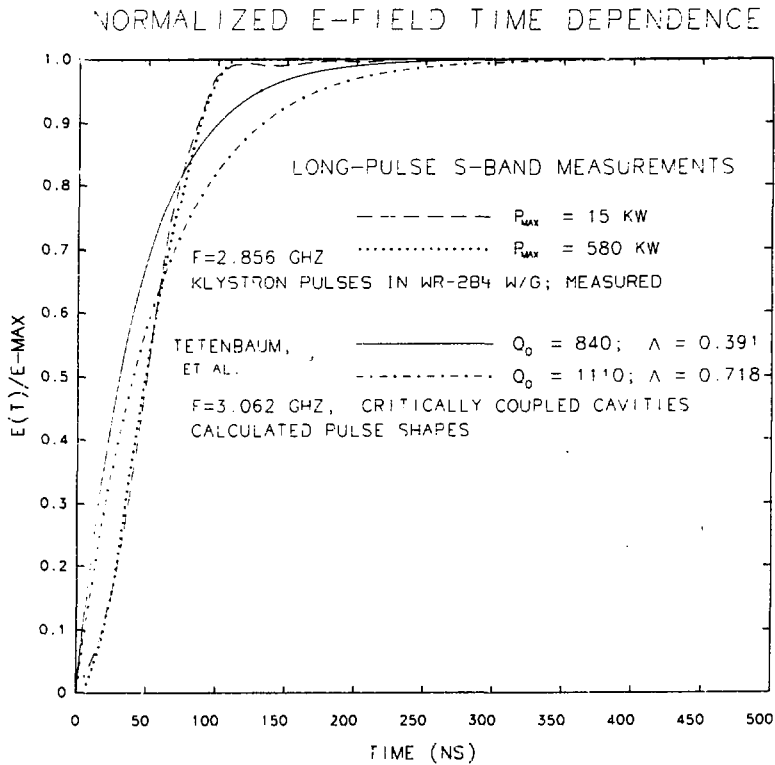
TIME (NS)

FIG. 4-6

iments, then the pulses of Tetenbaum et al., contained more energy, when integrated over their slower rise times. The agreement of the two experiments for 600-ns pulses, and the different results obtained as the pulse lengths got shorter, suggest that the assumption of Tetenbaum et al., that a pulse only contributes to breakdown when its E-field is greater than 95% of its maximum amplitude, only applies when the rise time is a small fraction of the total pulse length.

Differences in the data from the present work and the Felsenthal "data" in Fig. 4-5 can also be attributed, in part, to rise time differences. For this reason, the threshold and peak breakdown time data, with zero-times normalized to the time the pulse reached 10% of its peak power (60-ns longer than the times in Fig. 4-4) are recast in Fig. 4-7. In this figure, the data are plotted on an E_{eff}/p vs $p\tau$ plot, where p is the pressure and τ the pulse length, and the microwave breakdown fields have been converted to effective field using equation 2.11b with $\nu_m = 5.3 \cdot 10^9 p$. For comparison, the average video pulse data of Felsenthal and Proud are included. For values of $p\tau \gtrsim 10^{-7}$ torr·sec, the agreement is within 10%. At low pressures, the collision frequency is not independent of energy, and at low values of τ, the microwave-pulse rise time was a significant fraction of τ. Thus at low values of $p\tau$, the agreement is expected to be poor.

The failure of the effective field concept at low pressures is, as discussed in Chapter II, well known. The re-

Comparison of Long-Pulse Data with DC Data
via the Effective Field
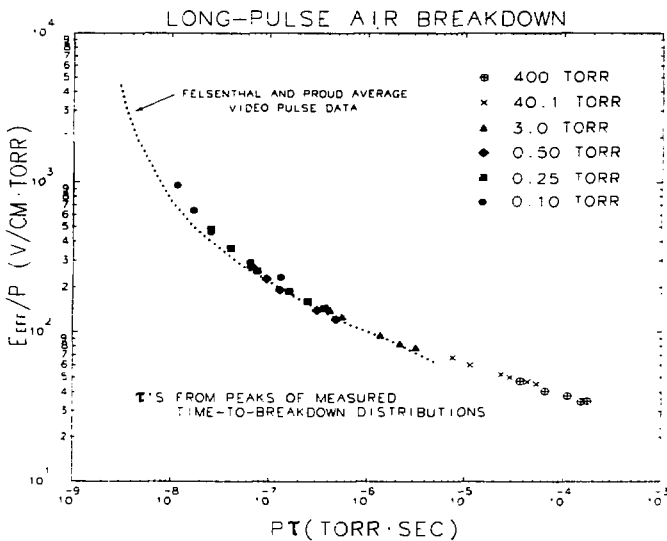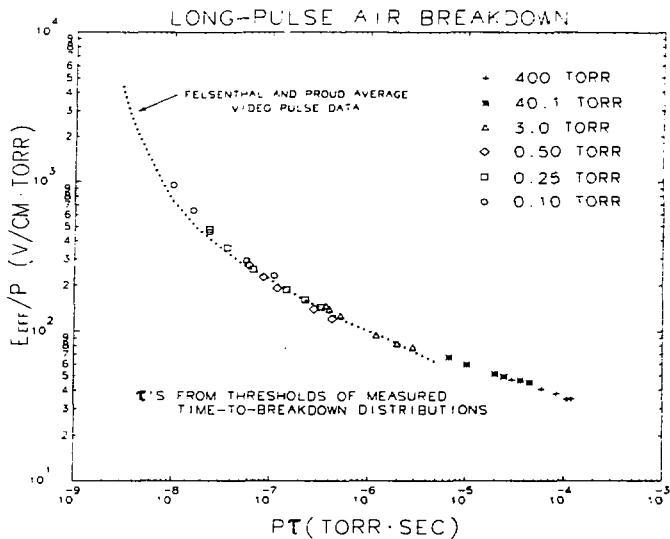
FIG. 4-7

sults and comparisons of this section indicate that to accu-
rately describe microwave breakdown data, one must also ac-
count for the actual time variation of the field envelopes,
in addition to the energy dependence of the collision fre-
quency, particularly for short pulses. For this reason, the
fluid and swarm theories, as discussed in Chapter II, will
be used to interpret the rest of the breakdown/transmission
data, in which breakdown occured in less than 100 ns.

4.2   Short-Pulse Results

4.2.1   Breakdown on the Leading Edge of the 47-ns Rise Time Pulse

In this section, we consider the results of breakdown
measurements in which breakdown occurred during the rise
time of the pulse generated by the klystron, i.e. on the
leading edge of the pulse. Tuning was performed to shorten
the rise time from 60 ns to 47 ns for these experiments.
For these pulses, comparisons to earlier microwave breakdown
measurements or the cascade theory breakdown condition de-
scribed by equation 2.13 were of questionable utility since
the pulse shapes were more triangular than rectangular [see
Fig. 3-2(C)]. In this section, swarm theory simulations,
which account for the time dependence of the fields, are
used to interpret the data. However, the swarm equations,
as described in Chapter II, do not in themselves account for
effects associated with the discharge and waveguide geome-
tries. The model of a plasma-post in a waveguide, also de-

scribed in Chapter II, approximately allows for these ef-
fects, and is used in conjunction with the swarm equations.
This model requires, of course, knowledge of the size of the
"post"; that information can be determined from time-inte-
grated photographs such as those shown in Fig. 2-2. One
should first establish, however, that the use of the post
model is reasonable in a dynamical sense, even early in time
when the plasma discharge is in its development stages.
Since the time-integrated photographs in Fig. 2-2 did not
provide dynamical information, streak photography was per-
formed on the discharges to examine their time development
and its relationship to the effects of breakdown on the mi-
crowave fields. The first part of this section will be de-
voted to the results of these optical measurements and their
interpretation.

The time development of the optical radiation from
breakdown plasmas in air and nitrogen is indicated in the
streak photographs in Fig. 4-8. These are streaks of micro-
wave breakdown discharges which occurred on the leading edge
of the klystron pulse, as in Fig. 3-2(C). The view, through
the streak camera, of the region where breakdown took place,
was along the waveguide axis, toward the microwave source.
Fig. A-5, and the discussion in Sec. A-4 of Appendix A, will
aid the reader in understanding how the streak photographs
were recorded. In the photographs, either the entire two-
dimensional image of the breakdown region, or a nearly one-
dimensional portion of it, was swept across the film. The

Streak Photographs of Waveguide Breakdown in Air and Nitrogen

<u>10-ns Axial Slit Image Streaks</u>

(a) 5 torr   (b) 200 torr   (c) 200 torr

Air

100 shots   1 shot   100 shots

(d) 1 torr   (e) 100 torr   (f) 200 torr

Nitrogen

100 shots   1 shot   100 shots
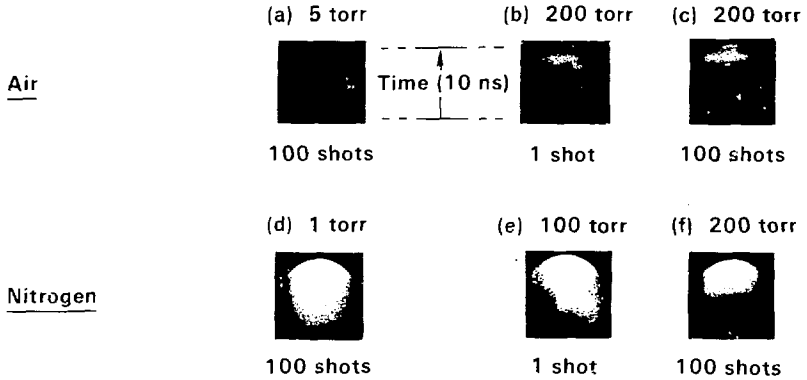
<u>10-ns Radial Slit Image Streaks</u>

(g) 3.5 torr   (h) 0.8 torr   (i) 200 torr

Air

1 shot   12 shots   1 shot

(j) 1 torr   (k) 1 torr   (l) 200 torr

Nitrogen

1 shot   10 shots   1 shot
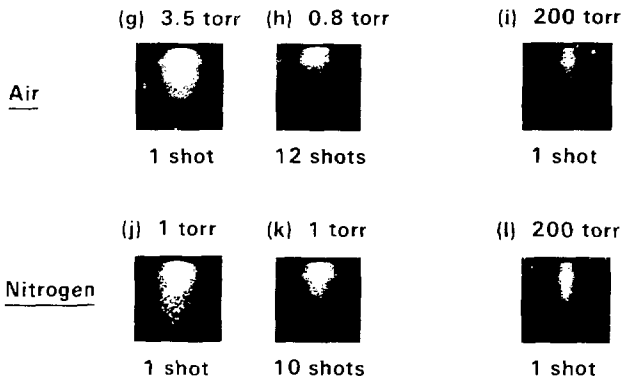
<u>10-ns Whole-Image Streaks (no slit)</u>

(m)   (n)   (o)

200 torr Air

1 shot   1 shot   1 shot
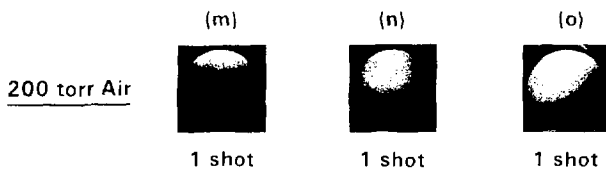
FIG. 4-8

sequence of events that resulted in the photographs in Fig.
4-8 was as follows: before the discharge developed, the
image of the breakdown region (or a portion of it) was fo-
cused onto the streak camera film plane, but outside the
area occupied by the film. In each of the photographs in
Fig. 4-8, the image was initially focused just below the
bottom edge of the photographs. The camera was then trig-
gered just before breakdown took place, and the breakdown
region image was swept across the film (from bottom to top
in the photographs) as the plasma began to radiate, crossing
the portion of the film shown in the photographs in 10 ns.

The photographs fell into three catagories, depending
on the orientation of the plasma in the photographs, and the
portion of it that was imaged and streaked: whole image
streaks and independent streaks of two one-dimensional por-
tions of the plasma (portions masked by a slit), mutually
orthogonal to each other and to the direction of microwave
pulse propagation. In the "axial" streaks in Fig. 4-8, a
narrow, central portion of the plasma-column, along its ax-
is, from one broad waveguide wall to the other, was imaged
on a slit. The image of the slit, horizontal in the photo-
graphs, was then swept upward across the film. Thus in
these photographs, the plasma column axis, and the E-field
direction in the waveguide, are from left to right. In the
"radial" streaks, the slit image is also horizontal in the
photographs, but the portion of the plasma imaged was radial
to the column axis, centered in the waveguide, and ran from

the center of the waveguide to about half the distance from
the center to the narrow walls, in opposite directions. The
left-to-right spatial dimension in these streaks was thus
perpendicular to the plasma column axis and electric field,
and was centered between the waveguide broad walls. In the
whole-image streaks, the plasma column axis and the direc-
tion of the E-field also lies from left to right in the
photographs, but the entire image, not just a slit-masked
portion, were streaked.

Several streaks are shown in Fig. 4-8 for each of the
three catagories. For the radial and axial slit images,
streaks are shown at low pressures, of the order of 1 torr,
on the left side of the figure, and at pressures of 100-200
torr on the right. Where possible, only single exposures,
corresponding to one breakdown event, are shown. When the
light intensity emitted from the plasmas was low, however,
multiple exposures were necessary, and these can only be
interpreted in an "averaged" sense. The bright horizontal
bands seen in the upper half (late in time) of many of the
photographs were a streak camera artifact, not a character-
istic of the development of the discharges. Also, the expo-
sure level varies from one photograph to another; they were
not all the same.

Three things can be concluded from these streaks. We
will state these conclusions, and then discuss the photo-
graphs in detail, to indicate how they were reached. First,
though breakdown may have developed from one or more loca-

lized spots where free electrons were initially present, the discharges were fully developed, all the way across the waveguide, within 5 to 10 ns. They did not remain localized for more than a few nanoseconds. Second, the plasma developed, at high pressure, at a speed of about $3 \cdot 10^8$ cm/sec in the direction of the E-field (actually, the plasma did not move; the motion was of the ionization front). Third, the radioactive sources used for pre-ionization produced a slightly higher initial electron density near the inner waveguide walls than in the central region of the waveguide.

The whole image streaks shown in photographs (m), (n), and (o) in Fig. 4-8 show how the plasma rapidly developed across the entire waveguide, even at high pressure where the electron mean free paths were less than 10^{-4} cm. Any evidence of localization about isolated, initial free electrons rapidly disappeared, within 10 ns. If it hadn't, vertical lines, whose width would be determined by the degree of localization, would appear in the streak photographs. Instead, the plasma developed uniformly along the plasma column exis, except in (o), where it started in the waveguide center and moved toward the waveguide walls (to right and left) within 5 ns.

In the axial slit image streaks (b) and (e), we see that the center of the plasma column axis began to radiate through the slit first. As the plasmas developed, portions along the column, nearer and nearer to the waveguide wall (along the E-field direction) began to radiate. At the end

of the sweep, the entire central portion of the column was radiating uniformly. Thus, in these photographs, breakdown initiated at the waveguide center and the ionization front moved to the waveguide walls within 4-7 ns. Since the center of the guide was 1.7 cm from the walls, the ionization front velocity, along the E-field direction, was 2 to $4 \cdot 10^8$ cm/sec. The low-pressure plasmas were too dim to measure this velocity with a single-shot streak, but photogragphs (a) and (e) show that the column axis began to radiate uniformly, when averaged over many shots, even faster, say in perhaps 2-4 ns. The radial streaks can also be used to determine ionization front velocities, in this case toward the narrow waveguide walls, perpendicular to the E-field direction. At the higher pressures, the plasmas radiated almost uniformly across the column radius. The column diameter was almost constant in time, and the plasma was within the region where the E-field was fairly uniform [photographs (i) and (l)]. At low pressure, though, the plasmas initially radiated from the high field region in the center of the waveguide and later began radiating in regions away from the center, toward the narrow waveguide walls. Photographs (g) and (j) suggest a radial propagation velocity slightly lower than the axial one, about 1 or $2 \cdot 10^8$ cm/sec.

Photographs (c) and (f) show the only qualitative difference between air and nitrogen observable in the streaks. These multi-shot pictures show that, on the average, breakdown in nitrogen is initiated near the waveguide walls [on

the left and right sides of photograph (f)] and moves into
the waveguide interior within 1 or 2 ns. Air streaks, such
as the one in (c), showed a more uniform development, on the
average. The reason for this is that the O_2 molecules in
the air rapidly attached electrons generated by the ^{60}Co
sources. Nitrogen, being non-attaching, retained a "memory"
of ^{60}Co-produced primary electrons as they passed through
the gas, reminiscent of a cloud chamber. This memory of
ionization tracks in nitrogen is also evident in the time-
integrated photographs in Fig. 2-2, in which breakdown along
the tracks is clearly visible. Apparently, the tracks have
higher ionization densities near the waveguide walls because
of secondary emission. The theoretical models for breakdown
to be discussed later in this chapter do not account for
secondary emission or other wall effects, but the effects
seem to be small; there was little evidence of track memory
in air.

If breakdown occured in times longer than about 100 ns
after the application of the klystron-generated pulse, the
onsets of the photomultiplier and reflected microwave sig-
nals were not coincident, as noted in Sec. 4.1. As the
times-to-breakdown got below 50-100 ns, however, it became
increasingly difficult to resolve the difference in the time
of onset of the reflected power and photomultiplier signals
with the equipment used; the plasma began to radiate within
1 or 2 ns of the time the microwaves were reflected. This
was also clear from transmitted power measurements that were

recorded simultaneously with the streak photographs. The
first discernible drop in transmitted power [see Fig.
3-2(C)] coincided with the appearance of optical radiation
in the streak photographs, within 2 ns. Thus the plasma did
develop cylindrically, even at early times, and did not re-
main localized about initiating free electrons. Its devel-
opment, as indicated by its emission of optical radiation,
coincided with the cut-off of microwave transmission, and
the plasma post model provides a reasonable approximation to
the discharge geometry. The approximation does ignore the
dynamics of the first few nanoseconds of discharge develop-
ment, but the effects of the plasma on the microwave fields
at these early times are small.

The microwave breakdown data for these pulses were ob-
tained similarly to those for the longer pulses, except that
the incident pulse was kept at a fixed amplitude, namely
12.6 MW, while the pressure was varied. In this case, re-
peated measurements at a given pressure resulted not only in
a distribution of breakdown times, but in a correlated dis-
tribution of breakdown field strengths, because most pulses
broke down during the pulse rise time, and the transmitted
pulse amplitude varied. The spread in the measured break-
down field distributions at 0.1 torr and at 500 torr, where
breakdown occurred after the pulse reached its maximum power
(12.6 MW), and not during the rise time, was small;   in
those cases, the field and time distributions were not
strongly correlated. At those two pressures, $\Delta E/E_{pk}$, where·

E_{pk} was the E-field at the peak of the field distribution
and ΔE was the half-width of the distribution, was < 3%. At
the intermediate pressures, where breakdown occurred during
the pulse rise time, the field distribution spreads were
much larger (up to 35% at 0.25 torr where initiating elec-
trons were scarce). Since statistical spreads were measured
in **both** the field at breakdown and in the times-to-break-
down, the results of these measurements will be presented
somewhat differently than for the longer pulses discussed
earlier.

In Fig. 4-9, the data from the measured distributions
is shown, cast in such a way that at a given pressure, only
two quantities are shown: the peak in the distribution of
breakdown fields, represented by the data point, and the
peak in the distribution of breakdown times, represented by
the number adjacent to the data point. These quantities
thus represent the most probable breakdown field and time at
a particular pressure, given the pulse used.

The times indicated in Fig. 4-9 are time distribution
peaks as measured by a photomultiplier tube viewing the
breakdown region. Photomultiplier signals, rather than re-
flected microwave signals, were used to measure the time
distributions for two reasons: one, the onset of optical
radiation and microwave reflection by the breakdown plasma
were nearly coincident, as mentioned earlier (the time dif-
ference was not measureable with the data acquisition system
used), and two, the amplitude and timing of the reflected

Swarm Theory vs Experiment - Breakdown During
the Rise Time of the 47-ns Rise Time Pulse
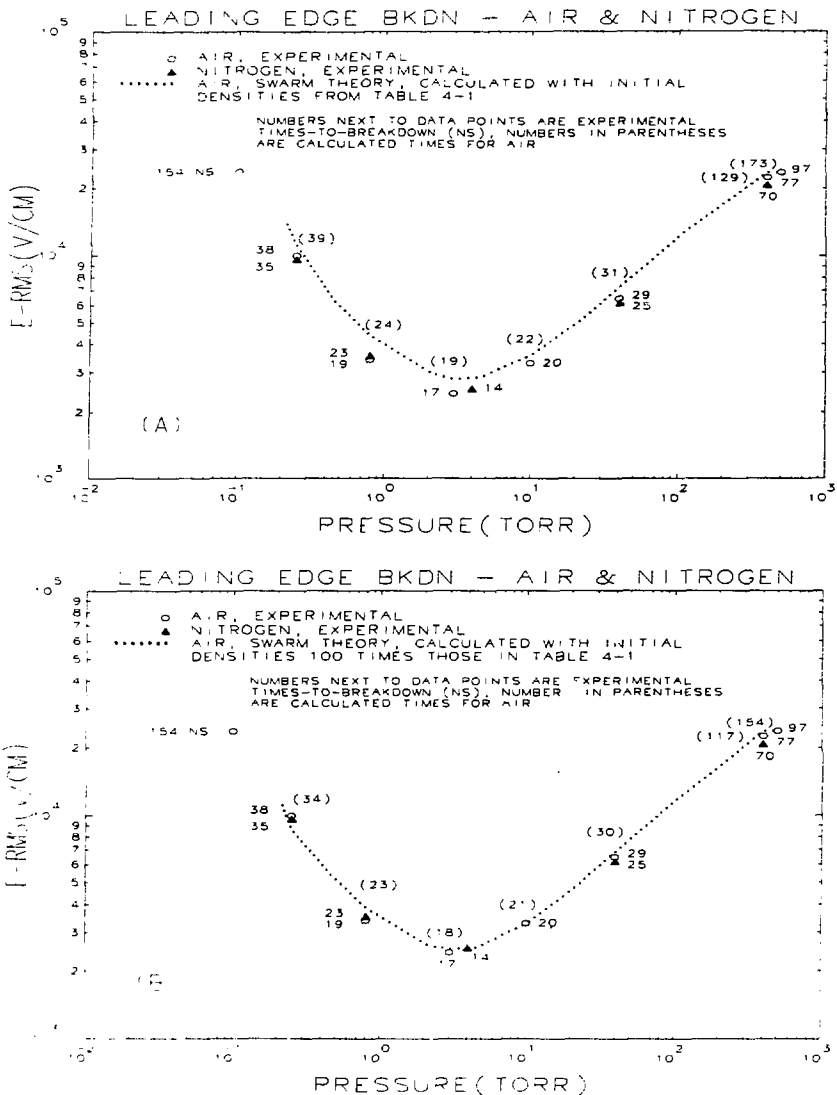
FIG. 4-9

microwave signals were not reproducible, because of random multiple reflections and attenuation at these high field levels. Constant-fraction time discrimination was not possible for these short pulses, as it was for the longer pulses; the times measured were relative to the first discernible increase of the incident pulse leading edge (the 0% time rather than the 10% or 90% time used on the long-pulse measurements), and were thus susceptible to errors of the order of 2-3 ns.

The theoretical curve for air shown in Fig. 4-9 was obtained by solving the swarm equations 2.22, 2.23, and 2.24 numerically, using the collision rates shown in Fig. 2-6. The numbers in parentheses are breakdown times predicted by this calculation, for those pressures at which experimental data were taken. Equation 2.22 was modified to account for diffusion and attachment; v_i was replaced by $v_i - v_a - D/\Lambda^2$. The electron energy dependent diffusion constant used was[1] $D = 2.2 \cdot 10^5 \varepsilon/p$ cm²·sec (for ε in eV, p in torr), while an attachment rate linearly dependent on the pressure[63], namely $v_a = 2.2 \cdot 10^4 p$ sec⁻¹ (for p in torr) was used. These values are very approximate, but should not have been very important at the pulse lengths under consideration.

The calculation yielded electron-fluid drift velocity and energy maxima for each cycle of the field, and avalanche electron density. The time step in the calculation was made small enough for convergence of the calculation, typically several hundred time steps per cycle. At each pressure,

several quantities were needed to complete the calculation. These included the experimental microwave pulse power (or E-field) waveform, the initial electron (swarm) drift velocity parallel with the applied E-field, the initial electron density and characteristic energy, and the breakdown electron density

Table 4-1 lists values of these parameters used in the calculation, except for the initial drift velocities, at those pressures for which data was taken, as well as the results of the calculation when breakdown density was reached:

Table 4-1

	input parameters				results at breakdown		
Pres.	n_{bkdn}	$\frac{d}{a}$	n_{init}	U_{init}	τ_{bkdn}	E_{rms}	U_{max}
[torr]	[cm^{-3}]		[cm^{-3}]	[eV]	[ns]	[$V \cdot cm^{-1}$]	[eV]
0.100	$8.4 \cdot 10^9$	0.5	$4.5 \cdot 10^{-4}$	2.300	-	no bkdn calculated	
0.250	$5.9 \cdot 10^9$	0.5	$2.6 \cdot 10^{-3}$	0.770	- 38.4	$1.11 \cdot 10^4$	536
0.800	$3.0 \cdot 10^9$	0.3	0.23	0.190	- 23.9	$4.35 \cdot 10^3$	85.7
3.0	$2.2 \cdot 10^9$	0.3	0.30	0.050	- 18.7	$2.81 \cdot 10^3$	29.0
10.0	$9.0 \cdot 10^9$	0.2	3.0	0.017	- 21.6	$3.57 \cdot 10^3$	16.2
39.7	$2.8 \cdot 10^{10}$	0.2	6.0	0.017	- 31.2	$7.30 \cdot 10^3$	10.2
400.	$1.1 \cdot 10^{12}$	0.1	1.2	0.045	- 127	$2.37 \cdot 10^4$	2.90
500.	$1.4 \cdot 10^{12}$	0.1	1.2	0.055	- 170	$2.37 \cdot 10^4$	2.42

The initial drift velocities were taken to be zero at all pressures, and the breakdown densities given in table 4-1 were calculated from equation 2.6, where breakdown was defined as a drop in the transmission coefficient of 1%, from 1.00 to 0.99. This calculation required values for the collision frequency ν and the plasma-column diameter to

waveguide width ratio d/a; ν was taken to be $5.3 \cdot 10^9 p$, and
the d/a ratios were determined empirically from time inte-
grated and streak photographs such as those shown in Fig.
2-2 and Fig. 4-8. Of course, the plasmas did not have dis-
continuous, cylindrical density profiles, and ν is not ener-
gy independent in air; these were approximations. Futher-
more, the d/a ratios could not be completely determined from
time-integrated or streak photographs of the breakdown plas-
mas, since such a determination ignores any part of the den-
sity profile from which light was not emitted.

The initial electron (swarm) characteristic energies
were estimated by averaging the energy loss of 70-eV average
energy Υ-ray-produced electrons (see Appendix B) over the
lifetime determined by diffusion and attachment:

$$U_{init} = \langle U \rangle = \frac{1}{\tau_1} \int_0^{\tau_1} (\text{energy loss}) dt = \frac{1}{\tau_1} \int_0^{\tau_1} U_0 e^{-\nu_w t} dt, \qquad (4.3)$$

where $U_0 = \frac{2}{3} \times 70$ eV, $\tau_1 = [\nu_a + D/\Lambda^2]^{-1}$, and ν_w was from
Fig. 2-6(C). This is a crude estimate of the actual elec-
tron lifetime since it is only valid for values of $\tau_1 \lesssim 1$ μs
(the interval between Υ-ray produced electrons), but it made
little difference in the calculations; assuming $U_{init} =$
70 eV at all pressures only changed the breakdown times and
E-fields given in table 4-1 by $\lesssim 2\%$.

The predicted breakdown fields in Fig. 4-9 exceed the
measured ones by an average of 14%, except at very high and

very low pressures, where the calculation predicted the same field the experiment measured, namely the maximum field in the 12.6 MW pulse. The predicted breakdown times, over the range of 0.25 to 40 torr, are surprisingly longer. In this pressure range, the 1 to 2-ns differences in times could easily be attributed to error in the choice of t=0 for the pulse, as mentioned earlier. This choice was used both in zeroing the time scale in the breakdown time distribution data and in the digitized pulse shape used for the calculations. Above 400 torr, however, the calculation clearly departs from the data; at 0.100 torr no breakdown was predicted at all by the calculations.

The fact that the predicted fields are generally higher than the data can be accounted for by error in the collision frequencies or the initial electron densities used in the calculation. Since n_{init} was estimated and not measured, it is a likely source for error. Fig. 4-9(B) is the same as Fig. 4-9(A), except the theoretical curve was calculated using initial densities 100 times those used to calculate the curve in Fig. 4-9(A). In Fig. 4-9(B), the predicted breakdown fields are only an average of 1.2% higher than the data. Still, no breakdown was predicted at 0.1 torr, and the breakdown times for $p > 400$ torr are too long. At pressures less than a few torr, where $\nu < \omega$, the plasma is not fluid-like, and the failure of the model is not surprising. In fact, because of the small initial electron density, the plasma may not be fluid-like at any pressure at early times

in its development. The failure of the model at high pressures, where the fluid approximation is good, is less clear. The model does not calculate the fields and currents self-consistently, nor does it account for convection or the effects of non-uniform fields. These things, however, would make the times-to-breakdown longer, if they were included in the model, because they all tend to reduce the electron density. The breakdown criterion, as determined from the plasma-post-in-waveguide model, would have to be changed drastically (3 or 4 orders of magnitude in electron density) to make the calculation agree with the experiment. Photo-ionization, which was not in the model, could be responsible for the shorter breakdown times observed, but streak photographs of one dimensional regions of the breakdown plasma could not establish that because a detailed knowledge of the initial electron density was lacking. Successive framing photographs, carried out on a nanosecond time scale, and spectroscopic measurements at ultraviolet wavelengths, would be useful in determining just how important radiation transport is in the development of these breakdown plasmas.

Comparing the results of the calculations and the experiments led to one important result. If the high pressure electron energies were increased by 15% during the calculations, or if the ionization rate ν_i was increased by a factor of 2 to 2.5, the same times-to-breakdown were obtained as in the experiments, within 2%. This is because ν_i is such a steep function of electron energy (see Fig. 2-6) at

high pressures where the maximum oscillation energies are
only 2 or 3 eV. At these pressures and electron energies,
errors resulting from assuming that the breakdown plasma
electron distribution function can be represented by a swarm
are larger than at higher energies.

Non-equilibrium effects could also account for the high
pressure discrepancies; if the plasma electron distribution
function was skewed asymmetrically toward higher energies,
relative to a Maxwell distribution, then the experiments
would yield shorter times-to-breakdown than the calcula-
tions, which assume an equilibrium distribution. However,
at pressures of a few hundred torr and above, collisions
occur on picosecond time scales (times at least two orders
of magnitude shorter than the field oscillation period or
the pulse rise time), and non-equilibrium effects should not
have been important. Further experiments with better char-
acterized pre-ionization sources need to be performed in
order to understand the high pressure results. Such sources
might include pulsed-uv sources, or RF-plasma sources; these
are capable of generating electrons with well known densi-
ties and energies at the same time the microwave pulse is
applied (if the time-decay characteristics of the electrons
generated by such pulsed sources can be measured, then the
effects of different electron energies and densities, at
fixed pressure, can be investigated).

4.2.2   Breakdown of the 2-ns Duration Pulses

In this section, we conclude the experimental results
with breakdown/pulse-transmission data for the shortest
pulses studied.   The incident microwave power pulses, which
were generated by the pulse-compression cavity,[18] had dura-
tions of about 2 ns (FWHM), and peak powers in the range
10-100 MW.   These peak powers corresponded to peak microwave
electric fields of about 3-10 MV/m in the center of the
waveguide.

The incident/transmitted data were taken from two di-
rectional couplers: one 1.4 meters upstream from the [60]Co
sources, and one 1.0 meter downstream from the sources, as
indicated in Fig. 3-3.   Fig. 4-10 shows incident and trans-
mitted envelopes for a typical pulse, with the waveguide
test section evacuated to prevent breakdown.   Although the
pulse envelope at the output of the pulse-compression cavity
was quasi-rectangular in shape, with smooth leading and
trailing edges, after propagating 3.7 meters to the incident
directional coupler, and then an additional 2.4 meters to
the transmitted coupler, the shape was more triangular, with
rippling of the pulse on the leading and trailing edges.
These changes occurred due to waveguide dispersion, the rip-
pling being produced by phase interference of the different
pulse frequency components, which propagated at different
speeds.   This interference modulation of the pulse leading
and trailing edges is to be expected for such short, wide
bandwidth pulses.[20]   Typically, the peak-power amplitude of

2-ns Pulse Experiments; Inc/Trans Pulse
Shape Without any Breakdown

INCIDENT PULSE; VACUUM

NTEGRATED PULSE ENERGY

0.542 J

WG POWER(WATTS)

TIME(NS)

TRANSMITTED PULSE; VACUUM

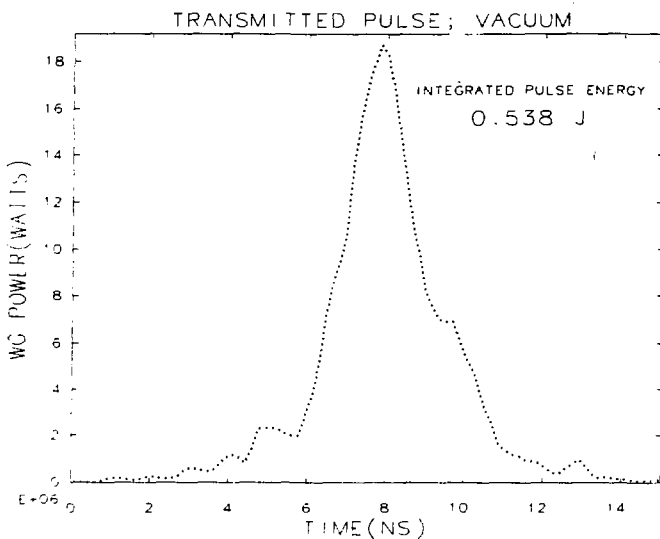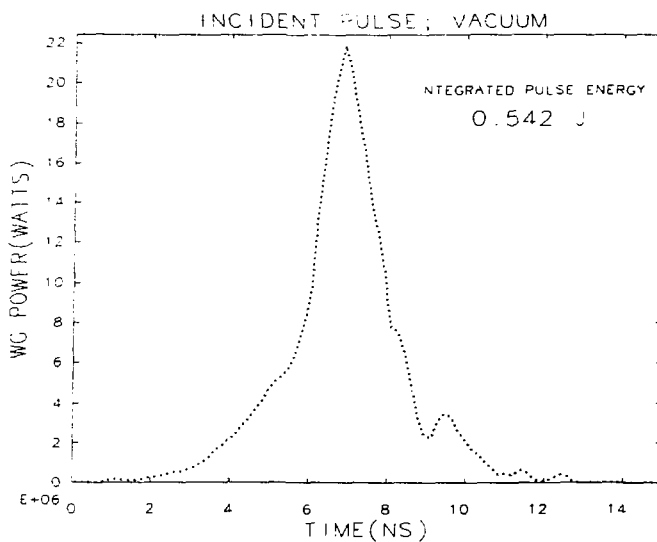INTEGRATED PULSE ENERGY

0.538 J

WG POWER(WATTS)

TIME(NS)

FIG. 4-1○

a transmitted pulse which did not break down was 15-20% low-
er than that of the incident pulse, due to dispersion, but
the integrated pulse energies were nearly equal, as expec-
ted. The integrated energies in Fig. 4-10 are within 1% of
each other, the small difference resulting from digitization
and deconvolution errors, along with a small amount of wave-
guide loss. To reduce the relative error, the pulses indi-
cated in Fig. 4-10 were obtained using the same detector,
attenuators, cables, and oscilloscope on two pulses of iden-
tical shape and amplitude (the pulse-compression cavity
could reproducibly generate identical pulses, to an accuracy
of the width of an oscilloscope trace, or < 1%). Separate
diagnostics were required, of course, when acquiring simul-
taneous incident/transmitted pulse envelope data for single
pulse breakdown measurements. In that case, the absolute
error, as discussed in Appendix A, was ±25%.

Figs. 4-11 and 4-12 show incident pulse envelopes and
transmitted pulse envelopes after breakdown, corresponding
to a single breakdown event in air and in nitrogen, at each
of five pressures covering the range of about 3/4 of a torr
to about 300 torr. Also included are the integrated pulse
energies. Almost no statistical behavior was observed at
these extremely high field strengths; each waveform was
digitized from a single oscilloscope photograph of ten con-
secutive traces. To an accuracy of the width of a single
trace, all ten on each photograph were identical. At each
pressure, attempts were made to ensure that breakdown oc-

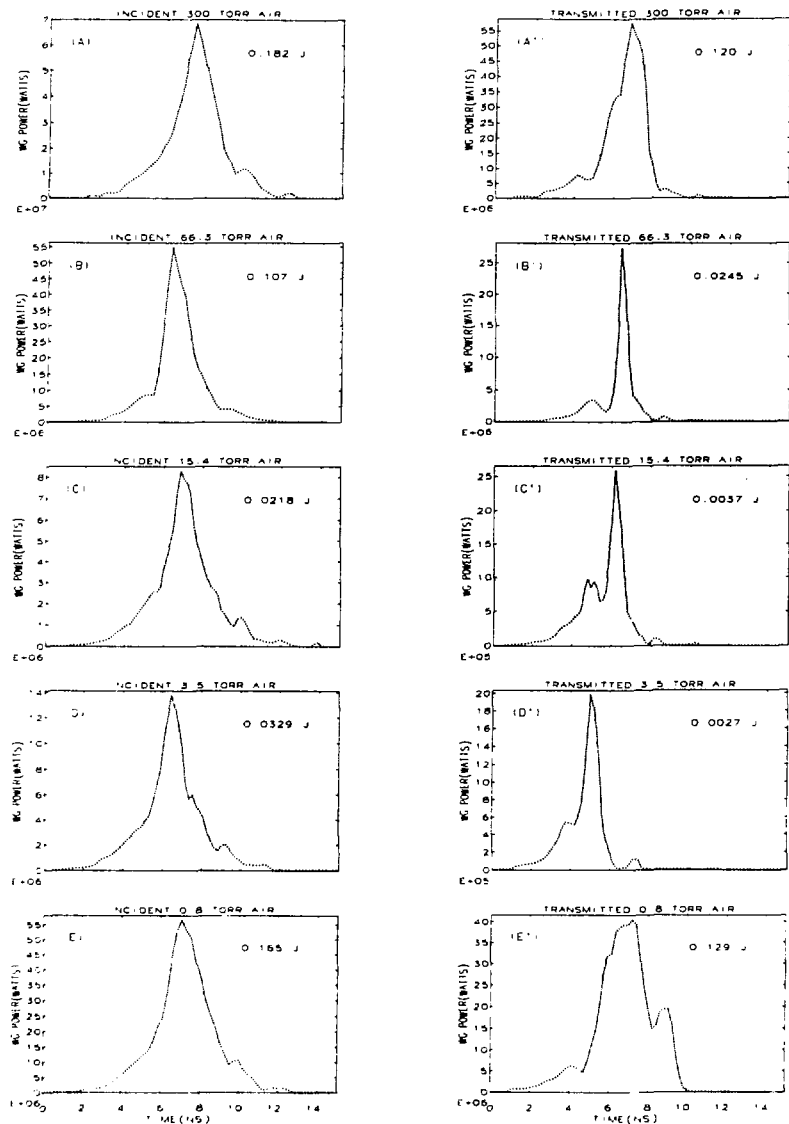## 2-ns Pulse Breakdown in Air;
Measured Inc/Trans Pulse Envelopes

FIG. 4-11

2-ns Pulse Breakdown in Nitrogen; Measured Inc/Trans Pulse Envelopes
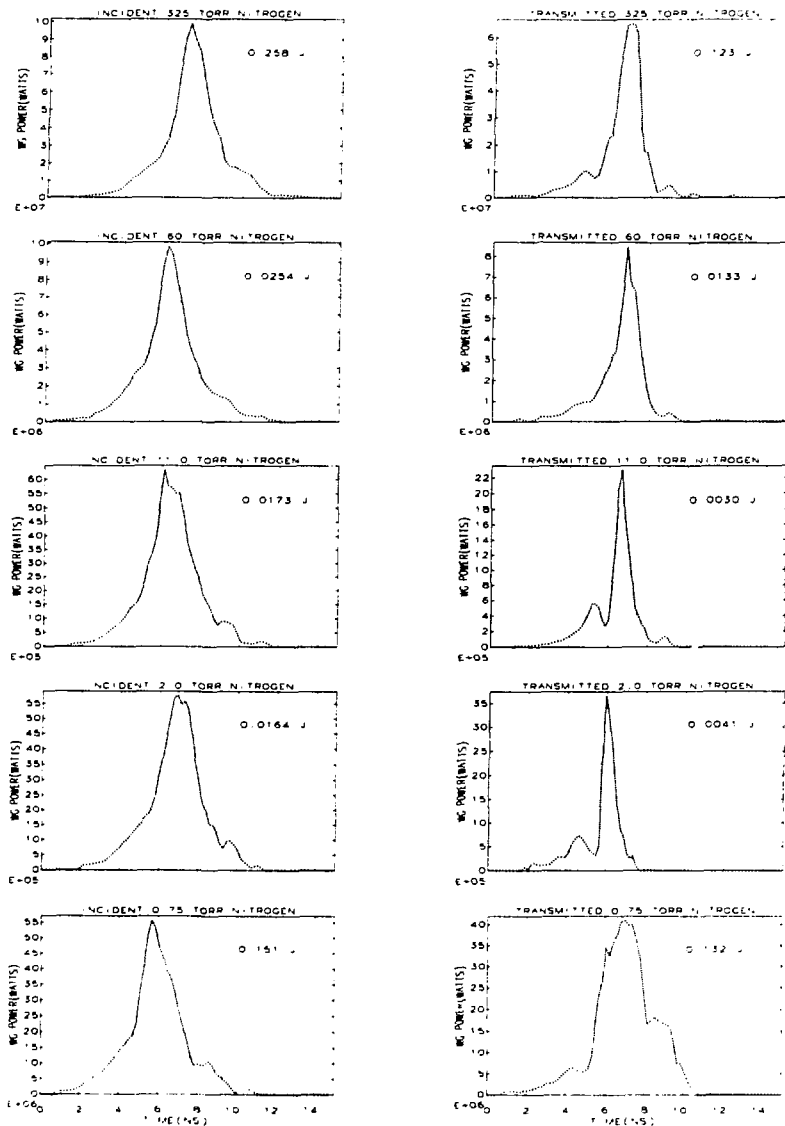
FIG. 4-12

cured as early in the pulse as possible, and the maximum
available peak pulse power was used. However, it was found
that at some pressures, particularly in nitrogen and helium,
raising the peak pulse power too high resulted in breakdown
at the waveguide window rather than at the location of the
radioactive sources. The measurements were made just below
the window breakdown threshold; that is the reason the peak
incident pulse power varies from pressure to pressure and
gas to gas.

At all pressures except the lowest (0.8 torr for air,
0.75 torr for nitrogen), breakdown occurr   on the leading
edge or near the peak of the pulse. At   lowest pressure,
break   n occured on the trailing edge, which was abruptly
clipped off. Only at these low pressures was any statisti-
cal behavior evident. Fig. 4-13 shows an oscilloscope pho-
tograph of diode detector responses to 10 consecutive trans-
mitted pulses at 0.8 torr in air. The trailing edges of the
pulses, during which time breakdown occurred, show a pulse-
to-pulse spread in time of about 0.4 ns. The deconvolved
power pulse in Fig. 4-11(E') corresponds to the earliest
one.

For comparison to these data, 2-dimensional fluid model
calculations, as discussed in Chapter II, were done by Yee
and Mayhall[18] to simulate the experiments for these air
pressures: 300 torr, 3.5 torr, and 0.8 torr. This model,
rather than the swarm model, was used because geometrical
effects, such as dispersion, were important in the transport

Statistical breakdown of 2 ns pulses at 0.8 Torr in air; 10 transmitted pulses

FIG. 4-13

of these short-duration pulses.

Note added in proof: Calculations for the other two ex-
perimental pressures were completed after the data anal-
ysis was done for this thesis. They reproduce peak trans-
mitted powers to within 25% and 41% and transmitted ener-
gies to within 21% and 21% at 15.4 and 66.3 torr, respec-
tively.

The experimental incident pulse envelopes shown in Fig.
4-11(a), 4-11(d), and 4-11(e), were multiplied by $\sin(\omega t)$,
where $\omega/2\pi = 2.856 \cdot 10^9$ Hz, and used as input waveforms for
the calculations. To account approximately for the angular
divergence of the Compton electrons responsible for pre-io-
nization (see Appendix B), and for the diffusion of elec-
trons out of the pre-ionization region, a gaussian spatial
profile was used for the initial electron density. In this
profile, the maximum densities, determined from table 4-1,
were assumed to be in the center of the waveguide, along the
collimation axis of the pre-ionization Υ-rays. The density
was assumed to fall off radially, to half its value at the
waveguide center, in 0.75 cm for pressures above 15 torr,
and in 1.5 cm for pressures above 15 torr. These scale
lengths were again determined from the time-integrated pho-
tographs of breakdown in Fig. 2-2, and were approximate,
since the spatial distributions of the initial densities
were not directly determined experimentally. Prior to the
arrival of the pulse, these initial electrons were assumed
to have zero temperature in the calculations.

    The calculations were started using the experimental

pulse envelopes [multiplied by $\sin(\omega t)$] at the position of
the incident directional coupler. They then calculated the
waveguide fields, electron densities, and electron fluid
energies as the pulse propagated 2.4 m to the transmitted
coupler; the results were plotted at 5-ps intervals. By
comparing line plots of the pulse electric fields, in the
waveguide center along the axis of propagation, at these
5-ps intervals, changes in the fields due to the build-up of
electron density could be observed. When the field ampli-
tude or phase, in any part of the pulse, changed by at least
5% between successive plots, breakdown was considered to
have occurred.

In Figs 4-14, 4-15, and 4-16, the calculated electric
fields, electron densities, and electron-fluid energies are
plotted. A 4.8 m section of waveguide is shown in the
plots; the x-axes are along the guide propagation direc-
tion. Pulse propagation is from left-to-right in the fig-
ures, and the left half (2.4 m) of each figure represents
the section between couplers. The fields, densities, and
energies are plotted at "breakdown" time ($t=t_0$) in the first
column in the figures, and after breakdown in the second
column, for each of the three pressures. The plots in the
second column are for times 4-8 ns later than than those in
the first column, after most of the pulse had propagated
through the source region and breakdown was fully developed;
they depict the absortion, reflection, and transmission of
the pulses. The discontinuity in density and energy on the

2-D Simulations of Air Breakdown in WR284 Waveguide;
Electric Field at Breakdown and After Breakdown

P = 300 torr air
Ez (v/.n) Ez_{max} = 6.83 MV/m
$t=t_0$

P = 300 torr air
Ez (v/m) Ez_{max} = 6.87 MV/m
$t=t_0+4.2ns$

P = 3.5 torr air
Ez (v/m) Ez_{max} = 3.03 MV/m
$t=t_0$

P = 3.5 torr air
Ez (v/m) Ez_{max} = 1.19 MV/m
$t=t_0+7.8ns$

P = 0.80 torr air
Ez (v/m) Ez_{max} = 5.93 MV/m
$t=t_0$

P = 0.80 torr air
Ez (v/m) Ez_{max} = 7.61 MV/m
$t=t_0+4.8ns$

FIG. 4-14

2-D Simulations of Air Breakdown in WR284 Waveguide;
Electron Densities at Breakdown and After Breakdown

Log_{10} (n) (m^{-3})   P = 300 torr air n_{max} = 1.28×10^{19} m^{-3}
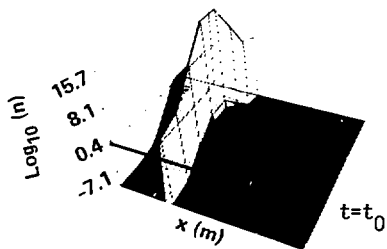
Log_{10} (n) (m^{-3})   P = 300 torr air n_{max} = 2.52×10^{19} m^{-3}

$t=t_0$

$t=t_0+4.2$ns
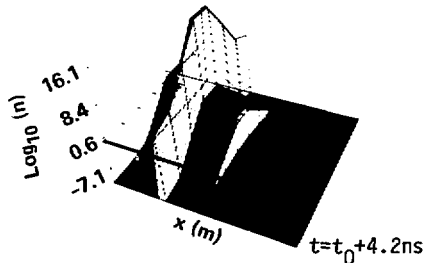
Log_{10} (n) (m^{-3})   P = 3.5 torr air n_{max} = 3.08×10^{18} m^{-3}
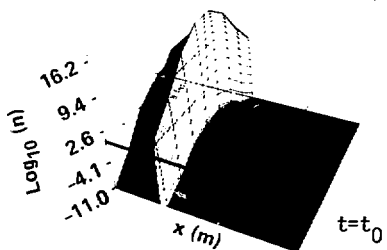
Log_{10} (n) (m^{-3})   P = 3.5 torr air n_{max} = 1.34×10^{19} m^{-3}

$t=t_0$

$t=t_0+7.8$ns
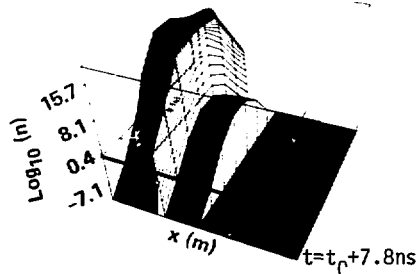
Log_{10} (n) (m^{-3})   P = 0.80 torr air n_{max} = 1.03×10^{17} m^{-3}
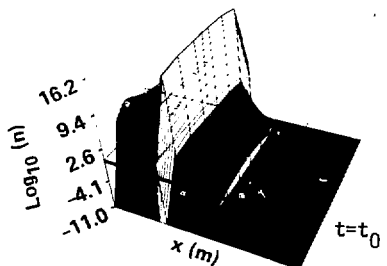
Log_{10} (n) (m^{-3})   P = 0.80 torr air n_{max} = 1.51×10^{19} m^{-3}
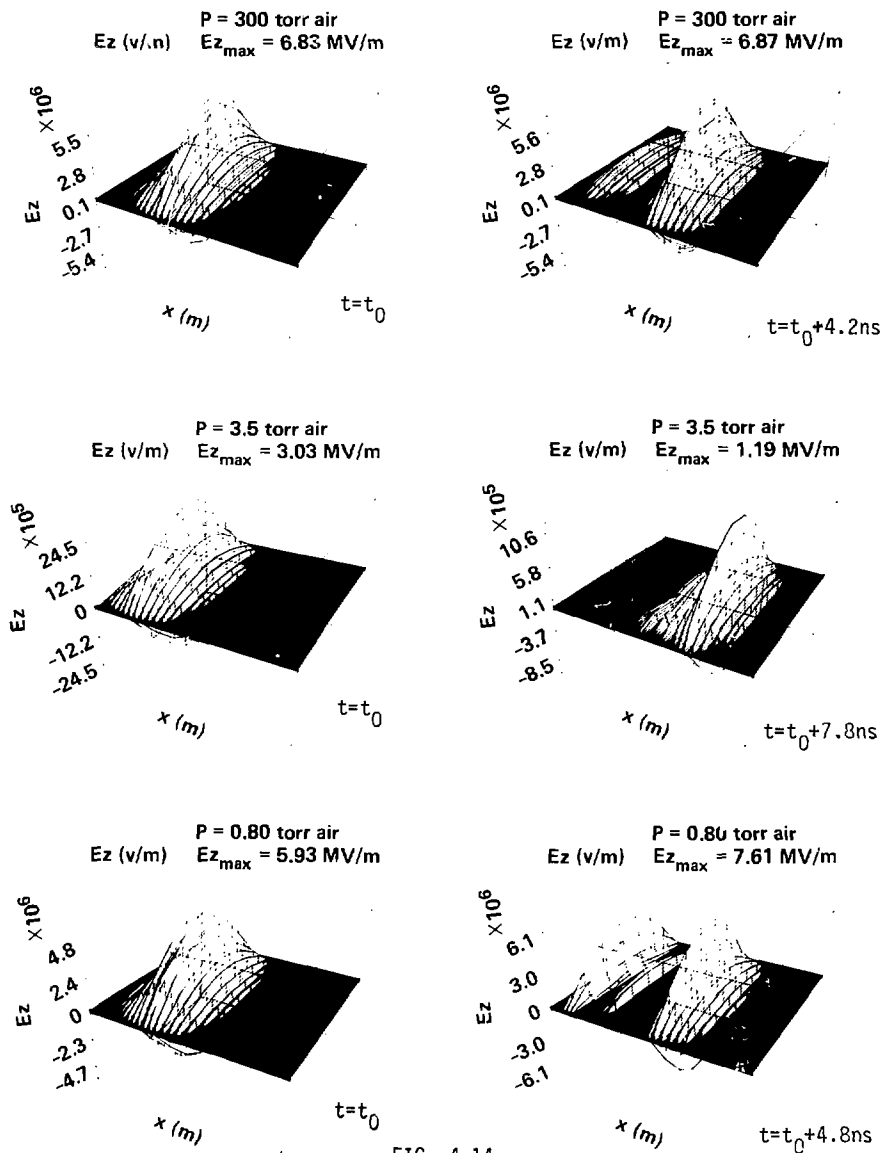
$t=t_0$

$t=t_0+4.8$ns
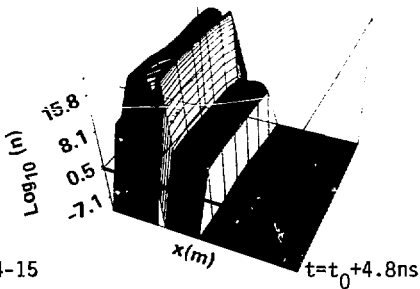
FIG. 4-15

2-D Simulations of Air Breakdown in WR284 Waveguide;
Electron Energies at Breakdown and After Breakdown

P = 300 torr air
U (eV) U_{max} = 0.0116 keV
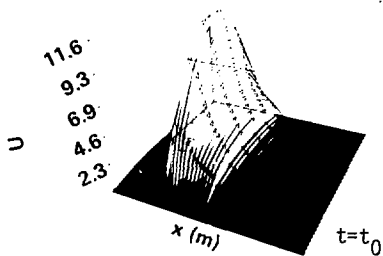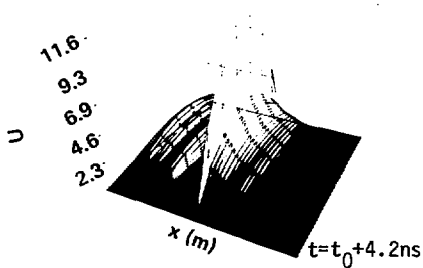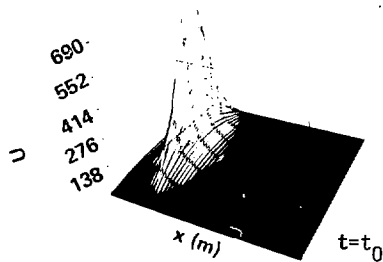
11.6
9.3
6.9
4.6
2.3

U

x (m)   t=t_0

P = 300 torr air
U (eV) U_{max} = 0.0116 keV

11.6
9.3
6.9
4.6
2.3

U

x (m)   t=t_0+4.2ns

P = 3.5 torr air
U (eV) U_{max} = 0.675 keV

690
552
414
276
138

U

x (m)   t=t_0

P = 3.5 torr air
U (eV) U_{max} = 0.0109 keV

10.9
8.7
6.5
4.3
2.1

U

x (m)   t=t_0+7.8ns

P = 0.80 torr air
U (eV) U_{max} = 23.93 keV

$\times 10^3$
23.9
19.1
14.4
9.6
4.8

U

x (m)   t=t_0

P = 0.80 torr air
U (eV) U_{max} = 7.838 keV

$\times 10^3$
7.8
6.3
4.7
3.1
1.6

U

x (m)   t=t_0+4.8ns
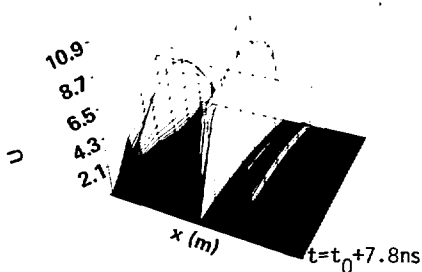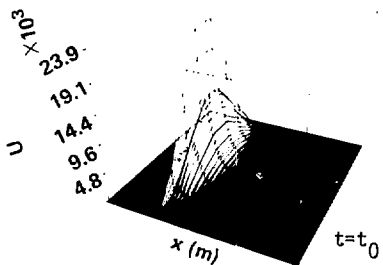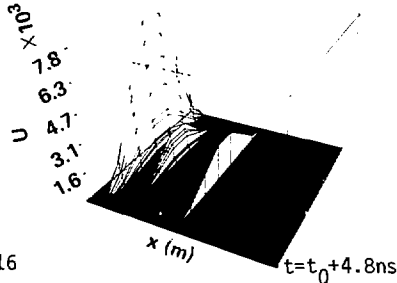
FIG. 4-16

leading edges of the pulses is a calculation artifact;
downstream from this discontinuity (downstream from the
transmitted coupler), the gas pressure and initial electron
density were taken to be 1 atm. and 10^{-5} cm^{-3}, respectively,
in the calculation.

Fig. 4-17 compares the results of the 2-D calculations
with the experimental results. The first column of plots in
the figure shows the experimental incident and transmitted
pulse power envelopes, plotted on the same scale, and the
second column shows the experimental transmitted pulse en-
velope overlaid with the transmitted pulse envelope calcu-
lated using the 2-D theory. As can be seen in the figure,
the experimental and calculated envelopes agree very well at
3.5 torr and 300 torr, nearly two orders of magnitude dif-
ferent in pressure.

The electron energies reached in the experiments were
not well known, though preliminary electron temperature mea-
surements with the same apparatus have been made by Yamagi-
shi, et al.,[21] using spectroscopic techniques and interpre-
ting the data using a coronal model. In those measurements,
small amounts of helium (1-10%) were added to the air, and
nitrogen and helium optical emission line intensities were
compared to infer the electron temperature. The tempera-
tures measured by this technique did not seem to be affected
by variations in helium concentration,[21] however, it is not
known if the presence of helium affected the temperatures
themselves, or the breakdown thresholds. The results of

Transmitted Power Envelope Comparisons; 2-D Simulations and Experimental Results
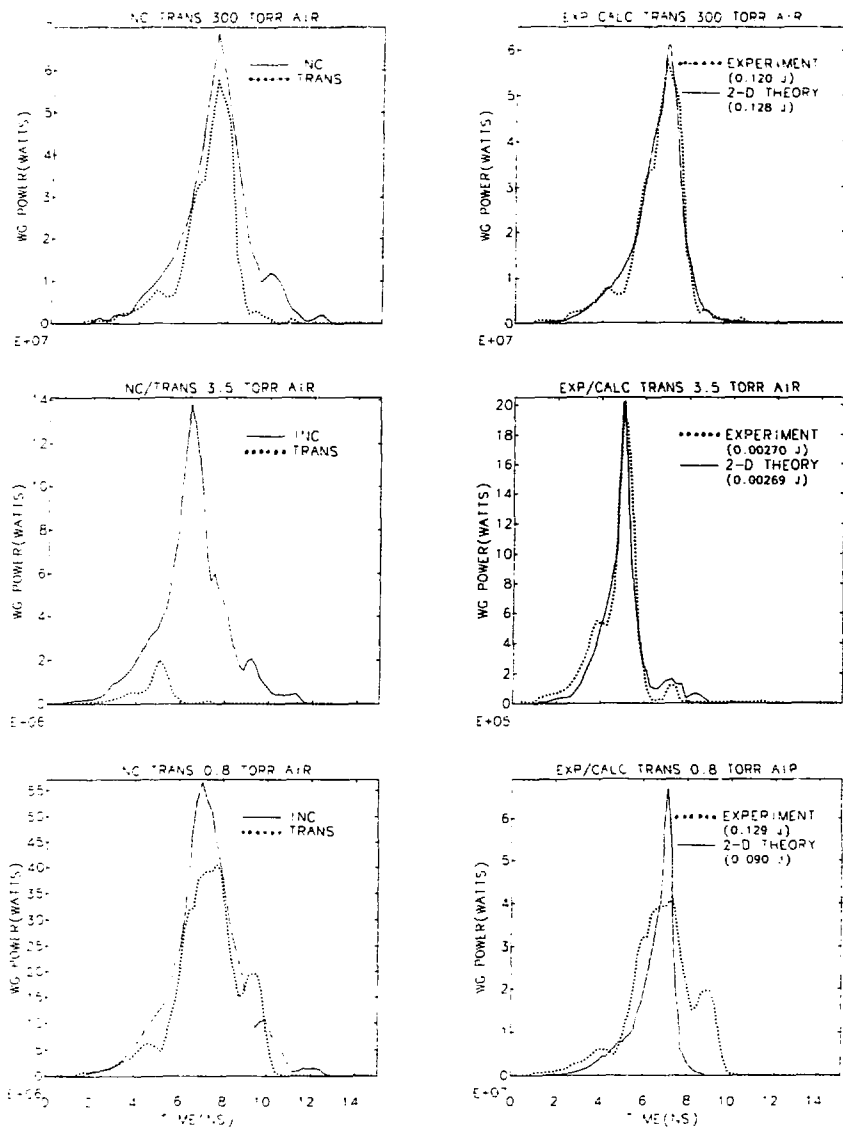
FIG. 4-17

those measure jents, which used an incident microwave pulse
with peak power amplitude of about 20 MW, are shown in Fig.
4-18, which is from Ref. 21.   The temperatures indicated by
the data points were determined from helium and helium-ni-
trogen emission line intensity ratios.   The wavelengths of
the lines (in angstroms) are indicated in parentheses in the
figure.   At 300 torr, the 2-D calculation shows fair agree-
ment with these measurements, but at 3.5 and 0.8 torr the
calculation predicts much higher energies, up to a maximum
of 24 keV at 0.8 torr for a 55 MW incident pulse.   However,
below 10 torr, where the electron energies exceeded tens of
eV, the coronal model is not expected to provide accurate
results.[21]   Also, the experimental measurements may have
averaged the temperature over a larger volume than the peak-
density (temperature) region of the plasma.

At 300 and 3.5 torr, the 2-D calculation doesn't repro-
duce the small peaks, caused by dispersive interference, on
the leading edges of the pulses.   This is because the inci-
dent pulses used in the calculation were only amplitude mod-
ulated at these peaks, at fixed carrier frequency.   There
was no frequency or phase modulation, since the actual fre-
quency content of the experimental pulses was not measured.
If the spectrum and relative phases at the incident direc-
tional coupler had been known, the calculation should have
given more correct results;   this is evident in the disper-
sed bumps on the trailing edges of the pulses, observable in
both the theoretical and the experimental results.   These

Breakdown Plasma Electron Temperature Measurements;
Coronal Model

ELECTRON TEMPERATURE vs. AIR PRESSURE
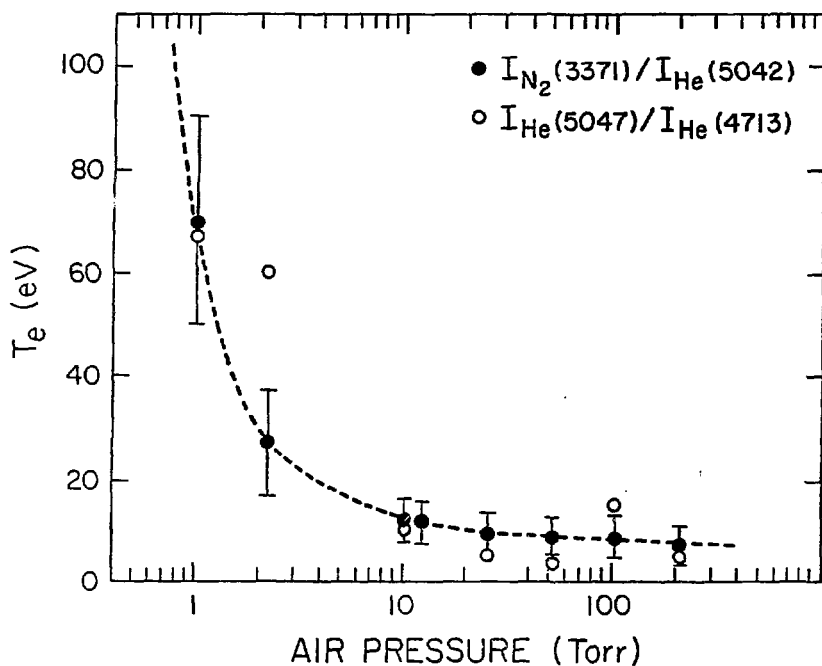
FIG. 4-18

are caused by the introduction of high frequency components when breakdown sharply cuts off the pulse. Since the calculation was 2-dimensional, it did account for frequency dispersion, but accounted for it on the trailing edges of the pulses more accurately. Appendix A, section A.3, contains a discussion of the justification for using a pure frequency, rather than a varying one, in the calculations.

The calculation at 0.8 torr departs significantly from the experimental result, even when an initial density an order of magnitude less than originally estimated is used, as shown in Fig. 4-19. Both calculations predict breakdown about 2-3 ns too early, relative to the experimental result, and yield larger transmitted pulse peak powers than in the incident pulse. Some experiments were performed, in which transmitted pulses resulting from breakdown at the upstream waveguide pressure window were compared with pulses transmitted after breakdown at the source position, the incident pulse amplitude and shape being the same in both cases. The pulses that broke down at the window had to travel further than those that broke down at the source position, and had slightly higher power amplitudes (~ 5%, for detector responses not deconvolved) due to dispersive interference. An enhancement of peak power due to interference effects, as indicated by these measuremtents and the 0.8 torr calculation, is thus possible, and suggests a method of increasing peak power for very wide bandwidth, short pulses. The failure of the model to predict the correct breakdown time at

Transmitted Power Envelope at 0.8 torr;
2-D Theory and Experiment for $n_{init} = 0.0023$ cm^{-3}

EXP/CALC TRANS 0.8 TORR AIR

.... EXPERIMENT
(0.129 J)
———— 2-D THEORY
(0.112 J)

WG POWER(WATTS)

TIME (NS)
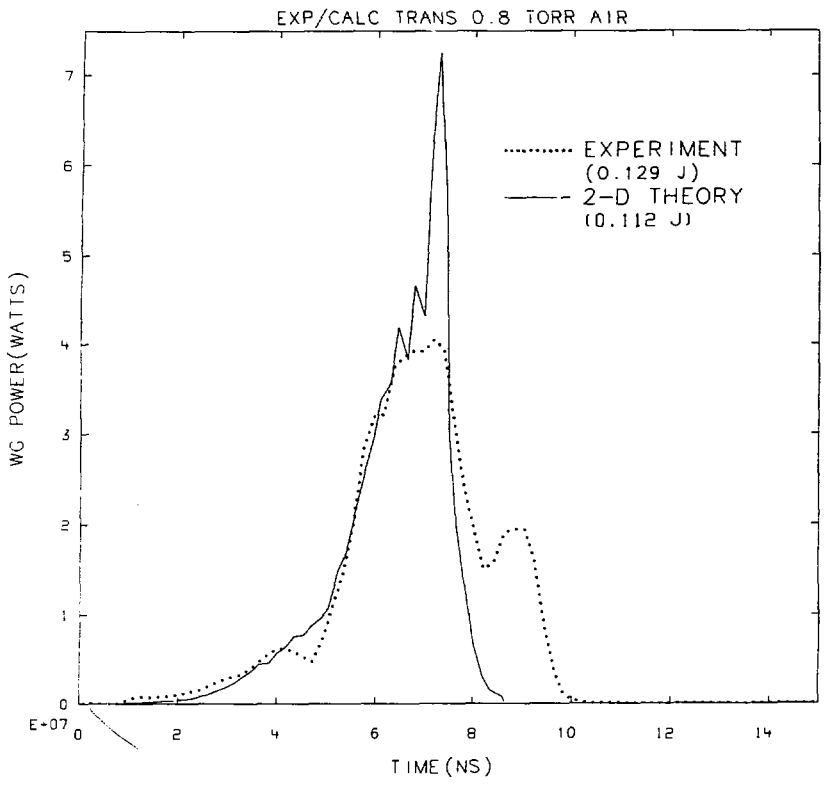
FIG. 4-19

0.8 torr may be expected, since at pressures below 2 or 3 torr, collisions are infrequent with respect to oscillations of the field, and a fluid theory is not appropriate. In addition, the large oscillation amplitudes of the electrons (see section 2.2) can lead to waveguide effects, making the problem three-dimensional. Also, non-equilibrium effects, which are not in the model, can be expected to be important.

4.3   Summary and Discussion

In this chapter, experimental data for air and nitrogen, and theoretical predictions for air, have been presented for microwave pulse breakdown thresholds, the pulse durations ranging from about 2 ns to greater than 1 µs.

The results presented first, for quasi-rectangular pulses of greater than 100-ns duration, established waveguide breakdown measurements as comparable to earlier measurements done in cavity resonators, provided pulse rise time effects were taken into consideration. If the pulse is considered to "start" when the amplitude reaches 90% (or some other fraction) of its maximum, then longer rise time pulses have lower breakdown thresholds, because they contain more energy. This is particularly true when the pulse rise time is a significant fraction ($\geq$ 25%) of its duration. Differences between the experimental results and those obtained from DC breakdown measurements were observed when the two were compared on an E_{eff}/p vs $p\tau$ plot, especially for values of $p\tau < 5\cdot10^{-8}$ torr·sec. At low pressures, the dif-

ferences result from a failure of the effective field con-
cept, as noted by earlier investigators, and for low τ val-
ues, the microwave pulse and DC pulse rise times were not
comparable. Because these rise time and low pressure ef-
fects are so important, swarm and two-dimensional fluid-mod-
els were used to interpret the shorter-pulse data, for which
no comparable previous measurements were available.

For breakdown during the 47-ns rise time of the kly-
stron pulse, leading to triangular-shaped transmitted pulses
of 10-ns to 100-ns duration, it was found that swarm simula-
tions were successful in predicting the experimental results
over a pressure range from about 0.2 torr to perhaps 200-300
torr. These simulations did not treat the microwave fields
and breakdown plasma currents self-consistently, but because
the electron avalanche in gas breakdown occurs so swiftly,
by the time electron densities reach large enough values to
expel the fields, breakdown is imminent, and errors re-
sulting from maintaining the fields in these high density
regions are small. Below 0.2 torr, where the plasmas were
not fluid-like, the swarm calculations failed to predict the
experimental results. They also failed above 400 torr,
probably due either to the model's inability to account for
radiation-transport effects, or because of small errors in
the collision frequencies used. The contribution of uv ra-
diation to ionization in the breakdown plasmas could not be
determined from the photographic streak measurements in
themselves; this problem needs further investigation. On

the other hand, small increases in the low electron-energy
ionization frequency used (< 15%), were seen to bring the
swarm simulations into accurate agreement with the experi-
ments.

Two-dimensional fluid-model simulations were made of
the breakdown experiments done using 2-ns duration pulses.
The 2-D simulations were similar to the swarm simulations,
except that they calculated the fields and plasma currents
self-consistently. This more sophisticated approach was
required in order to predict transmitted-pulse waveforms,
and account for geometrical effects, such as dispersion,
which are important in extremely short pulse propagation.

Agreement well within the experimental error was found
between the experiments and the simulations for pressures of
3 and 300 torr. The best agreement was obtained at 3.5
torr, which is in a pressure region where the breakdown
field is lowest for S-band microwaves. In this case, the
peak pulse power transmitted after breakdown was predicted
to within less than 3% of the experimental result, and the
predicted transmitted pulse energy agreed with the measure-
ment to within less than 1%. This is an important result,
because the pressure range of 2 to 5 torr, where the break-
down field is a minimum, is a critical one for atmospheric
microwave pulse propagation. The model failed to predict
the experimental results below 1 torr, but again, the fluid-
plasma approximation is expected to be poor at low pres-
sures.

Another problem at low pressures is that electron os-
cillation amplitudes are large; at and above 3.5 torr, the
oscillation amplitudes in the 2-ns pulse experiments were
calculated to be less than 2 mm, but in the 0.8 torr mea-
surement, they were calculated to be 10% of the waveguid
height (the dimension parallel with the microwave electric
field). This means that free electrons near the waveguide
walls are accelerated into the walls, and disappear from the
interaction region, resulting in an increase in the break-
down threshold. The fact that the 2-D calculation, which
did not account for waveguide effects, predicted breakdown
too early at 0.8 torr, relative to the experimental result,
suggests that this mechanism may be important; therefore
one cannot make a direct connection between the results of
the low pressure waveguide experiments and the behavior of
pulses traveling in free space.

APPENDIX A.   EXPERIMENTAL DETAILS

A.1   Data Acquisition Systems

In Chapter III, the two different systems used for data aquisition were briefly described. One system collected incident, reflected, and transmitted microwave pulse peak-amplitude and timing data for pulses of greater than 10-ns duration; the other system, used for pulses shorter than 10 ns, photographically recorded the raw pulse waveform envelopes. More detail on these systems is given here.

The experiment for long-pulse measurements is shown in Fig. 3-1 in Chapter III, while the details of the multi-parameter data acquisition system are indicated in Fig. A-1. Four electrical signals were generated during each breakdown event: a negative rectified pulse envelope signal for the incident, reflected, and transmitted microwave pulses, and a photomultiplier signal from the light created by the break-down discharge. The signals were conducted over equal lengths of double-shielded RG-58 coaxial cable to the data acquisition system, where they entered linear fan-out cir-cuits. Here, each was split three ways: one output was used for direct oscilloscope monitoring of the data signal, and the other two were used for amplitude and timing mea-surements.

The right half of Fig. A-1 indicates the signal paths for the amplitude measurements. The signals were linearly

Data Acquisition System - Long-Pulse Measurements
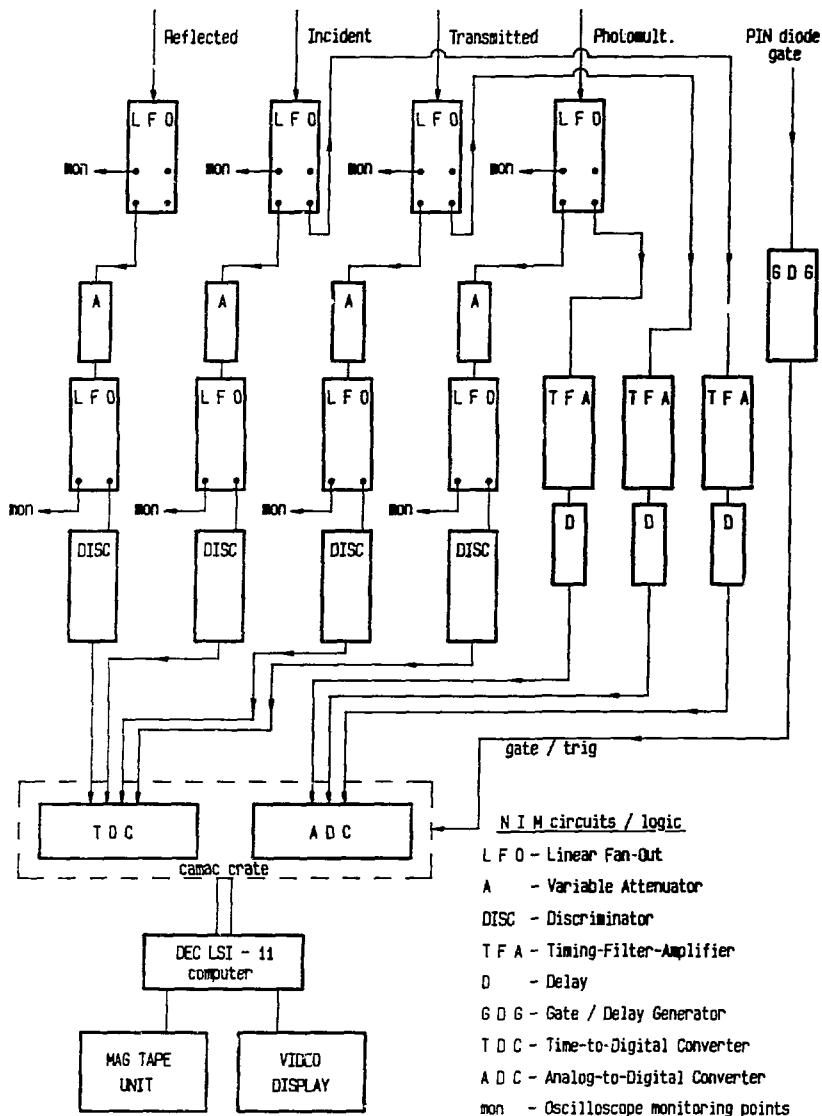
FIG. A-1

amplified and inverted by timing-filter-amplifiers, then run through adjustable delays to an octal, peak-measuring, analog-to-digital converter (ADC), where the peak amplitude of each signal was measured. Amplification was necessary to utilize the full dynamic range of the ADC, and inversion was necessary because of ADC requirements. Delay circuits allowed for synchronization of the data pulses with the acquisition interval of the ADC. Note that the reflected signal amplitude was not measured; it was originally planned to do this, but preliminary measurements indicated that interpretation of the reflected signals would be difficult. Due to inadequate directional coupler directivity and multiple breakdown caused by the subsequent formation of standing waves, the reflected signal amplitudes were not reproducible. However, the initial part of the reflected pulse was reproducible, and thus useful for timing the onset of breakdown.

The left side of the Fig. A-1 schematic shows the timing circuits of the data acquisition system. From the first set of linear fan-outs, the signals passed through variable attenuators into a second set of linear fan-outs, and then through discriminator circuits. The discriminators generated 10-ns duration NIM pulses, coincident with a fixed time on the leading edges of the four pulses. These NIM pulses were then routed to an octal time-to-digital converter (TDC), which measured the time-of-arrival of the NIM/data pulses relative to its own acquisition cycle start time.

The TDC was triggered by the leading edge of a "start" pulse
(the start-pulse voltage was proportional to, and coincident
with, the 8568 klystron current pulse), of course, just be-
fore the NIM/data pulses arrived. The attenuators were used
to keep the four analog data signals regulated to constant
amplitude from one run to another, no matter what the micro-
wave pulse amplitude was, and the second set of linear fan-
outs allowed for visual verification of this with an oscil-
loscope. In this way, the discriminators could be set to
fire when the leading edge of the pulse had reached some
constant fraction of its peak amplitude, no matter what that
amplitude may have been. An arbitrary constant fraction
(~30%) was chosen; constant time values obtained from cali-
brating oscilloscope photographs were added to or subtracted
from the digital data to normalize the timing to the desired
point on the leading edge of the pulses.

For each microwave pulse, the ADC and TDC were trig-
gered and gated, and the signal amplitudes and times were
measured. The computer then read the results, stored them
in memory, and then reset the ADC and TDC to prepare them
for the next event. Every 15 events, the computer wrote the
stored data onto magnetic tape. Though the software that
managed this system was not designed to do analysis in real
time before recording on magnetic tape, the raw data could
be viewed on a video terminal in real time as it was being
acquired.

The recorded data was later analyzed and processed by a
computer program, which allowed one to separate out the ef-
fects of the acquisition electronics, i.e. added delays,
cable effects, and linear and non-linear calibrations.   For
example, data for which photomultiplier signal amplitudes
were below a set threshold were ignored during processing.
This ensured that any breakdowns that occurred in spatial
regions not directly visible to the photomultiplier tube
were ignored.

For microwave pulses of duration less than about 10 ns,
the above system simply was not sufficiently accurate;   the
short-pulse measurements were made directly with oscillo-
scopes, whose traces were photographically recorded.   Fig.
3-3 in Chapter III shows how the 1-GHz bandwidth Tektronix
7104 oscilloscopes were used to simultaneously record the
three microwave envelope signals.   A directional coupler and
rectifying diode connected to the pulse-compression cavity
output provided simultaneous triggering for all three oscil-
loscopes.

A.2   Microwave Diagnostics

The microwave diagnostics consisted of WR284 waveguide
directional couplers, attenuators, fast microwave diode de-
tectors, and cables for delivering the signals to the data
acquisition devices.   These diagnostics are shown in Fig.
A-2.

In experiments in which a microwave pulse has a spatial

Microwave Diagnostics
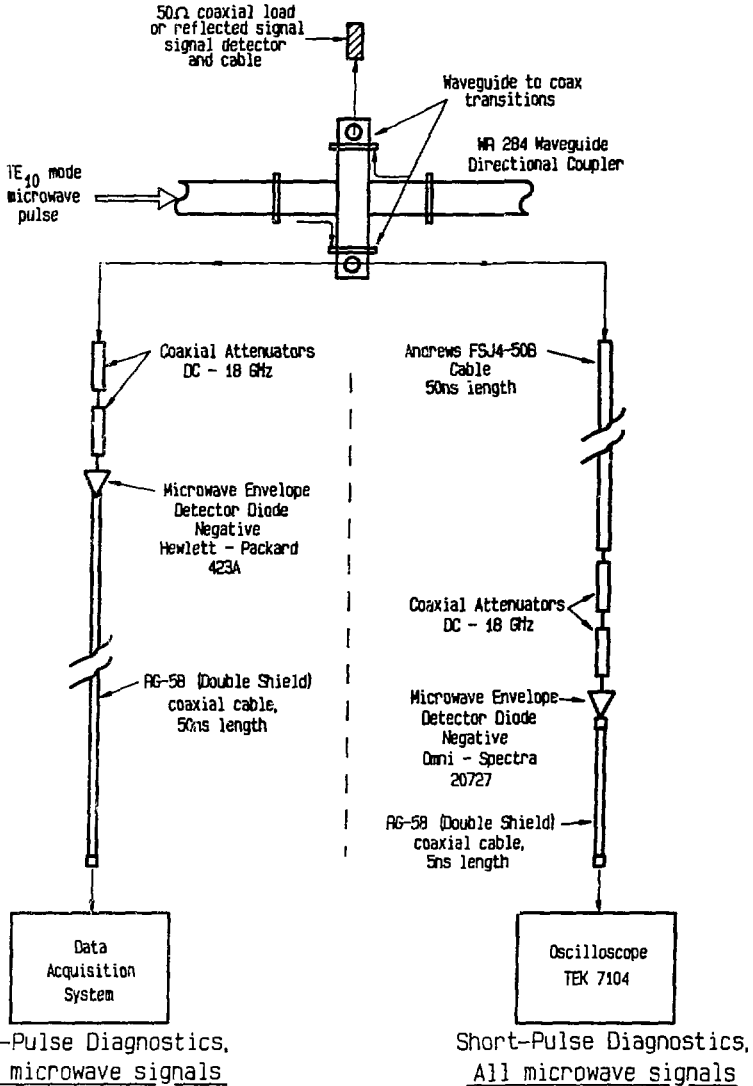
FIG. A-2

extent of the order of, or greater than, the size of the
experiment, it is very important that high directivity di-
rectional couplers be used for accurate measurements.
Otherwise, counter-propagating waves inside the coupler can
interfere with each other and lead to errors. For this rea-
son, a specially designed, 37-dB directivity sidewall direc-
tional coupler was used to measure incident and reflected
power for pulse lengths of 10 ns or longer. All transmitted
pulses, and incident and reflected pulses of duration less
than 10 ns, were measured with wide-bandwidth, low-directi-
vity (~15 dB) couplers. Since 3-GHz pulses of less than
10-ns duration carry a considerable number of significant
frequency components besides the carrier, broadband couplers
were necessary to accurately monitor the pulse shapes. All
couplers were calibrated over a 1.3 GHz wide band about
2.856 GHz to an accuracy of 0.01 dB.

From figure A-2, one sees that the detector/cable deli-
very system used depended on the pulse length being mea-
sured. For the longer pulses, calibrated attenuators were
connected first to the directional couplers. These attenu-
ated the microwave signals to within the dynamic range of
the diode detectors. Next, calibrated Hewlett-Packard 423A
point-contact diode detectors with 1-2 ns intrinsic rise
time[22] converted the microwave signal to a negatively recti-
fied envelope signal, which was delivered to the data acqui-
sition system via a 50-ns length of RG-58 coaxial cable.
The cable attenuation was, of course, accounted for.

Because RG-58 is very lossy at high frequencies or
short pulse lengths, the system was slightly altered for
measuring short pulses. In that case 50-ns lengths of
Andrews FSJ4-50B cable carried the microwave signal from the
coupler to the attenuators. Calibrated Omni-Spectra 20727
back diode detectors with 0.6-ns rise time (see Sec. A.3)
converted the microwave signal to a negative-rectified en-
velope, and a short, 5-ns length of RG-58 conducted the en-
velope signal to the 7104 oscilloscopes. Again, loss due to
the cables (at 2.856-GHz frequency) was accounted for.

The pulse envelopes recorded by the data acquisition
systems, along with knowledge of signal attenuation and the
detector and coupler calibrations, determined the TE_{10} wave-
guide mode electric fields as a function of time for the
incident and transmitted microwave pulses.

A.3 Short-Pulse Signal Processing

In this section, the signal processing methods briefly
described at the end of chapter III will be discussed in
more detail.

As indicated in Sec. A.2 of this appendix, the inci-
dent and transmitted microwave pulse waveform measuring sys-
tem consisted of Omni-Spectra 20727 back diodes driving
Tektronix 7A29 amplifiers in a Tektronix 7104 oscilloscope.
Because this system lacked the bandwidth to accurately re-
solve the details of the short pulses (< 5 ns) generated by
the pulse-compression cavity and transmitted through the

breakdown regions, signal processing was required.

From linear response theory,[23] we know that if $r(t)$ is the time response of a linear system to a driving function $f(t)$, and if $R(s)$ and $F(s)$ are their respective complex Fourier transforms (one-sided Laplace transforms for causal functions), then

$$R(s) = F(s)H(s), \qquad (A.1)$$

where $H(s)$ is the system transfer function. Further, the response $h(t)$ of the system to a unit impulse $\delta(t)$ is just the inverse transform of $H(s)$. Thus a knowledge of $r(t)$ and the impulse response $h(t)$ allows one to deconvolve the original driving function $f(t)$ by inversely transforming $F(s)$, where

$$F(s) = R(s)/H(s). \qquad (A.2)$$

Additionally, $h(t)$ can be determined from the unit step response $u(t)$ of the system, since

$$u(t) = \int_0^t h(\tau)d\tau. \qquad (A.3)$$

The diode/cable/oscilloscope system used for the short-pulse experiments was a linear system, provided the diodes were operated in their square-law regions. To be able to reconstruct actual pulse shapes from measured ones using the techniques described above, it was necessary to measure the step response of that system. This was done with the cir-

cuit indicated in Fig. A-3. A continuous signal of 2.856-
GHz frequency was applied to the local oscillator input of
an Anaren model 75127 diode mixer with 1.8 GHz IF bandwidth.
A Hewlett-Packard 215A pulser driving a step-recovery diode
was used to generate a 100±10-ps 10-90% rise time voltage
pulse (measured with a Tektronix 7S11 sampling unit and S-6
sampling head in a 7104 oscilloscope), which was applied to
the IF port of the mixer. The RF output of the mixer was
thus gated "on" by the IF pulse, and was applied to the
diode/cable/oscilloscope system to measure its step re-
sponse. The rise time τ_{meas}, of the oscilloscope waveform
was assumed to be related in quadrature to the rise time τ_{IF}
of the pulse applied to the mixer IF port, the mixer rise
time τ_{mix}, the Omni-Spectra diode rise time τ_{diode}, and the
oscilloscope amplifier rise time τ_{scope}, as

$$\tau^2_{meas} = \tau^2_{IF} + \tau^2_{mix} + \tau^2_{diode} + \tau^2_{scope}. \qquad (A.4)$$

The oscilloscope rise time was 350 ps, as reported by the
manufacturer. This was verified by a separate sampling mea-
surement. The IF pulse rise time was 100 ps, as indicated
above. The mixer rise time could not be measured by this
circuit, but was below an upper limit set by the IF band-
width of 1.8 GHz.

These measurements yielded 10-90% rise time values of
590 ps ±10% for the Omni-Spectra 20727 diodes, and 660 ps
±10% for the diode/cable/oscilloscope combination, for peak
diode voltage outputs varying between 50 and 140 millivolts.

Detector Diode / Cable / Oscilloscope
Step-Response Measurement Circuit
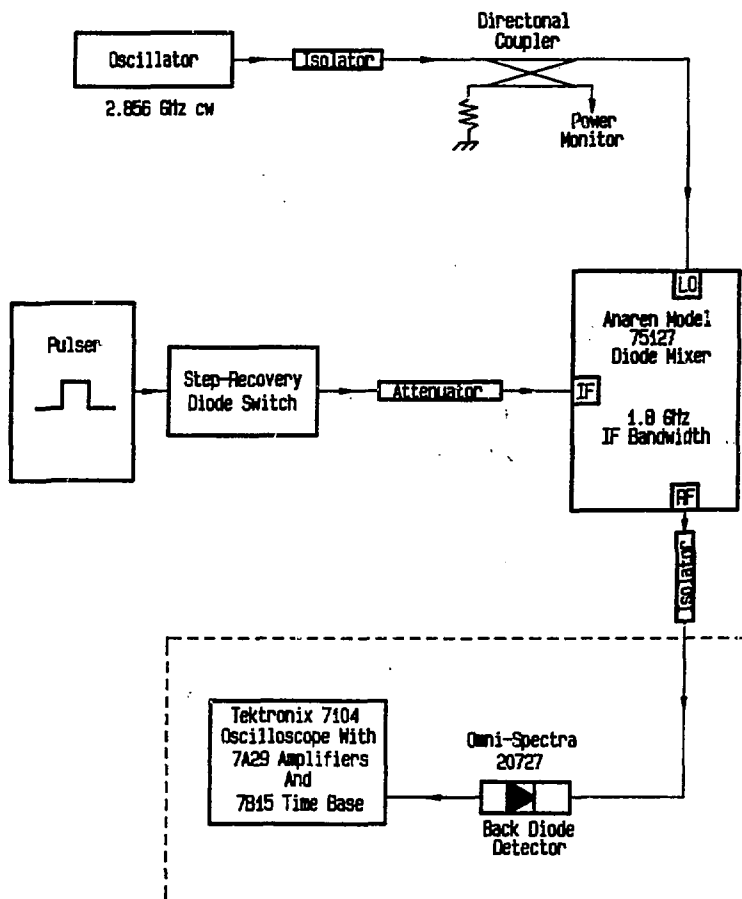
FIG. A-3

The error values include the resolution and accuracy limitations of the oscilloscope waveforms, as well as mixer rise time uncertainty as indicated above. Within the error, the diode rise time is consistent with the 650-ps rise time result reported by Ballard and Earley[22] for a similar Omni-Spectra diode. The manufacturer reports that at higher output voltage levels than those examined by Ballard and Earley, the video resistance of these diodes is lower, making the rise time shorter. It is therefore expected that the rise times measured by Ballard and Earley would be slightly longer.

Once the step response of the diagnostic system was known, it was possible to process the data using the linear response theory techniques discussed above. For this purpose, a collection of signal-processing computer programs developed at the Lawrence Livermore National Laboratory[24] was used. Fig. A-4 shows a flowchart of the processing that was done. Incident and transmitted microwave pulse envelope waveforms, recorded photographically from the oscilloscopes, were first digitized. Next, the step response of the diagnostics was integrated to yield a unit impulse response, which was also digitized. Computerized processing of the data was then initiated. Fast Fourier transforms (FFTs) were performed on the data and impulse response to yield their frequency spectra. The data spectrum was then divided by the impulse spectrum to yield the deconvolved data spectrum, as in equation A.2. Inverse transformation of this

Flowchart For Signal Processing Of Short - Pulse Data

```
┌────────────────────────┐  ┌────────────────────────┐
│ Incident / Transmitted │  │  Impulse Response Of   │
│    Data Waveforms,     │  │ Diagnostics, Digitized │
│       Digitized        │  │                        │
│    Time vs Voltage     │  │    Time vs Voltage     │
└────────────────────────┘  └────────────────────────┘
```

| Fast Fourier Transform | Fast Fourier Transform |

| Data Spectrum ÷ Impulse Spectrum |

| Waveguide Pulse Envelope / Time vs Power |

| Inverse Fast Fourier Transform |

| Waveguide Pulse Envelope / Time vs rms E-Field |

| Adjust For Detector Calibration and Attenuation / Time vs Power |

| Integrated Energy, Running Sum / Time vs Energy |

| Convert To Electric Field / Time vs E-Field |

| Multiply By Sin (wt) |

| Fast Fourier Transform |

| Restore E-Field Envelope |

| Directional Coupler Frequency Response |

| Adjust For Finite Coupler Bandwidth |

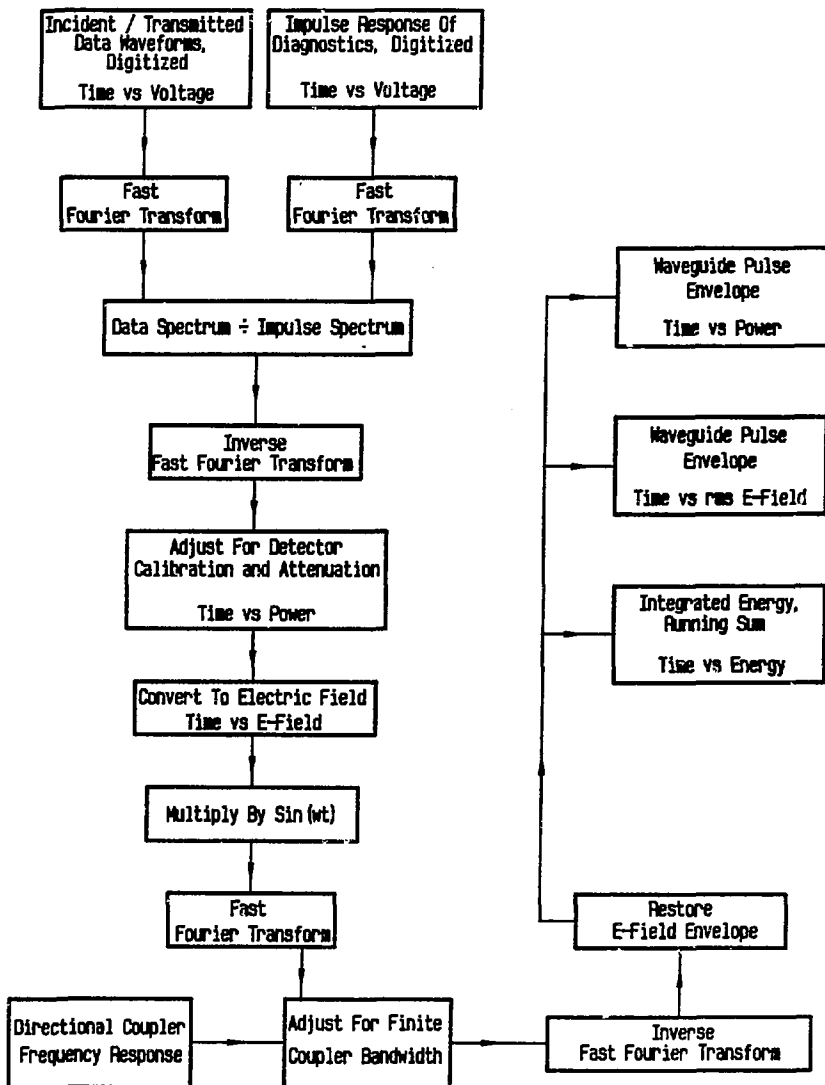| Inverse Fast Fourier Transform |

FIG. A-4

spectrum yielded deconvolved data. Next, microwave power vs
time was calculated using the detector calibration and ac-
counting for any attenuation used. This power envelope was
then converted to an electric-field envelope, which in turn
was converted to a microwave signal by multiplying by
$\sin(\omega t)$, where $\omega/2\pi$ was the 2.856-GHz carrier frequency.
The spectrum of this signal was then obtained by performing
another FFT, after which all its spectral components were
adjusted according to the frequency response of the direc-
tional coupler used. An inverse FFT then yielded the micro-
wave electric-field signal within the waveguide. From this
result, the electric field vs time, average power vs time,
and integrated pulse energy vs time were generated.

The only questionable step in this process was the con-
version of the E-field pulse envelope to a microwave signal
by multiplication by $\sin(\omega t)$. This is because the phase and
frequency modulation of the carrier, due to pulse-compres-
sion and waveguide dispersion, were not known. However, the
frequency modulation of the carrier in the output of a pulse
compression cavity has been measured.[25] In Ref. 25, a
300 MHz modulation of the carrier upward from the resonant
frequency of an X-band cavity was observed. The effects of
modulation of this type were studied parametrically, using
the signal processing program discussed earlier, by multi-
plying the E-field envelope of a typical transmitted pulse
by $\sin(\omega(t) \cdot t)$, where $\omega(t)$ was chirped over a 300-MHz band
centered at the carrier frequency. The final resulting pow-

er envelopes varied by no more than 4% in time or amplitude
from the results obtained using an unchirped carrier. The
same results would have obtained over a wider band as the
directional couplers used had a flat frequency response
(less than 0.5 dB) over a 600-MHz band centered at 2.856
GHz.

To further examine the effects of dispersion, waveguide
propagation was also modeled using the signal processing
program. Fig. A-4A shows a typical pulse power envelope
(after deconvolution and accounting for directional coupler
effects) measured at a directional coupler located about two
feet from the output of the pulse-compression cavity. The
amplitude scale in this figure is arbitrary; all the pulses
had this same shape. This pulse shape is quite different
from the incident pulse shapes measured in the breakdown
experiments (see, for example, the left column of plots in
Fig. 4-11), because the incident pulses were measured 3.7
meters further down the waveguide and had undergone disper-
sion. The effects of dispersion on this cavity pulse can be
simulated as follows: first, one computes an electric field
envelope (in the center of the waveguide) from the pulse in
Fig. A-4A. Next, one multiplies this envelope by
$\sin[\omega(t) \cdot t]$, and calculates the resulting pulse's frequency
spectrum. Dispersion at a distance z from the cavity output
coupler is accounted for by multiplying each component of
this spectrum by $e^{i\beta z}$, and the dispersed pulse is computed
by inversely transforming the multiplied spectrum. To pre-

Measured Pulse Power Envelope at the Output
of the Pulse-Compression Cavity

CAVITY OUTPUT PULSE POWER ENVELOPE
AFTER DECONVOLUTION AND REMOVAL OF
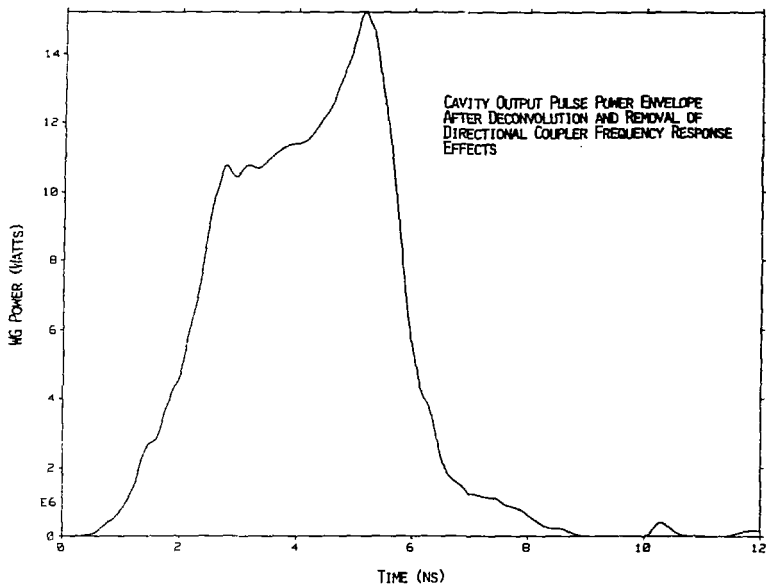DIRECTIONAL COUPLER FREQUENCY RESPONSE
EFFECTS

FIG. A-4A

dict the waveform at z = 3.7 m, the location of the direc-
tional coupler used to measure the incident pulses in the
breakdown experiments, these steps were followed using a
waveguide phase factor $\beta = c^{-1}(\omega^2 - \omega_c^2)^{1/2}$, and a chirped car-
rier wave [$\omega(t)$ was initially 2.856 GHz, and increased line-
arly with time by 150 MHz during the pulse]; the power enve-
lope and E-field waveforms shown in Fig. A-4B(A) and A-4B(B)
resulted.

A better approximation to the measured incident coupler
waveform was obtained with chirping than without. For com-
parison, the measured incident pulse envelope from the 0.8
torr air breakdown experiment is shown in Fig. A-4B(C). The
pulse envelopes in Figs. A-4B(A) and A-4B(C), though not
identical, have similar rippling on their leading and trail-
ing edges, indicating that dispersion and cavity frequency
modulation were the primary mechanisms responsible for phase
modulation. Further, we can compare the calculated E-field
waveform corresponding to Fig. A-4B(A) with the one used for
input to the two-dimensional simulation of breakdown at 0.8
torr discussed in Chapter IV. These are shown in Figs.
A-4B(B) and A-4B(D), respectively. The E-field waveform in
Fig. A-4B(D) was obtained from the envelope in Fig. A-4B(C)
by multiplying by sin(ωt), where ω was 2.856 GHz. Though
there is phase modulation in the waveform shown in Fig.
A-4B(B), the variation from cycle-to-cycle is small; this
pulse could be considered to have an effective frequency of
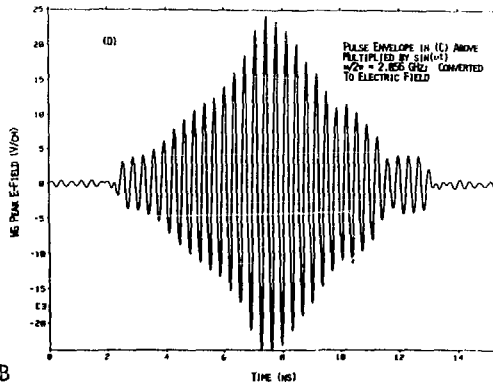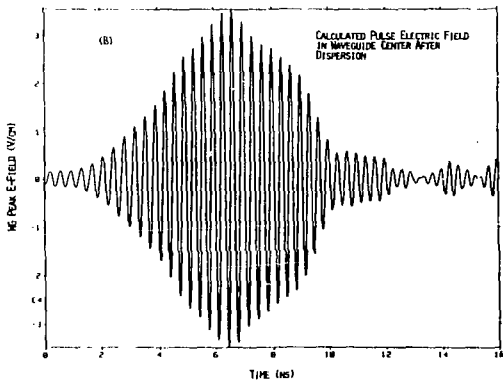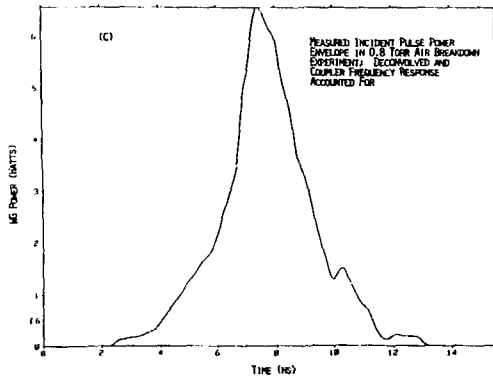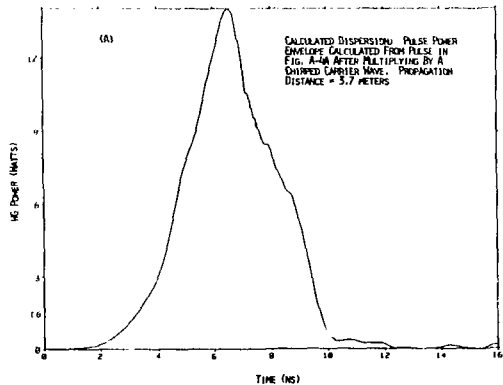$\omega = (\omega_0 + 150 \text{ MHz})/2$, where $\omega_0 = 2.856$ GHz. There are no large

FIG. A-4B
Calculated pulse dispersion and measured incident pulse envelope from the 0.8 torr air breakdown experiment. (D) obtained from (C) after conversion to field and mult. by sin(ωt).

cycle-to-cycle phase shifts during the pulse except on the trailing edge, and multiplying the measured incident pulse envelopes by a pure frequency carrier [Fig. A-4B(D)] to yield an E-field envelope for use as input to the two-dimensional simulations is expected to be a reasonable approximation.

A.4   Optical Diagnostics

A circular aperture and sapphire window placed in one of the narrow walls along the radius of an H-plane waveguide bend provided visual access to the microwave breakdown plasma.   The plasma image was directed, with the aid of two half-silvered mirrors, into a 35-mm camera, a photomultiplier tube, and a streak camera.   The layout is depicted schematically in Fig. A-5.   In addition, a second photomultiplier tube viewed the upstream pressure window (not shown; see Fig. 3-3 in Chapter III) through a quartz optical window and allowed for monitoring of window breakdown.

The 35-mm camera, shown with a 105-mm lens and 2X tele-extender, captured time-integrated, two-dimensional frames of the plasma on ASA 400 film, push-processed to ASA 1200. An RCA 8855 photomultiplier tube, with 2-ns rise time, was used for the long-pulse measurements, and a faster Hamamatsu R1635 tube, with 800-ps rise time, was used for looking at short-pulse breakdown.   Both types of tubes had S-20 photocathodes, and, for the radiation to which they were sensitive, yielded spatially averaged breakdown light-intensity

Optical Diagnostics

side view

Load

waveguide H-plane bend

microwave source

breakdown plasma

to cameras, photomult. tube

top view

microwave source

^{60}Co sources

breakdown plasma

optical viewport

half silvered mirrors

A

B

80-200mm zoom lens

100μm slit

35mm camera

Hamamatsu C979 Streak Camera

shutter

photomultiplier tube

to data acquisition system

105mm lens

2X tele-extender

35mm camera

to microwave system trigger

FIG. A-5

Diagnostics view of breakdown plasma

Waveguide wall

plasma

optical viewport aperture
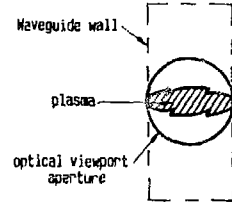
Plasma/slit image - axial

slit image
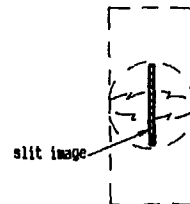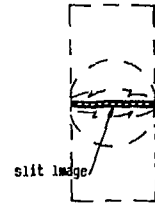
slit image

Plasma/slit image - radial

vs time measurements. In the streak camera, the plasma im-
age was focused by an 80-200-mm zoom lens onto a 100-μm
slit. The image of this slit was then swept, as the plasma
developed, across the film (ASA 400) in a second 35-mm cam-
era body attached to the back of the streak camera. Typi-
cally, 5-ns or 10-ns sweep exposures were made. By ad-
justing the orientation of mirror A, or by rotating both
mirror A and the streak camera about the axis indicated by
the dotted line in Fig. A-5, any one-dimensional part of the
two-dimensional view of the plasma seen through the optical
viewport could be imaged on the streak camera slit. In gen-
eral, two types of exposures were made: those in which the
central axis of the plasma column were imaged on the slit,
and those in which the radial portion of the center of the
plasma column were imaged. Since the streak camera had a
light gain of 3000, it was also used as a single-shot fram-
ing camera, particularly when the breakdown discharges pro-
duced low levels of light.

A.5 Pulse-Compression Resonator

Microwave pulse-compression involves the accumulation
of microwave energy in a resonant structure, and the subse-
quent rapid release of this energy to some type of external
load. Ideally, the accumulation time is much longer than
the extraction time, and pulse length is traded for power
gain.

The theoretical details of microwave energy storage in

cavities were worked out in the late 1930s by Hansen,[26] Condon,[27] and Borgnis,[28] while more recently these ideas have been discussed with regard to the pulse-compression problem.[29,30]

Schwarzkopf built the first experimental pulse-compression resonator in 1962,[31] and since that time others have contributed further developments to the technique, using both room-temperature and superconducting resonators.[25,32,33] This technique has been used in gas breakdown studies similar to this work,[6,7,34] and suggested as a means for increasing the accelerating fields in rf particle accelerators.[35] A similar technique, using a different scheme to extract the stored energy, is in use at the Stanford Linear Accelerator Center.[36]

The basic principles of microwave pulse-compression can be understood by referring to Fig. A-6. Here, a TE_{104} resonant mode is excited in a rectangular, asymmetric T-shaped cavity. In the unswitched state (A), the stored energy is very weakly coupled to the output arm of the structure, and the cavity behaves like any high-Q resonator. At some point in time after the input microwave signal has been turned on, the stored energy in the resonator attains its maximum value.[37] When this has occurred, an inductive, conducting post, located one-quarter of a guide wavelength (or an odd multiple of quarter wavelengths) from the cavity wall opposite the input aperture, is "turned on", and the waveguide is short-circuited at that point. Now the counter-propa-
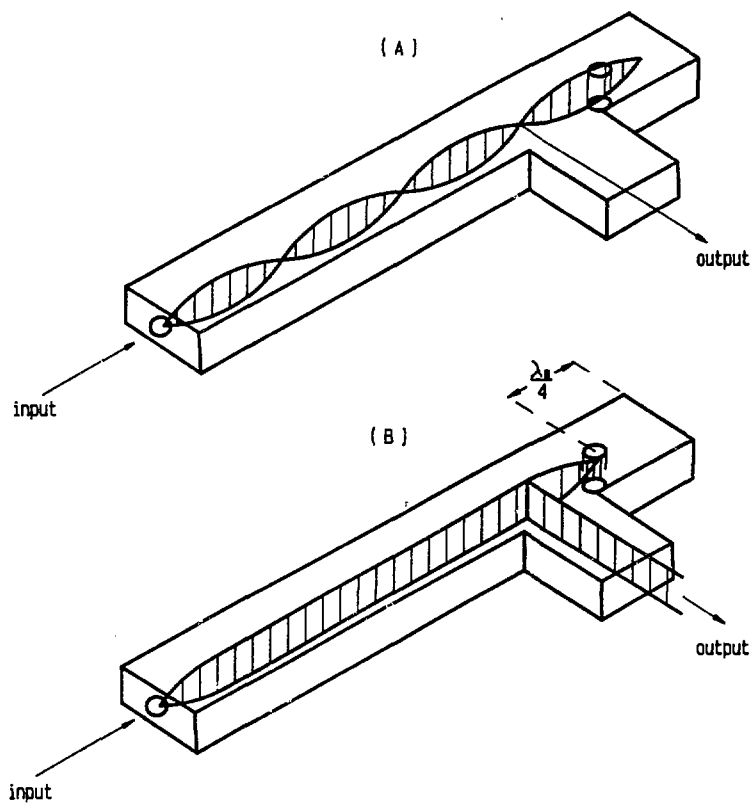
Pulse-Compression Cavities – Basic Concept

FIG. A-6

gating waves at the output arm no longer phase cancel; rather, they add in phase and are strongly coupled to the output arm, as in (B). This is the switched state. The microwave energy in the cavity is then dumped to an external load in a time equal to twice the length of the cavity divided by the group velocity of the guided waves in the structure.

Several different types of switches have been constructed for pulse-compression resonators. These include spontaneously-breaking gas switches, triggered self-breaking gas switches, and electron beams. In spontaneously-breaking switches, the microwave fields inside the cavity break down a gas localized $\lambda_g/4$ from the cavity end wall. The breakdown discharge then represents a large impedance discontinuity or an effective short-circuit. Triggered self-breaking switches are similar, in that the microwave fields still break down the gas, but the time this occurs is controlled by a trigger, for example, by the uv-ionization produced by a triggered spark-gap. Electron beams, on the other hand, can be fired directly through the (thin) cavity walls in a direction parallel with the microwave E-fields. The resulting conducting channel then provides a current path across the waveguide, again shorting it out. These techniques, and similar ones, have all been reported in the literature.[31,38-40]

Fig. A-7 is a schematic of the pulse-compression resonator built for the short-pulse breakdown measurements. It is a room-temperature resonator, constructed of OFHC copper

Pulse-Compression Resonator

FIG. A-7
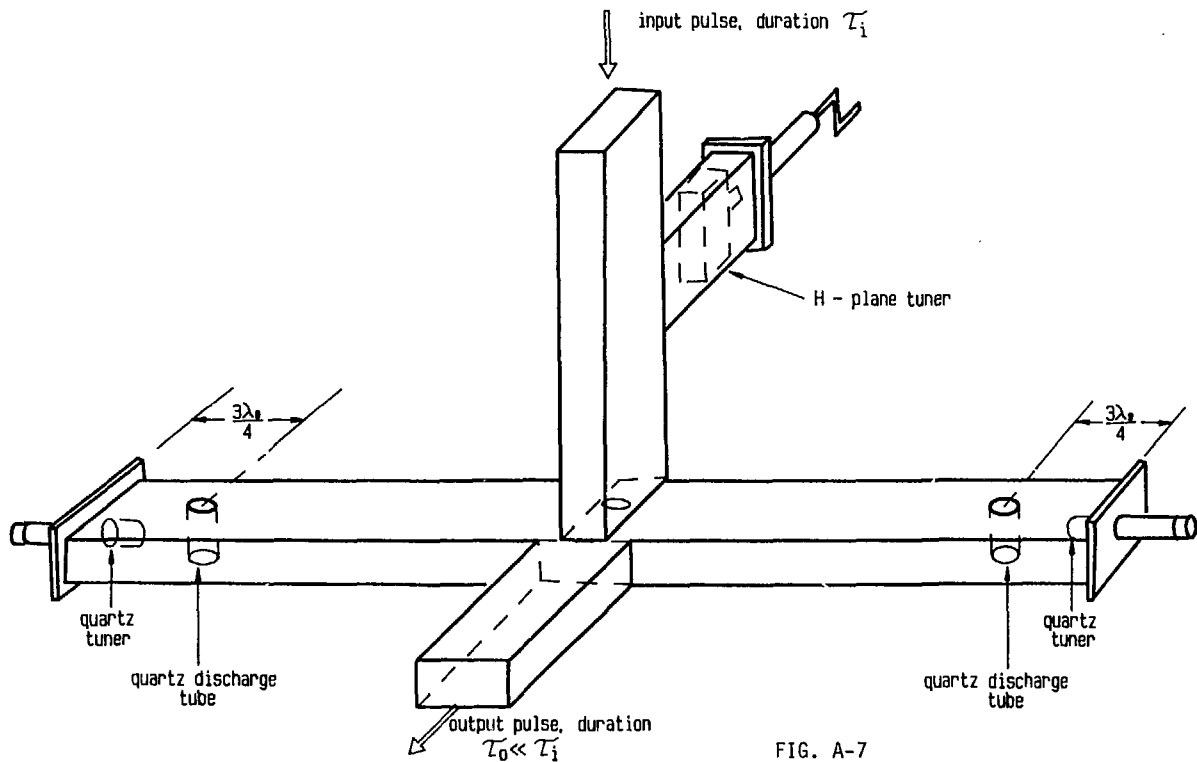
WR284 waveguide, of such an electrical length as to produce
a 5-ns output pulse. The magic-T configuration of the in-
put/output waveguides, along with the symmetrical arrange-
ment of the cavity on either side of them, greatly increases
the unswitched isolation of the device[16]; i.e. leakage of
microwave energy into the output waveguide during filling,
but prior to switching, is suppressed relative to the unsym-
metric T. For a given output pulse length and field
strength in the cavity, this configuration also doubles the
output power, relative to the asymmetric T, because it is
twice as long.

The H-plane tuner on the input arm was designed to al-
low one to vary the coupling of the source to the cavity,
while dielectric tuners at either end inside the cavity al-
lowed for isolation and resonant frequency adjustment.
Pressure-isolated quartz discharge tubes were located in the
center of the cavity broadwall, $3\lambda_g/4$ from the cavity ends.
One tube served as a switch; the other was a dummy, main-
taining the symmetry required for prepulse suppression.

The switch that was used is shown in more detail in
Fig. A-8. This switch was a spark-gap-triggered, self-
breaking switch. The gap, of a point to planar-screen type,
was positioned nearly flush with the cavity inside wall. A
grounded-screen anode was necessary to prevent microwave
energy from coupling out of the cavity and into the spark-
gap high voltage pulser.

Operated with 1 or 2 torr of Ne in the switch tube,

Pulse-Compression Cavity Switch and Switch Trigger Assembly

H V connector

U V spark plug assembly

Dielectric support / seal

O-ring seal

Cathode

0.050" spark gap

Grounded screen anode

WR284 waveguide

Quartz discharge tube

O-ring

Vacuum pumpout / Gas feed assembly

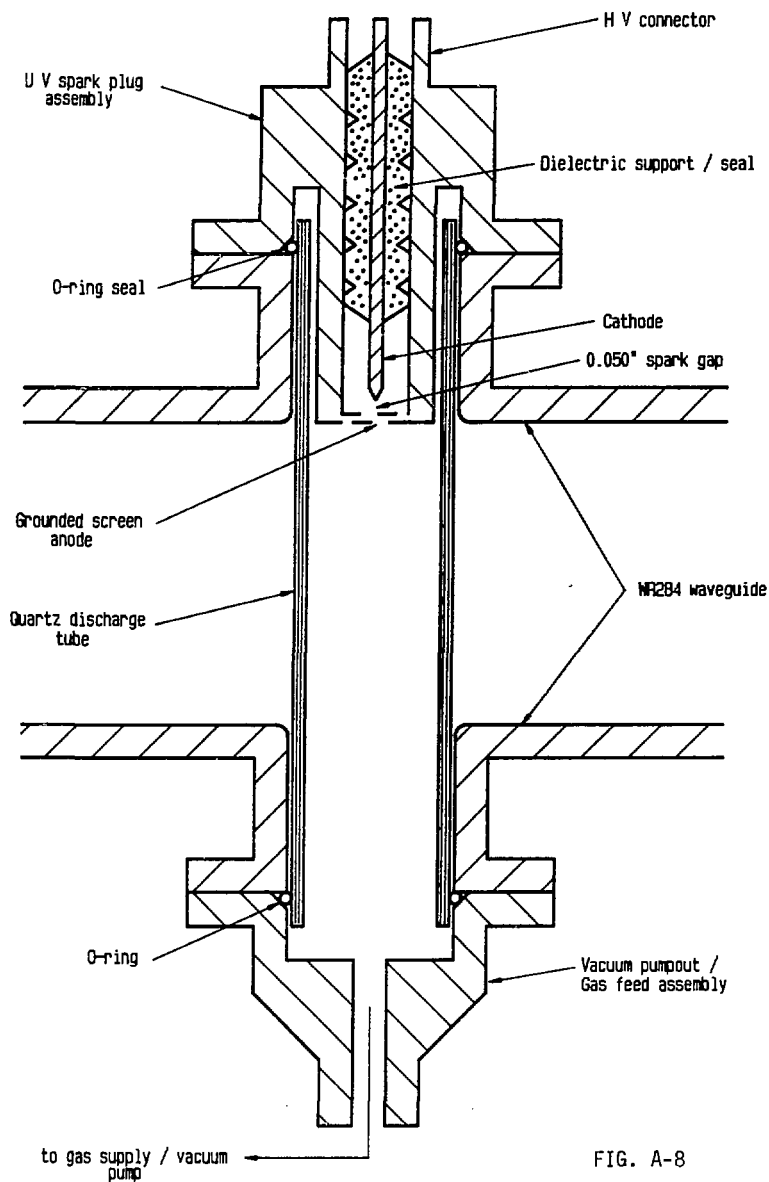to gas supply / vacuum pump

FIG. A-8

this pulse-compression cavity worked very well, at least up to the point where the dielectric strength of the neon was greatly exceeded by the cavity microwave fields. The resonator had an intrinsic Q of about 13000, and a drive-pulse to output leakage-pulse isolation of 70-80 dB. For drive-pulse amplitudes of 10 kW to about 1 MW, the peak power gain was flat and exceeded a factor of 60 for critical coupling of the cavity to the source. More details on the efficiency and electrical operation of the symmetric pulse-compression cavity can be found in Ref. 18.

The 3-ns rise time, 2.5-ns FWHM pulse shape generated by this resonator [see, for example, Fig. 3-4(D)] was the same for drive amplitudes of 10 kW to about 1 MW, and its jitter was determined entirely by the spark-gap trigger pulser jitter (~2 ns). Above 1-MW drive-pulse amplitude, the switch broke down spontaneously and limited stable operation. This limitation precluded generating pulses with peak amplitudes greater than about 100 MW.

A.6 Vacuum/Gas Handling System

The schematic shown in Fig. A-9 shows how the test gases were transferred in and out of the waveguide test section. Manifolds connected to the wave guide narrow walls forced the gases in or out through eight 1" X 1/4" slots. The slots were oriented parallel to the wave guide electric fields and produced negligible reflection and/or perturbation of the propagating mode (the VSWR of the slotted sec-

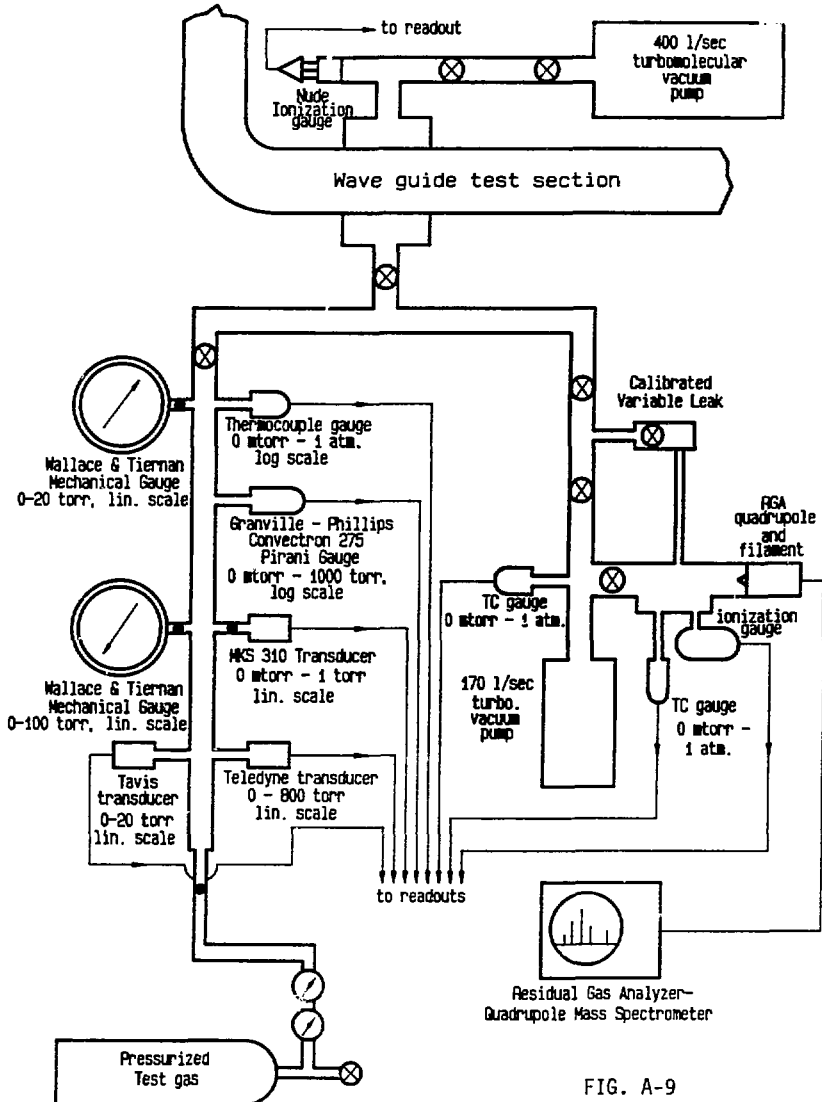# Vacuum / Gas Handling System

Fig. A-9

tion was less than 1.03:1).

The gas handling system connected to the test section
was divided into three major assemblies: primary vacuum
pumping, pressure measurement, and gas composition analysis.
The primary vacuum pump was a 400 liter/sec turbomolecular
pump connected, and in close proximity, to the test section.
Pressure measurement and test-gas introduction were conduct-
ed via a secondary manifold as shown in the figure. Final-
ly, the secondary manifold also connected the test section
to another turbomolecular pump and a residual gas analyzer.

Since the vacuum system contained many indium and Viton
O-ring seals, it was not a bakeable ultra-high vacuum sys-
tem. Even so, the entire system was heated to about 100°C
to reduce water vapor outgassing, and those parts of it not
adjacent to rubber and indium seals were heated to 150°C..
After baking and pumping for 2 or 3 days, the waveguide test
section reached its minimum base pressure of approximately
$1 \cdot 10^{-6}$ torr. All experimental runs were conducted after
pumping to this base pressure and then backfilling with gas.
At $1 \cdot 10^{-6}$ torr, the test section volume had an outgassing
rate of 15 µtorr/min. This outgassing rate implied maximum
contamination levels of 1 part in 10^5, during a typical ex-
perimental run, at the lowest test gas pressures studied.
As measured by the residual gas analyzer, the contaminants
consisted primarily of H_2O and small amounts of CO and H_2,
typical of unbaked leak-tight vacuum systems containing hot
filaments. With the filaments off during the runs, water

vapor was the principle contaminant. Though contamination
at this level may have affected the accuracy of the helium
breakdown measurements,[1] earlier studies of breakdown in
air and nitrogen containing water vapor[2] suggest that there
are no significant effects on the air and nitrogen measure-
ments.

The pressure transducers and mechanical gauges used
were all calibrated with a mercury-column manometer over the
range of 1 to 760 torr, and a mercury McLeod gauge over the
range of 0.001 to 1.000 torr. The calibration equipment was
isolated from the vacuum system with a dry ice/acetone trap
to prevent mercury contamination. The test gases used were
obtained from the Matheson company:

Air   - Matheson Ultra-Zero Air, dry, certified total
           hydrocarbons as CH_4 < 0.1 ppm

Nitrogen - Matheson Ultra-High Purity Nitrogen; the sum
           of O_2, Ar, CO_2, THC as CH_4, and H_2O < 10 ppm,
           99.999%

Helium   - Matheson Ultra-High Purity Helium; the sum of
           N_2, Ar, CO_2, THC as CH_4, and H_2O < 10 ppm,
           99.999%

A.7   Errors

The two primary physical quantities measured in the experiments done for this thesis were gas pressure and instantaneous time-average microwave pulse power in WR284 waveguide. From standard impedance relationships for the TE_{10} mode, the peak microwave electric fields in the waveguide were determined.

All pressure instrument calibrations, and experimental pressure measurements, were carried out at $30\pm1^\circ C$. The measured pressures for which breakdown data were recorded were estimated to have the following accuracies in the given pressure ranges:

```
1% uncertainty for    1 torr ≥ p  and  p ≥ 100 torr;
3% uncertainty for  100 torr > p >  10 torr;
10% uncertainty for  10 torr ≥ p ≥   2 torr;
25% uncertainty for   2 torr > p >   1 torr.
```

These values were determined from instrument manufacturer specifications (verified by manometer and McCloud gauge calibrations), and the minimum resolution of the U-tube manometer used for the calibrations of the pressure transucers.

For pulses of greater than 10-ns duration, the microwave pulse power was determined from diode-detector voltage responses to pulses sampled from the waveguide test section and attenuated to within the dynamic range of the detectors. The maximum voltage response, related to the maximum pulse power by a cw calibration of detector response vs microwave power at 2.856 GHz, was recorded digitally by the data acquisition system (DAS) described in Sec. A.1 of this appen-

dix. The directional couplers and attenuators used were
calibrated to 0.01-dB precision and 0.04-dB accuracy with a
2.856-GHz cw signal source and a Hewlett-Packard 438A power
meter with 8481A and 8484A power sensors. The integral non-
linearity of the DAS was less than 2%, and the detector
calibrations were reproducible to within an accuracy of
0.1-dB in microwave power for a given voltage response (the
reproduciblity, not the accuracy, of the detector calibra-
tions determined the estimated error). In a particular ex-
periment, then, the maximum pulse power error (i.e. the er-
rors in attenuation, detector calibration, and computerized
measurement of detector responses added in quadrature), was
less than 0.2 dB. It was found, however, that in indepen-
dent experiments, line-voltage fluctuations and uncharacter-
ized mismatches between coaxial and waveguide components
introduced further errors, making maximum power measurements
reproducible only to within an accuracy of 0.5 dB. Thus in
the E-field vs pressure and E-field vs time data in Secs.
4.1 and 4.2.2, the electric fields (proportional to the
square root of the measured pulse power) were estimated to
be accurate to within 0.25 dB, or 6%.

The times-to-breakdown in Sec. 4.1 were measured by a
LeCroy 2228A octal TDC, which recorded the difference in
time between two discriminator pulses: one coincident with
the microwave incident pulse leading edge and one coincident
with the leading edge of a photomultiplier or microwave re-
flected power pulse, as described in Sec. A-1. The EG&G

T105/N discriminators used had less than 2-ns output pulse jitter and slewing when triggered on the leading edge of the 47-ns rise time input pulses (regulated to constant amplitude ±5%). The TDC had 1-ns resolution, and an integral non-linearity of 2-ns. The times-to-breakdown reported in Sec. 4.1 were thus accurate to less than 1%. The times reported in Sec. 4.2.1 for 10-ns to 100-ns duration pulses, were only accurate to ±4 ns. The additional error in the shorter pulse measurements resulted from the pulse zero-time definition; for these pulses the zero-time was not the time the pulse reached 10 or 90% of its maximum amplitude, because there was no discriminator-pulse signal. Instead, the TDC acquisition cycle start time was related to the 0% time of the microwave pulse, and because of the small slope of this pulse at early times, the 0% time was determined only within ±2 ns.

The power envelope wave forms in Sec. 4.2.2 were deconvolved from waveforms measured with Tektronix 7104 oscilloscopes and 7A29 amplifiers and 7B15 time bases (see Sec. 3.2). The amplifier accuracy reported by the manufacturer was ±2%; the time base sweep accuracy was the same. These accuracies were verified by calibrations with a precision voltage source (0.1 mV absolute accuracy) and a pure oscillating signal (frequency deviation < 5 parts in 10^{10}) from a Hewlett-Packard 5360A computing counter. Without deconvolution, however, the peak pulse powers measured could have been in error by more than 50% because of oscilloscope and

detector bandwidth limitations. The measured impulse re-
sponse of the oscilloscope/detector system (see Sec. A.3)
yielded 590 ps ±10% for the system rise time. 10% error in
the rise time resulted in ±8-mV error in the deconvolved
detector responses at the peaks of the power envelopes, for
detector responses in the range 50 to 140 mV. From the de-
tector calibrations, ±8-mV error corresponded to ±0.8-dB
error in the power, for detector responses less than 130 mV,
resulting in an overall error (including errors in attenua-
tion and detector calibration), for the peak pulse powers in
Sec. 4-1, of ±25%. The results for the incident pulse at 66
torr in air (see Fig. 4-11), where the detector output vol-
tage was larger than 130 mV, and the detector was saturated,
are estimated to be accurate to within ±30%.

To some extent deconvolution errors will "cancel", at
least as far as comparisons with the 2-D simulations are
concerned. That is, an error in the incident pulse re-
sulting from an incorrect impulse response will also result
in an error **in the same direction** in the transmitted pulse
calculated by the 2-D simulation. The absolute experimental
error, however, is as given above.

APPENDIX B. THE INITIAL ELECTRON DENSITY

Accurate predictions of breakdown dynamics require a
knowledge of the initial "seed" electron density, prior to
the application of the microwave field. In this appendix,
estimates of the initial electron density generated by two
160-mCi ^{60}Co γ-ray sources placed just outside the breakdown
test section will be made.

The geometry of the radioactive source placement rela-
tive to the waveguide test section is indicated in Fig. B-1
(see also Fig. 2-1 in chapter II). Ionization inside the
waveguide is produced directly by the interaction of the
γ-rays (1.25-Mev average energy) with the gas and by the
interaction of forward and back-scattered Compton electrons
with the gas, the Comptons being produced inside the copper
waveguide walls by the γ-rays.

In general, this problem is very complex; its solution
requires a detailed knowledge of the photon transport into
the waveguide, of all possible energy loss processes, both
elastic and inelastic, that can occur to the photons and
electrons within the gas, and of the chemistry and reaction
kinetics of the gas under irradiation. Most of the cross
sections and kinetics for the relevant reactions have been
measured, and following all these processes, e.g. in a nu-
merical simulation, is possible in principle. However,
since the breakdown condition, as indicated by equation

PREIONIZATION GEOMETRY

Only one source is shown; the other is symmetrically
located. Angular divergence of the γ-rays from the
collimators has been ignored.

FIG. B-1

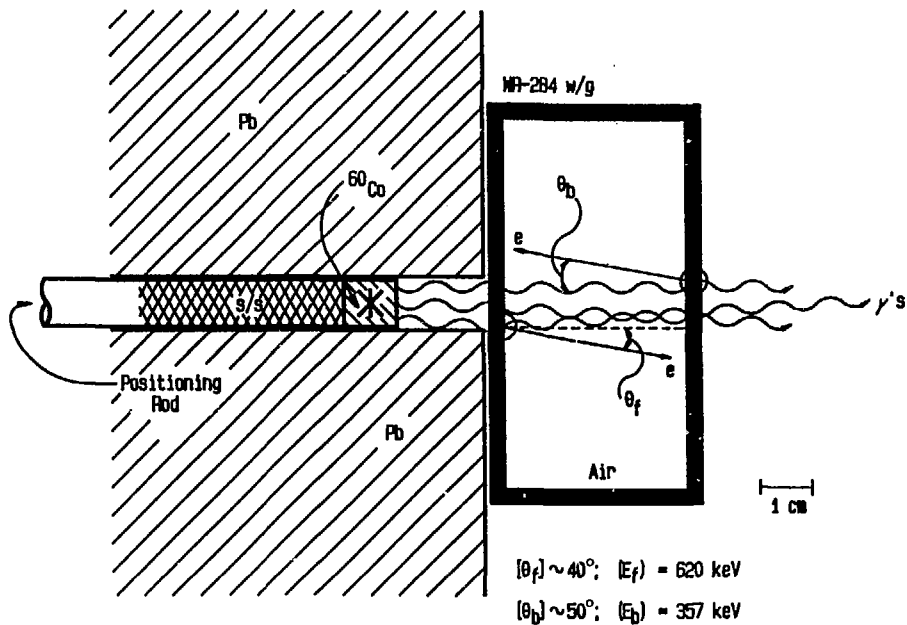$[\theta_f] \sim 40°;$ $[E_f] = 620$ keV
$[\theta_b] \sim 50°;$ $[E_b] = 357$ keV

2.13, depends only logarithmically on the initial density, a
more economical and approximate approach will be taken.
Here, for processes in the gas, energy dependent quantities
will be evaluated at the average electron or photon energy,
or, where appropriate, thermal values used. Chemical ef-
fects will be ignored. Also, dry air will be the only gas
considered.

   To determine the equilibrium spatial electron density,
the homogeneous continuity equation for the electrons must
be solved,

$$\frac{\partial n}{\partial t} = S - \nu_a n - (D_1/\Lambda^2)n + \beta_d NN^- = 0. \tag{B.1}$$

Here S is the volume production rate of electrons due to
ionization processes caused by the radioactive sources, ν_a
is the attachment rate, which accounts for loss of electrons
due to attachment to neutral molecules to form negative
ions, D_1/Λ^2 is the loss rate due to electron diffusion, and
$\beta_d NN^-$ is the production rate of electrons due to collisional
detachment of electrons from negative ions. In this last
term, β_d is the detachment coefficient, N^- is the negative
ion density, and N is the neutral density. Because of the
low electron densities under consideration, electron-ion
recombination processes will be neglected. Since the last
term in equation B.1 contains the negative ion density, two
additional equations must also be solved. These are the
equilibruim equations for positive and negative ion density,

$$\frac{\partial N^-}{\partial t} = \nu_a n - \alpha_1 N^- N^+ - (D_2/\Lambda^2)N^- - \beta_d NN^- = 0 , \qquad (B.2)$$

$$\frac{\partial N^+}{\partial t} = S - \alpha_1 N^- N^+ - (D_3/\Lambda^2)N^+ = 0. \qquad (B.3)$$

Since chemical effects have been ignored in these equations, both ions are treated generically. N^- is considered to be the oxygen negative molecular ion density and N^+ is the nitrogen and oxygen positive molecular ion density. Atomic ions are ignored. The attachment, detachment, and volume production rate terms in equations B.2 and B.3 balance similar terms in equation B.1. In addition, ion-ion recombination with coefficient α_1, and positive and negative ion diffusion terms (D_2/Λ^2) and (D_3/Λ^2) are included. To solve these three equations, we consider each term separately.

The Volume Production Rate S

The two radioactive sources, one of which is indicated in Fig. B-1, were placed symmetrically 2 cm from the WR284 waveguide walls in 1-cm-diameter lead collimators. Assuming perfect collimation, $1.78 \cdot 10^8$ γ-rays/sec were radiated into the waveguide. The Monte-Carlo numerical simulation computer programs SANDYL[43] and TIGER[44] were used to model the transport of the γ-radiation through the waveguide walls and through the air inside. With these simulations, the transport of γ-rays and electrons could be followed across any desired plane or zone in the problem geometry. All nuclear and atomic processes occurring at energies greater than 1 keV were allowed for; in this problem the most signifi-

cant ones were knock-on, photo-electric effect, Compton effect, Auger, bremsstrahlung, and K x-ray processes. The simulations calculated energy flux distributions and photon and electron flux and angular distributions across problem zones, as well as energy and particle depositions within any desired zone. Standard deviations for all these values were also calculated. The codes automatically deposited all particles of less than 1-keV energy; therefore they did not yield the total electron production rate. They did, however, yield the flux and energy and angular distributions of electrons and photons crossing the inside waveguide wa'⌐s into the gas interior.

We consider first the results of the simulations for the electrons. Of the "primary" electrons produced, the forward scattered ones had 620 ± 12-keV average energy, and $5.17\cdot10^{-3}\pm1.0\cdot10^{-4}$ were produced per γ-ray. The backscattered ones had 357 ± 21-keV average energy and $6.4\cdot10^{-4}$ $\pm3.2\cdot10^{-5}$ were produced per γ-ray. The scattering angular distributions were peaked at $0°$ for the forward scattered electrons and $180°$ for the back-scattered electrons, with the distributions falling off, as shown in Fig. B-1, to $1/e$ of their peak values at $40\pm4°$ and $50\pm10°$ for the forward and backscattered particles, respectively. These simulations, coupled with the radioactive source strength, indicated that $1.03\cdot10^6$ "primaries", with average energy 590 ± 41 keV, entered the waveguide interior per second.

Although approximately 200 photons entered the gas for every electron, photon energy-loss calculations indicated that ionization due to photons was less than 1% of that due to the electrons. Photon ionization was therefore ignored.

The total electron production, then, must be determined from the interaction of the radioactive source-produced "primaries" with the gas. The stopping power -dE/dx, and the mean range R, of 590-keV electrons in air are 1.74 MeV/gm/cm² and 0.243 gm/cm², respectively.[45] Since the waveguide was 3.4-cm wide, these numbers allow one to calculate the energy lost from the primary electrons to the gas. Further, careful measurements have been made of the mean energy expended in a gas per ion pair formed. This number, called W by most authors, equals E/N, where E is the initial electron kinetic energy and N is the mean number of ion pairs formed. For dry air, $W = 33.8 \pm 0.15$ eV/ion pair[46] at 590 keV. Included are all ionization processes, including ionizations produced by high-energy secondary electrons.

Since the fractional energy-loss of a 590-keV electron crossing 3.4 cm of air is negligible, the volume production, assuming uniform radiation and ionization in a 3-cm diameter cylinder between the sources (~25 cm³ volume) is:

$$S = (4.12 \cdot 10^4) \rho \cdot \frac{dE}{dx} \cdot \frac{b}{W} \quad \text{electrons/sec/cm}^3, \quad (B.4)$$
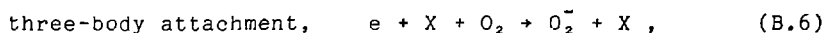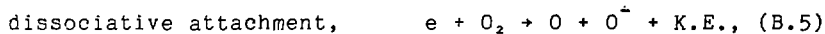
where ρ is the gas density in gm/cm³, b is the waveguide dimension in cm, and dE/dx and W are in units of eV/gm/cm²

and eV/ion pair, respectively.

The average energy of the secondary electrons produced, though not measured, was estimated to be about 70 eV according to electron-beam transport simulations done by Strickland and Ali.[47] The results of those simulations, shown in Fig. 4 of Ref. 47 as a plot of average initial secondary energy vs energy of all secondaries up to a given energy, with initial beam energy as a parameter, also yielded the same result as equation B.4, within 30%.

Attachment

Several attachment processes can occur between electrons and neutral oxygen molecules or atoms in air. The predominant ones are

dissociative attachment, $e + O_2 \rightarrow O + O^- + K.E.,$ (B.5)
three-body attachment, $e + X + O_2 \rightarrow O_2^- + X ,$ (B.6)
radiative attachment, $e + O \rightarrow O^- + h\nu ,$ (B.7)
        or $e + O_2 \rightarrow O_2^- + h\nu .$ (B.8)

Rate constants for all these reactions have been measured.[48,49] At electron energies of a few eV, dissociative attachment is important, but below 1 eV, three-body attachment dominates.

Initially, the electrons created by ionization inside the waveguide have an average energy of 70 eV, as indicated above. Using the electron energy-loss rate vs energy shown in Fig. 2-6 to integrate a loss equation of the form

$$\frac{\partial \varepsilon}{\partial t} = -\nu_w \varepsilon, \qquad (B.9)$$

one finds that approximately $10^9/N$ seconds, where N is the gas number density in cm^{-3}, are required for the 70-eV electrons to drop to 1 eV. Equation B.5 has a rate coefficient[50,51] at 5-eV electron energy of about 10^{-11} cm^3/sec, which implies a lifetime due to two-body attachment of $5 \cdot 10^{11}/N$ seconds in air. Clearly, 70-eV electrons are reduced to less than 1 eV faster than two-body attachment can occur. For this reason, only three-body attachment will be considered. Electrons undergoing these processes obey the rate equation,

$$\frac{\partial n}{\partial t} = -\{K_1[O_2]^2 + K_1'[O_2][N_2]\} \cdot n = -\nu_a n , \qquad (B.10)$$

where the square brackets indicate concentrations (number densities). K_1 is the three-body coefficient for attachment with oxygen as the stabilizing third body, and K_1' the coefficient for nitrogen as the third body. Ref. 49 gives these coefficients as

$$K_1 = (1.4 \pm 0.2) \cdot 10^{-29} \cdot (300/T) \exp(-600/T) \text{ cm}^6/\text{sec}, \qquad (B.11)$$
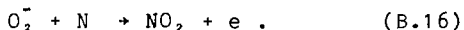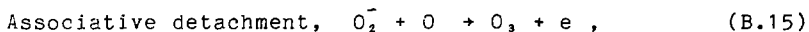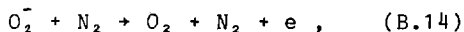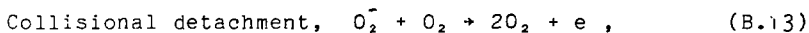
$$K_1' = (1 \pm 0.5) \cdot 10^{-31} \text{ cm}^6/\text{sec}, \qquad (B.12)$$

where T is the gas temperature in K. Here, the electrons will be considered thermal. At the lowest pressures we consider, where average electron energies are 1 or 2 eV, this attachment rate will not be correct. However, a value of ν_a $= 10^{-31}N^2 \text{ sec}^{-1}$ will be in error by no more than a factor of

two or three[52,53] over the electron energy range of 0.025 to 1 eV. Furthermore, at the lowest pressures, where the error is largest, diffusion dominates attachment as an electron loss mechanism.

Detachment

Because three-body attachment is the primary attachment process, the negative oxygen molecular ion will be the dominant negative ion. Both collisional detachment with neutral molecules and associative detachment with neutral atoms can occur,

Collisional detachment,	$O_2^- + O_2 \rightarrow 2O_2 + e$,	(B.13)
	$O_2^- + N_2 \rightarrow O_2 + N_2 + e$,	(B.14)
Associative detachment,	$O_2^- + O \rightarrow O_3 + e$,	(B.15)
	$O_2^- + N \rightarrow NO_2 + e$.	(B.16)

Only collisional detachment will be considered because of the relative densities of the molecules and atoms. The rate coefficients for these reactions are given by[49,54]

$$B.13: K_2 = (2.7\pm0.3)\cdot10^{-10}\cdot(T/300)^{\frac{1}{2}}\cdot\exp(-5590/T), \quad (B.17)$$

$$B.14: K_2' = (1.9\pm0.4)\cdot10^{-12}\cdot(T/300)^{\frac{1}{2}}\cdot\exp(-4490/T). \quad (B.18)$$

The experimental data from which the above coefficients were derived was taken at temperatures between 375 and 600 K, so their use here, at 300 K, will be an extrapolation. At 300 K, these equations yield an electron rate equation,

$$\frac{\partial n}{\partial t} = -\frac{\partial [O_2^-]}{\partial t} = K_2[O_2^-][O_2] + K_2'[O_2^-][N_2], \text{ or}$$

$$\frac{\partial n}{\partial t} = -\frac{\partial [O_2^-]}{\partial t} = \beta_d[O_2^-] = (9.2 \cdot 10^{-19})N[O_2] \ . \tag{B.19}$$

Ion-Ion Recombination

For the two dominant recombination reactions,

$$O_2^- + N_2^+ \rightarrow O_2 + N_2 \ , \tag{B.20}$$

$$O_2^- + O_2^+ \rightarrow 2O_2 \ , \tag{B.21}$$
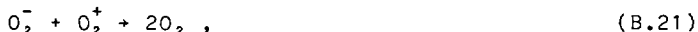
the two-body rate coefficients are[55] $(1.6\pm0.5)\cdot10^{-7}$ cm³/sec and $(4.2\pm1.3)\cdot10^{-7}$ cm³/sec, respectively, at 300 K. At pressures above 10 torr in air, recombination proceeds by a three-body, or so-called Thompson[56] process, with rate coefficient[55] $(3\pm1)\cdot10^{-25}$ cm⁶/sec. Since positive ions are being treated generically, a value for α_1 in equations B.2 and B.3 of $2.0\cdot10^{-7}$ cm³/sec will be used below 10 torr, while above 10 torr $\alpha_1 = 3\cdot10^{-25}N$ cm³/sec will be used. Above 10 torr, this choice of α_1 corresponds to the measured value for air, regardless of the specific recombination reaction. Combining the rate coefficients for B.20 and B.21 to get $\alpha_1 = 2.0\cdot10^{-7}$ cm³/sec for air below 10 torr is an approximation which more strongly weights the predominant reaction, B.20. This value should be in error by no more than a factor of two for air; moreover, the recombination terms in equations B.2 and B.3 are the least significant ones at low pressures, and the computed electron density is insensitive to even large errors in them.

Ion Diffusion

It is assumed that diffusion takes place in the funda-
mental mode in the waveguide. For an infinite rectangular
pipe of width a and depth b, fundamental mode diffusion
means that Λ^2 in equations B.1, B.2, and B.3 is[57]

$$\Lambda^2 = \left[(\pi/a)^2 + (\pi/b)^2 \right]^{-1} . \tag{B.22}$$

For WR284 waveguide, $\Lambda^2 = 0.96$ cm². The thermal diffusion
coefficients for N_2^+, O_2^+, and O_2^- can be determined from their
zero-field mobilities, since the mobility, μ, is

$$\mu = De/kT. \tag{B.23}$$

The measured zero-field mobility of N_2^+ in N_2 is[58] 1.87
cm²/volt·sec, while that for O_2^+ in O_2 is[59] 2.22
cm²/volt·sec. At 300 K, the mobilities of O_2^- and O_2^+ in oxy-
gen are about equal; for O_2^- it is[59,60] 2.4 cm²/volt·sec.
Since the diffusion constant and mobility are inversely pro-
portional to pressure, equation B.23 implies that at 300 K,

$$DN = (6.9 \cdot 10^{17})\mu , \tag{B.24}$$

where D is in cm²/sec, N in cm⁻³, and μ in cm²/volt·sec.
Assuming a positive ion mobility of 2.0 cm²/volt·sec in air,
and an O_2^- mobility the same in air as in oxygen (Recall that
we are ignoring chemical reactions. If charge exchange oc-
curs, one still has a diffusing ion, though its identity may
be unknown.), one gets

$$D_2 N = 1.6 \cdot 10^{18} \ \text{sec}^{-1} \ \text{for} \ O_2^- \ , \tag{B.25}$$

$$\text{and} \quad D_3 N = 1.4 \cdot 10^{18} \ \text{sec}^{-1} \ \text{for} \ O_2^+ \ \text{and} \ N_2^+ \ . \tag{B.26}$$

Electron Diffusion

The thermal diffusion constants for electrons in oxygen and nitrogen given in Dutton's survey[61] will be used,

$$\text{electrons in } N_2, \quad D_{th} N = 9.5 \cdot 10^{21} \ \text{cm}^{-1} \text{sec}^{-1} \ , \tag{B.27}$$

$$\text{electrons in } O_2, \quad D_{th} N = 39 \cdot 10^{21} \ \text{cm}^{-1} \text{sec}^{-1} \ . \tag{B.28}$$

Since there are no published thermal diffusion values for air, a density weighted average,

$$\frac{1}{D_{air}} = \frac{f_{O_2}}{D_{O_2}} + \frac{f_{N_2}}{D_{N_2}} \ , \tag{B.29}$$

where f_{O_2} and f_{N_2} are the fractions of O_2 and N_2 in air, respectively, will be used. Again, these values will not be correct at the low pressures where the average electron energies are not thermal. However, using the definition of the diffusion constant, $D = \langle v^2/3\nu_c \rangle$, with an energy independent value[1] of $\nu_c = 5.3 \cdot 10^9 p$, and averaging over a Maxwellian distribution, one obtains[1]

$$DN = 7.8 \cdot 10^{21} \epsilon_0 \ \text{cm}^{-1} \text{sec}^{-1}, \tag{B.30}$$

where ϵ_0 is the average energy, over the distribution, in electron volts. Equation B.30 is applicable for electron energies of up to a few eV, and pressures greater than about 10 torr, where ν_c is approximately independent of energy.

For additional comparison, we have the results of swarm measurements of the longitudinal diffusion coefficient in nitrogen (for diffusion parallel to an applied electric field) at E/p of approximately 4 volts/cm·torr, which correspond to electron energies of about 1 eV. This result is[62]

$$D_L N \approx 2 \cdot 10^{22} \ cm^{-1} sec^{-1}. \hspace{3cm} (B.31)$$

From equations B.27, B.28, B30, and B.31, we see that using B.27 and B.28 in equation B.29 should yield a diffusion constant accurate to within a factor of three over the entire pressure range under consideration.

Table B-1 lists values of the rate coefficients dis-
cussed above as a function of air pressure, at those pres-
sures for which short-pulse air breakdown data was obtained.
All coefficients are in units of s^{-1}, except for S and α_1,
which have units of $cm^{-3}s^{-1}$ and $cm^3 s^{-1}$, respectively.

Table B-1

Pressure [torr]	300	66.3	15.4	3.5	0.8
Rate Coeff.					
S	$3.7 \cdot 10^6$	$8.1 \cdot 10^5$	$1.9 \cdot 10^5$	$4.3 \cdot 10^4$	$9.8 \cdot 10^3$
ν_a	$1.1 \cdot 10^7$	$5.5 \cdot 10^5$	$3.0 \cdot 10^4$	$1.5 \cdot 10^3$	80
$\beta_d N$	9.8	2.2	0.50	0.11	0.026
α_1	$3.2 \cdot 10^{-6}$	$7.0 \cdot 10^{-7}$	$2.0 \cdot 10^{-7}$	$2.0 \cdot 10^{-7}$	$2.0 \cdot 10^{-7}$
D_1/Λ^2	$1.5 \cdot 10^3$	$6.8 \cdot 10^3$	$2.9 \cdot 10^4$	$1.3 \cdot 10^5$	$5.6 \cdot 10^5$
D_2/Λ^2	0.16	0.71	3.1	13	59
D_3/Λ^2	0.14	0.62	2.7	12	51

Using the results shown in table B-1, one obtains, after
simultaneous solution of equations B.1, B.2 and B.3, the
estimated initial electron densities in cm^{-3} given in table
B-2.

Table B-2

Pressure [torr]	300	66.3	15.4	3.5	0.8
Density n_e [cm^{-3}]	1.3 (0.47)	5.5 (2.1)	4.8 (4.5)	0.4 (0.4)	0.02 (0.02)

The numbers in parentheses in table B-2 indicate the results
obtained from solving equation B.1 without the detachment

term $\beta_d NN^-$. They are presented not only to show the effects
of detachment, but also because there is less uncertainty in
the rate coefficients used to derive them. If one accounts
for uncertainties in deposition volume, source production
rate, attachment, and diffusion, one finds that the numbers
in parentheses are accurate to within about a factor of
five. The initial density estimates which include detach-
ment are more uncertain, however.

 During the course of the longer-pulse (>1 μs) measure-
ments done for this work, it became apparent that at pres-
sures greater than 200 torr, the statistical distributions
of times-to-breakdown following the onset of many identical
pulses were not consistent with the statistics one would
expect would result from primary electrons produced once
every microsecond, all secondaries of which had attachment
lifetimes of less than 100 ns. It appeared that an addi-
tional source of electrons was present, and for this reason,
detachment was considered.

 Table B-2 indicates that detachment can be important,
particularly at higher pressures, because of the large ion
densities produced by the radioactive sources. At atmo-
spheric pressure, a similar analysis indicates an order of
magnitude difference in calculated initial density, depen-
ding on whether detachment is included or not.

 The detachment rate calculated from equations B.17 and
B.18 lies outside the range of experimental data and its
uncertainty is unknown, though the exponential temperature

dependence of equations B.17 and B.18 would be expected for a Boltzman distribution of ion energies. Because chemical reaction effects were ignored, the calculated ion density uncertainties are difficult to estimate. The recombination coefficients used were reasonable, but the calculations of ion removal due to diffusion assumed that the only ions present were O_2^-, O_2^+, and N_2^+. However, the zero-field mobilities of the diatomic ions in irradiated air all lie within a factor of two of each other, while other species (NO_2^-, NO_3^-) would diffuse somewhat more slowly. The ion diffusion coefficients used should thus be within a factor of five of the actual values regardless of the identity of the ion.

Ion identities also affect the detachment rate, since electrons have higher affinities for NO_2^- and NO_3^- than O_2^-. Hirsh and Eisner,[62] in an experiment in which air was irradiated by MeV electrons from an accelerator, found that initially the predominant negative ion was O_2^-, while after 30 minutes of continuous irradiation, the dominant ions were NO_3^-, NO_2^-, and O^-, in that order. Their electron flux was about 10^4 times that produced by the sources described here, but the results are consistent with observations made during experiments conducted for this work. Time-to-breakdown distributions at pressures greater than 100 torr had a much wider spread if the measurements were made using aged, irradiated air than fresh air, suggesting lower detachment rates. For this reason, the gases used were replenished often enough that no aging effects on the distributions were ob-

served.

Reasonable estimates of uncertainties are a factor of five for the detachment rate and a factor of ten for the ion densities, resulting in an uncertainty factor of fifty for the initial electron density above 200 torr. Below that pressure, uncertainties should be the same as without detachment.

Though these uncertainties are large, the ultimate aim is to be able to accurately predict breakdown field thresholds, which depend logarithmically on initial density, as was mentioned earlier. One can examine the field dependence of the breakdown condition, equation 2.13, by employing the effective field concept. DC measurements have been made of $\nu_n/p = (\nu_i - \nu_a)/p$ as a function of electric field divided by the pressure. Using the effective field E_e to relate DC breakdown fields to microwave breakdown fields, one can empirically fit E_e/p to ν_n/p, obtaining,[63] for pulses short enough that diffusion can be neglected,

$$E_e/p \approx 3.75[(p\tau)^{-1}\ln(n_f/n_0) + 6.4\cdot10^4]^{3/16} \text{ Volt/cm·torr}$$

$$\dots\dots\dots\dots\dots\dots\dots\dots\dots\dots(B.32)$$

Using this expression, with $n_f = 10^{11}$ cm^{-3}, and any product $p\tau$ in the range $10^{-9} < p\tau(\text{torr·sec}) < 10^{-4}$, one finds only a 4% variation (at most) in E_e/p, when n_0 varies between 1 cm^{-3} and 100 cm^{-3}. This insensitivity of the breakdown field to a two order-of-magnitude change in initial electron

density clearly suggests that the initial densities derived above, used as input for numerical simulations, should lead to accurate results, even given their large uncertainties.

Appendix C - Helium Data

In the course of the microwave breakdown experiments on air and nitrogen, pulse breakdown data was also obtained for helium. Though the helium data has been reduced from its raw form for presentation here, no analyses or comparisons to theoretical models have been done; the data is presented only for reference purposes. The experimental measurements and techniques used were the same as those used for air and nitrogen, and one should see earlier chapters and appendices of this thesis for more information on those topics.

Fig. C-1 shows distributions of times-to-breakdown in helium for pulses of 100-ns to greater than 1-μs duration. The figure is similar to Figs. 4-1 and 4-2 for air and nit-rogen, and the data were obtained in an identical experi-ment. From distributions like those shown in Fig. C-1, breakdown times vs microwave field strength, as shown in Fig. C-2, were determined; this figure is similar to Fig. 4-4 in Chapter IV, and the data were derived the same way.

Fig. C-3 shows the most probable breakdown field strengths and times-to-breakdown for helium breakdown during the rise time of the 47-ns klystron pulse. Again, the ex-periments which yielded these results were identical to those done with air and nitrogen, whose results are shown in Fig. 4-9.

Finally, Fig. C-4 depicts the effects of breakdown in helium on the 2-ns duration, cavity-generated pulse. The first column of plots shows incident pulses before breakdown and the second column shows pulses transmitted after breakdown. These plots are similar to those shown in Figs. 4-11 and 4-12 for air and nitrogen.

The experimental errors for the air and nitrogen measurements reported in Sec. A-7 of Appendix A also apply to these data.
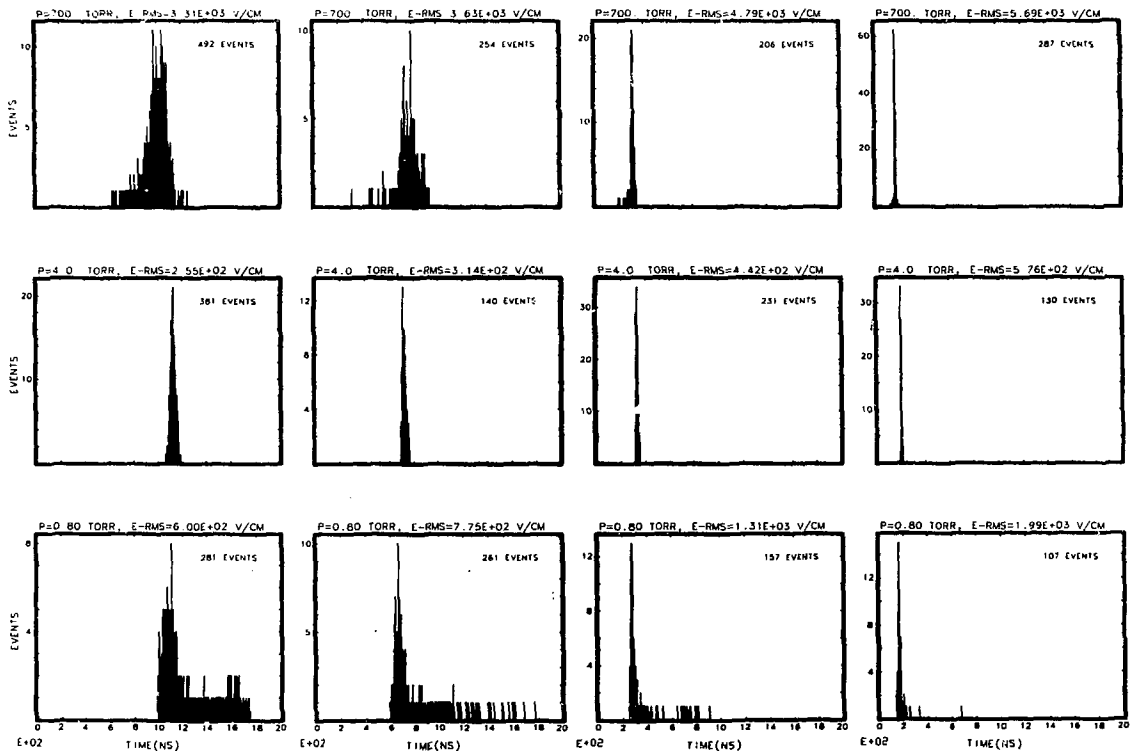
FIG. C-1 – <u>Distributions of times-to-breakdown in helium.</u> From repeated measurements at constant pulse amplitude and pressure. Incident pulse duration = 1.8 µs, total abscissa range = 2 µs. Fields are rms fields at the center of the waveguide.
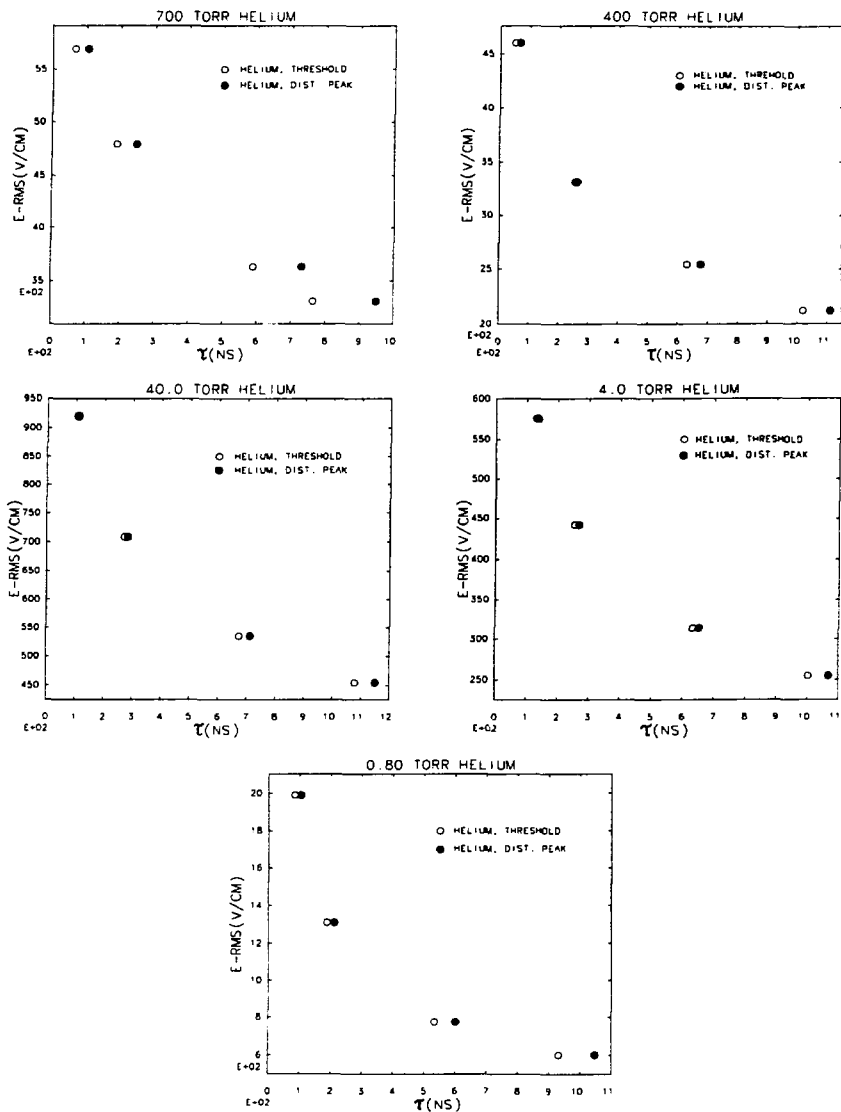
Long-Pulse Fields vs Breakdown Times in Helium

FIG. C-2

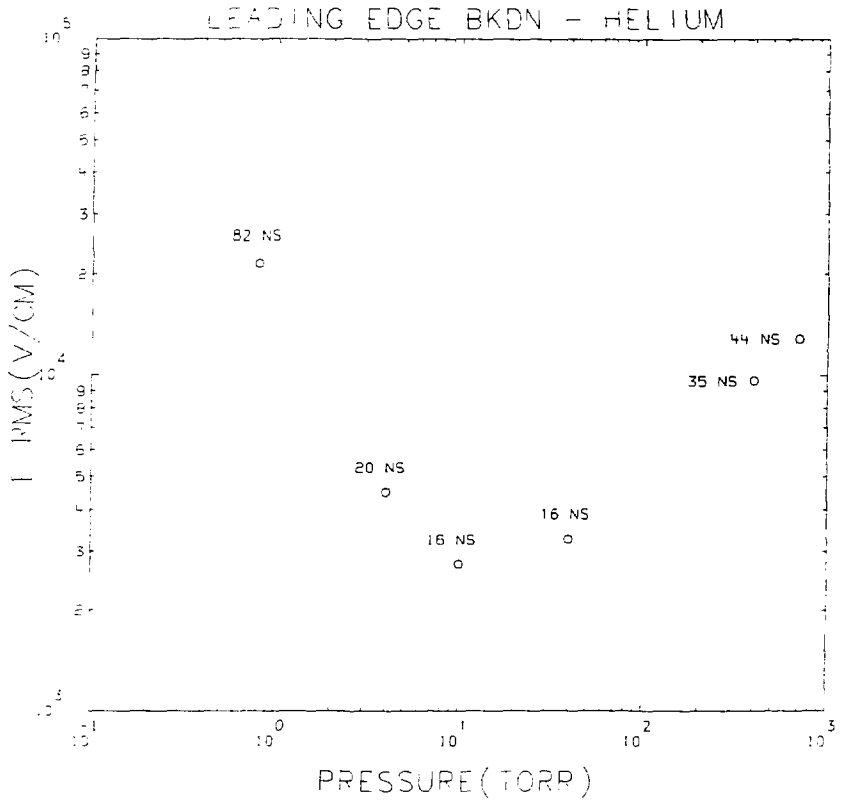Helium Breakdown During the Rise Time of the
47-ns Rise Time Pulse

FIG. C-3

2-ns Pulse Breakdown in Helium;
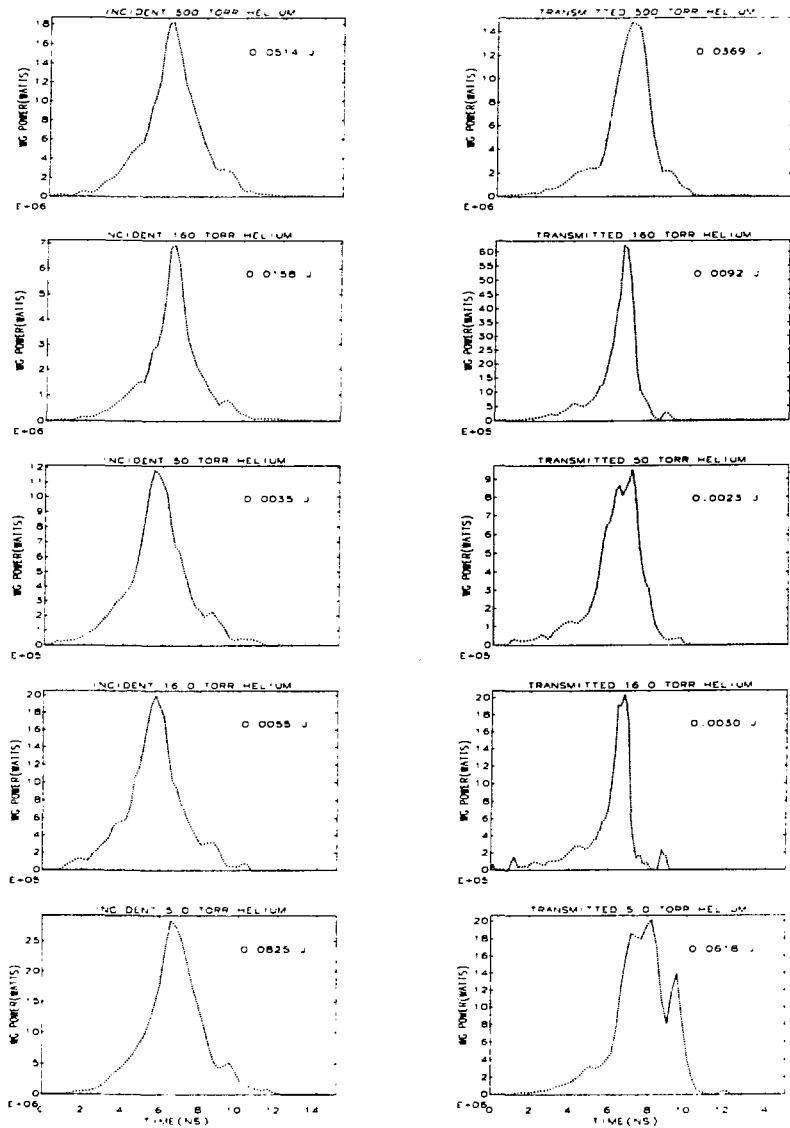## Measured Inc/Trans Pulse Envelopes

FIG. C-4

BIBLIOGRAPHY

1. A.D. MacDonald and S.J. Tetenbaum in **Gaseous Elec-
    tronics, Volume** I (M. Hirsh and H. Oskam, eds.), pp.173-
    217. Academic Press, New York, San Francisco, and
    London, 1978.

2. A.D. MacDonald, **Microwave Breakdown in Gases.** Wiley, New
    York, 1966.

3. S.C. Brown, **Introduction to Electrical Discharges in
    Gases,** chapter 10. Wiley, New York, 1966.

4. N.H. Makik and A.H. Qureshi, "Electrical Breakdown in
    Gases", in **Digest of Literature on Dielectrics,** Vol. 42,
    Ch. 5, S.J. Rzad, Ed.; Nat. Acad. of Sciences, Washing-
    ton, 1979. Most volumes in this yearly periodical con-
    tain up to date literature reviews on the subject of
    electrical breakdown in gases.

5. S.J. Tetenbaum, A.D. MacDonald, and H.W. Bandel, J.
    Appl. Phys. **42,** 5871(1971).

6. C. Buntschuh and M. Gilden, RADC-TDR-64-204, Rome Air
    Development Center, Griffiss Air Force Base, New York,
    July, 1964.

7. A.N. Didenko, S.A. Novikov, S.V. Razin, P.Yu. Chumerin,
    and Yu.G. Yushkov, Radiotekhnika i elektronika, No. 4,
    731(1985) [Sov. J. Communications Tech. and Electronics
    (formerly Radio Engng. Electron. Phys.) **30,** No. 7, 105
    (1985)].

8. J.H. Yee, R.A. Alvarez, D.J. Mayhall, D.P. Byrne, and

J. DeGroot, Phys. Fluids **29**, 1238(1986).

9. S.C. Brown and A.D. MacDonald, Phys. Rev. **76**, 1629
    (1949).

10. J.W. Schwinger and D. Saxon, **Discontinuities in Wave-
    guides,** Gordon and Breach Science Publ., Inc., 1968.

11. A.D. MacDonald, D.U. Gaskell, and H.N. Gitterman, Phys.
    Rev. **130**, 1841(1963).

12. H.A. Herlin and S.C. Brown, Phys. Rev. **74**, 291(1948).

13. H.A. Herlin and S.C. Brown, Phys. Rev. **74**, 910(1948).

14. H.A. Herlin and S.C. Brown, Phys. Rev. **74**, 1650(1948).

15. P. Felsenthal and J.M. Proud, Phys. Rev. **139**, A1796
    (1965).

16. L. Gould and L.W. Roberts, J. Appl. Phys. **27**, 1162
    (1956).

17. J. Yee and D. Mayhall, Lawrence Livermore National Lab-
    oratory, private communication.

18. R.A. Alvarez, D.P. Byrne, and R.M. Johnson, **Prepulse
    Suppression in Microwave Pulse Compression Cavities,** to
    be published in Reviews of Scientific Instruments.

19. P. Felsenthal, J. Appl. Phys. **37**, 4557(1966)

20. R.S. Elliot, IRE Trans. Microwave Theory Tech. MTT-5,
    254(1957).

21. M. Yamagishi, K. Mizuno, J.S. DeGroot, R. Alvarez, and
    T. Oda, Bull. Am. Phys. Soc. **30**, 1554(1985).

22. W.P. Ballard and L.M. Earley, Rev. Sci. Instrum. **56**,
    1470(1985).

23. see, for example, R. Bracewell, **The Fourier Transform**

and Its Applications, McGraw-Hill, New York and San
Francisco, 1965.

24. D. Lager and S. Azevedo, SIG, A General Purpose Signal
Processing Program, UCID-19912, Lawrence Livermore
National Laboratory (1985).

25. D.L. Birx and D.J. Scalapino, J. Appl. Phys. 52, 187
(1981).

26 W.W. Hansen, J. Appl. Phys. IX, 654(1938).

27. E.U. Condon, J. Appl. Phys. XII, 129(1940).

28. F. Borgnis, Ann. Phys. p.359, 1938.

29. R.A. Alvarez, UCID-19696, Lawrence Livermore National
Laboratory, Livermore, CA, February, 1983 (to be pub-
lished in Reviews of Scientific Instruments).

30. S.V. Barnev and O.P. Korovin, Sov. Phys. Tech. Phys. 25,
1444(1980).

31. D.B. Schwarzkopf, Microwave J. 5, 172(1962).

32. D. Birx, G.J. Dick, W.A. Little, J.E. Mercereau, and
D.J. Scalapino, Appl. Phys. Lett. 32, 68(1978).

33. R.A. Alvarez, D. Birx, D. Byrne, M. Mendonca, and R.M.
Johnson, IEEE Trans. Mag. MAG-17, 935(1981).

34. C. Buntschuh, B. Salkins, and M. Gilden, RADC-TDR-63-82,
Rome Air Development Center, Griffiss Air Force Base,
New York, February 1963.

35. R.A. Alvarez, D.L. Birx, D.P. Byrne, E.J. Lauer, and D.
J. Scalapino, Particle Accel. 11, 125(1981).

36. Z.D. Farkas, H.A. Hogg, G.A. Loew, and P.B. Wilson,
SLED, A Method of Doubling SLAC's Energy, Proc. IX In-

ternatl. Conf. on High Energy Accelerators, SLAC, 1974.

37. see, for example, J.C. Slater, **Microwave Electronics**, Van Nostrand, New York, 1950.

38. H. Farber, M. Klinger, M. Sucher, and E. Malloy, IEEE Trans. Microwave Theory Tech. **MTT-13**, 28(1965).

39. D.L. Birx and D.J. Scalapino, IEEE Trans. Magn. **MAG-15**, 33(1979).

40. D.L. Birx and D.J. Scalapino, J. Appl. Phys. **51**, 3629 (1980).

41. Ref. 2, Chapter 4.

42. H.W. Bandel and A.D. MacDonald, J. Appl. Phys. **41**, 2903 (1970).

43. H.M. Colbert, **SANDYL, A Computer Program for Calculating Combined Photon-Electron Transport in Complex Systems**, SLL-74-0012, Sandia National Laboratory, Livermore, CA, May, 1974.

44. J.A. Halbleib and T.A. Mehlhorn, **ITS: The Integrated TIGER Series of Coupled Electron/Photon Monte-Carlo Codes**, SAND84-0573, Sandia National Laboratory, Livermore, CA, November, 1984.

45. A.T. Nelms, Supplement to NBS Circular 577, National Bureau of Standards, Washington, D.C., 1958.

46. ICRU Report 31, International Commission on Radiation Units and Measures, Washington, D.C., 1979.

47. D.J. Strickland and A.W. Ali, NRL Memorandum Report 4956, Naval Research Laboratory, Washington, D.C., 1982.

48. A.V. Phelps, Canad. J. Chem. **47**, 1783(1969).

49. A.V. Phelps, Chapt. 17, **DNA Reaction Rate Handbook**, DNA 1948H, Bortner and Baurer, Eds., DASIAC, DOD Nuclear Information and Analysis Center GE-Tempo, Santa-Barbara, CA, 1972.

50. A.W. Ali, NRL Memorandum Report 4619, Naval Research Laboratory, Washington, D.C., 1981.

51. W.R. Henderson, W.L. Fite, and R.T. Brackman, Phys. Rev. **183**, 157(1968).

52. A.W. Ali, NRL Memorandum Report 5341, Naval Research Laboratory, Washington, D.C., 1984.

53. L.M. Chanin, A.V. Phelps, and M.A. Biondi, Phys. Rev. **128**, 219(1962).

54. J.L. Pack and A.V. Phelps, J. Chem. Phys. **44**, 1870(1966).

55. M.A. Biondi, Chapt. 16 of Ref. 49.

56. J.J. Thompson, Phil. Mag. **47**, 337(1924).

57. E.W. McDaniel, **Collision Phenomenon in Ionized Gases**, John Wiley and Sons, New York, London, Sidney, 1964.

58. T.M. Miller, J.T. Moseley, D.W. Martin, and E.W. McDaniel, Phys. Rev. **173**, 115(1968).

59. H.Z. Eiber, Z. angew. Phys. **15**, 103(1963).

60. J.A. Rees, Aust. J. Phys. **18**, 41(1965).

61. J. Dutton, J. Phys. Chem. Ref. Data **4**, 577(1975).

62. M.N. Hirsh and P.N. Eisner, Radio Science **7**, 125(1972).

63. G. August, SRI International Report, 11 May 1982 (unpublished), SRI International, Menlo Park, CA.